TRANSFORMER THERMAL ASSESSMENT UNDER GEOMAGNETICALLY INDUCED CURRENT CONDITIONS

MILAD AKBARI

A DISSERTATION SUBMITTED TO
THE FACULTY OF GRADUATE STUDIES
IN PARTIAL FULFILLMENT OF THE REQUIREMENTS
FOR THE DEGREE OF
DOCTOR OF PHILOSOPHY

GRADUATE PROGRAM IN ELECTRICAL
ENGINEERING AND COMPUTER SCIENCE
YORK UNIVERSITY
TORONTO, ONTARIO

November 2022

Abstract

Power transformers are one of the most critical and expensive pieces of equipment in power systems. The widespread use of the transformer in power grids and its high cost makes the lifetime and reliability of this apparatus highly important. Although some factors affect the reliability of transformers, thermal and electrical stresses are the main reasons for transformer failure. As a result, transformers thermal modeling is essential in the design and operation stage to represent the thermal behavior of transformers during normal operation or transient phenomena. However, the multi-physics behavior of transformers, and the nonlinear and frequency-dependent parameters make this modeling a challenging task.

This thesis aims to develop a more accurate transformer model for representing the thermal behavior of transformers, especially during transient phenomena such as Geomagnetically Induced Current (GIC). To fulfill this goal, it is necessary to perform several tasks in different fields, such as geometry and material modeling, electromagnetic studies, and investigation into computational fluid dynamic (CFD) analysis of transformers.

First, the GIC phenomenon and its impact on the transformer are briefly explained. Then, a comprehensive literature review of existing transformer thermal models is performed to find their drawbacks. A 3-phase, 3-leg transformer is then subjected to an electromagnetic-thermal study in both normal and GIC conditions. It is shown that the structural parts, including the tank, clamps, and tank shunts, are saturated with a small amount of GIC. However, the transformer core becomes saturated with larger currents, resulting in additional stray losses in the structural parts. The findings show that the most vulnerable part is the tank, as the hot spot temperature (HST) of the

tank approaches 372.14 ^{0}C, which is double the permissible limit, under 66.6A GIC per phase. Finally, a new approach is proposed to determine the HST of OIP bushing based on the FEM-modified thermal equivalent circuit (TEC) model. The proposed model can accurately estimate the HST of the bushings under normal and GIC conditions. Furthermore, a detailed thermal analysis is performed to investigate the impact of different parameters such as load, ambient temperature, and top oil temperature on the thermal performance of bushings.

Dedication

ماحصل آموخته هایم را تقدیم می کنم به

پدرم،

استوارترین تکیه گاه زندگی ام

و مادرم،

زیباترین نغمه زندگی ام

Acknowledgments

This PhD thesis concludes the research that I have conducted at the Department of Electrical Engineering and Computer Science (EECS), Lassonde School of Engineering, York University from September 2018 until August 2022. There are many people who have helped and empowered me to complete this research.

My first sincere gratitude must go to my supervisor Prof. Afshin Rezaei-Zare for providing the opportunity to continue my academic studies at the post-graduate level. I would also thank him for his guidance, supervision, and encouragement during my PhD studies period. He has also given me great freedom to pursue independent work, which provides me with the opportunity to learn more.

I would also like to thank my PhD committee members Prof. John Lam and Prof. Hany Farag for their support and advice. I want to express my appreciation to all my current and former colleagues and staff at the Department of Electrical Engineering and Computer Science.

I would like to express my deep gratitude to Dr. Ryan Schimizzi, Dr. Saeed Asghari, and all Nexim group members at Ansys Company for providing me with a great internship. I have learned a lot and had a great time during that time.

Last but certainly not least, I would like to thank my family and friends, especially my parents and my lovely fiancé. Thanks to my fiancé, Afsaneh, not only for her contributions to CAD modeling but for her patience and continual support. Thanks also to my father and mother who without their encouragement and endeavors, I would never be able to achieve my goals.

Contents

List of Tables

List of Figures

List of Acronyms

GIC	Geomagnetically Induced Current
MMF	Magnetomotive Force
HST	Hot Spot Temperature
CFD	Computational Fluid Dynamics
ONAN	Oil Natural Air Natural
ONAF	Oil Natural Air Force
OFAF	Oil Force Air Force
OFWF	Oil Force Water Force
ODAF	Oil Direct Air Force
ODWF	Oil Direct Water Force
TOT	Top Oil Temperature
GA	Genetic Algorithm
THN	Thermal Hydraulic Network

ON	Oil Natural
OD	Oil direct
FEM	Finite Element Method
LAEs	Linear Algebraic Equations
FVM	Finite Volume Method
FDM	Finite Difference Method
CV	Control Volume
PDE	Partial Differential Equation
Re	Reynolds number
Nu	Nusselt number
OIP	Oil Impregnated Paper
RIP	Resin Impregnated Paper
TEC	Thermal Equivalent Circuit
TTOT	Transformer Top Oil Temperature

List of Thesis Publication

Published:

1- **Milad Akbari**, Afshin Rezaei-Zare, " *Transformer Bushing Thermal Model for Calculation of Hot-Spot Temperature Considering Oil Flow Dynamics'"* IEEE Transactions on Power Delivery, Vol. 36, No. 3, 2021.

2- **Milad Akbari**, Afshin Rezaei-Zare, Muhammad Cheema, Tomasz Kalicki, " *Air Gap Inductance Calculation for Transformer Transient Model*", IEEE Transactions on Energy Conversion, Vol. 36, No. 3, 2021.

Accepted:

3- **Milad Akbari**, Mohsen Mostafaei, Afshin Rezaei-Zare, " *Estimation of Hot Spot Heating in OIP Transformer Bushings due to Geomagnetically Induced Current*" Accepted in IEEE Transactions on Power Delivery, 2022.

Submitted:

4- **Milad Akbari**, Afshin Rezaei-Zare, "*Heat analysis of transformers due to Geomagnetically Induced Current*" submitted in IEEE Transaction on Energy Conversion, 2022.

Chapter 1

Introduction

1.1 Background

The Geomagnetically Induced Current (GIC) is a phenomenon that happens during space weather or geomagnetic disturbances (GMD). It is regarded as one of the most dangerous space weather and solar activity occurrences. The regular bombardment of the earth by charged particles released by the sun is referred to as a solar storm. A geomagnetic disruption (GMD) happens when the solar storm's magnetic field is in opposition to the earth's. These disturbances, known as Coronal Mass Ejections (CMEs), are masses of electromagnetic fields and particles emitted by the Sun during solar activity. When CMEs approach, the Earth's magnetic field is distorted, resulting in a variable magnetic field on the ground [1] [2] [3]. By perturbing the Earth's magnetic field, GMDs may create quasi-dc surface voltages. In turn, these voltage potentials will generate low-frequency (0.1 mHz–0.1 Hz) geomagnetically induced currents (GICs) with amplitudes of 10–15 A and up to 300 A peak current for 1–2 minutes that flow in transmission lines and grids. As seen in Figure 1-1, Figure 1-2 and Figure 1-3, a number of GIC events have been documented by

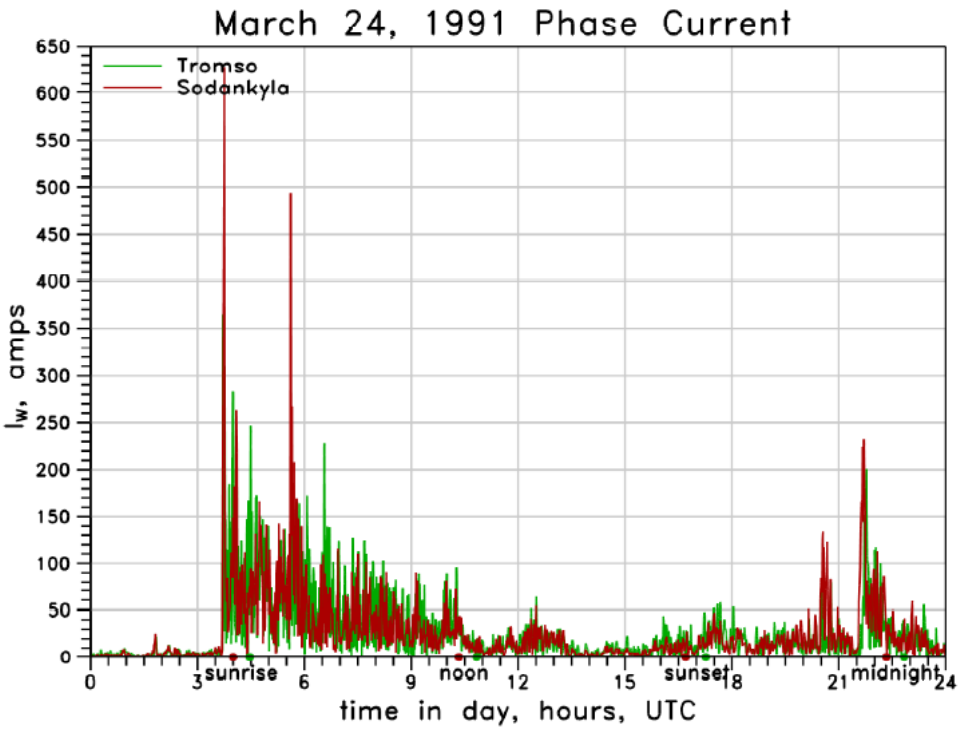

Figure 1-1. Real GIC event on March 24, 1991, the current peaks up to 630 A per phase [4].

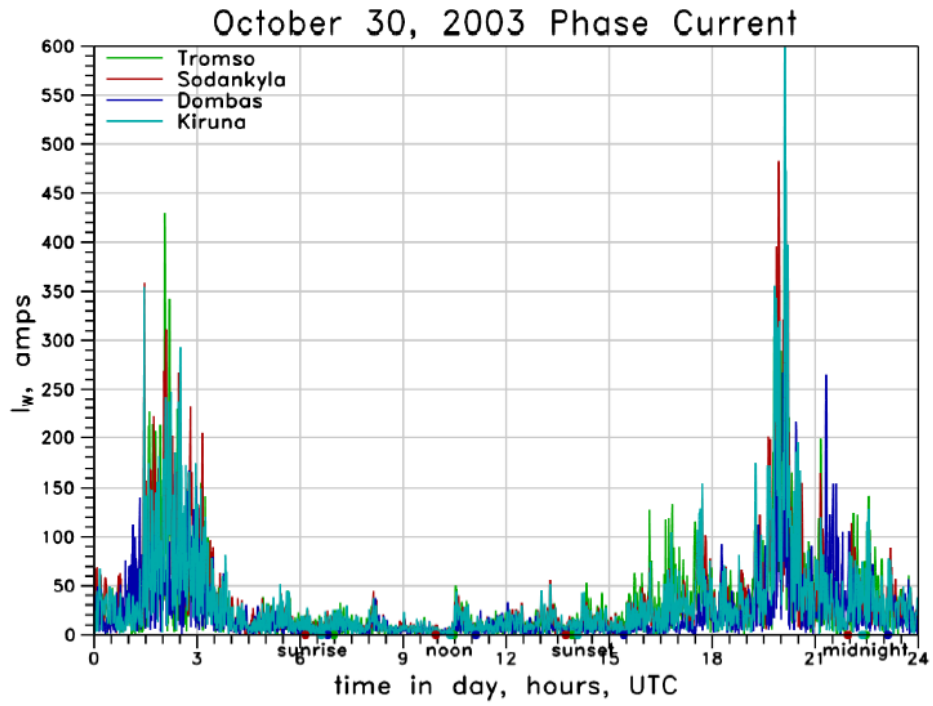

Figure 1-2. Real GIC event on October 30, 2003, the current peaks up to 600 A per phase [4].

various countries and areas [4]. In certain instances, the peak of GIC may approach 620 A for

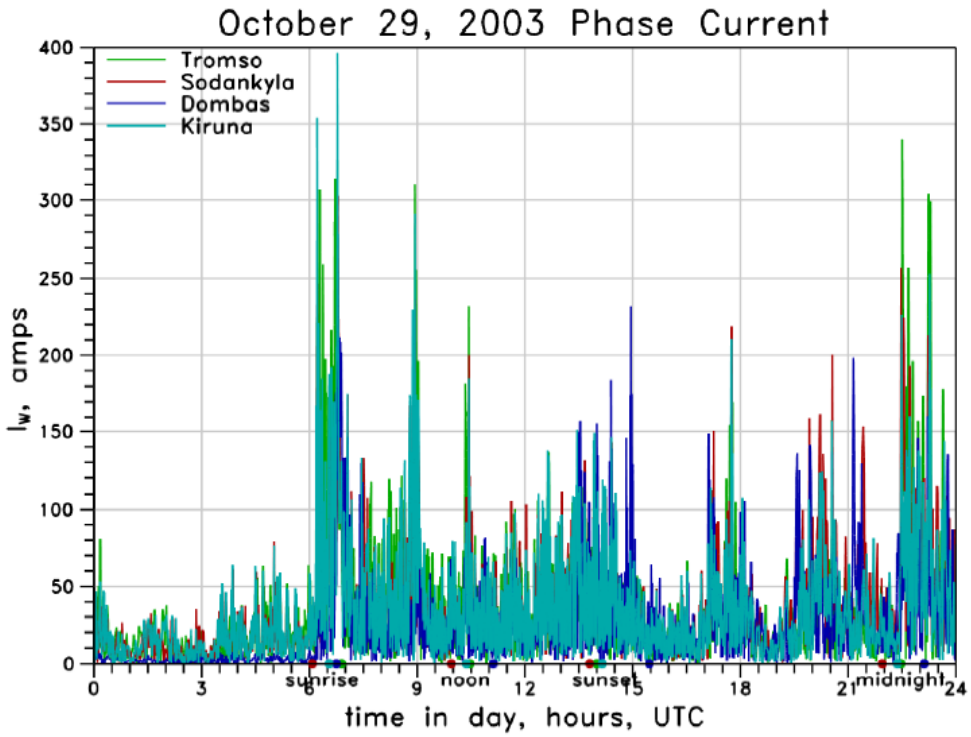

Figure 1-3. Real GIC event on October 29, 2003, the current peaks up to 350 A per phase [4].

several minutes. In addition, these instances indicate that the GIC may have a duration of several hours with a peak of more than 100 A.

1.2 Effect of GIC on Power Transformers

Demand for electricity is set to increase further as a result of industrial development with the electrification of transport and heat, and growing demand for connected digital devices. Electric power systems are responsible for providing customers with reliable electricity. These complex systems are designed and operated to generate, transmit, and distribute electricity, as shown in Figure 1-4. The essential elements of conventional power systems are power plants, power transformers, transmission and distribution lines, and customers. Among them, the power transformer is of paramount importance and is one of the most useful electrical devices ever invented.

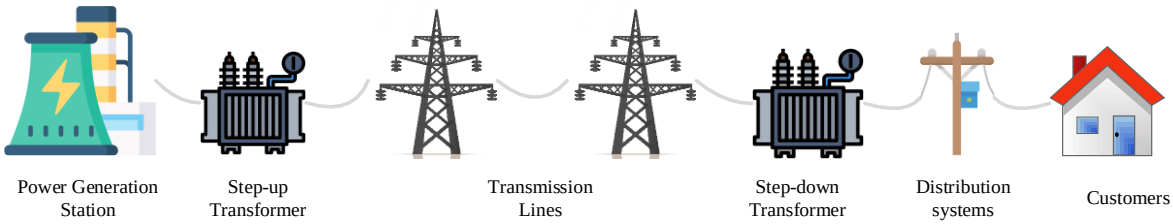

Figure 1-4. Conventional power system elements

Transformers are electrical devices that change or transform voltage levels between two circuits. They can raise or lower the voltage or current in an ac circuit, isolate circuits from each other, and increase or decrease the apparent value of a capacitor, an inductor, or a resistor. Furthermore, the transformer enables us to transmit electrical energy over great distances and distribute it safely in factories and homes [5], [6]. From the technical viewpoint, a transformer is an electromagnetic device with two or more stationary coils coupled through a mutual flux. Ferromagnetic cores are used to provide tight magnetic coupling and high flux densities. Such transformers are known as iron core transformers [7].

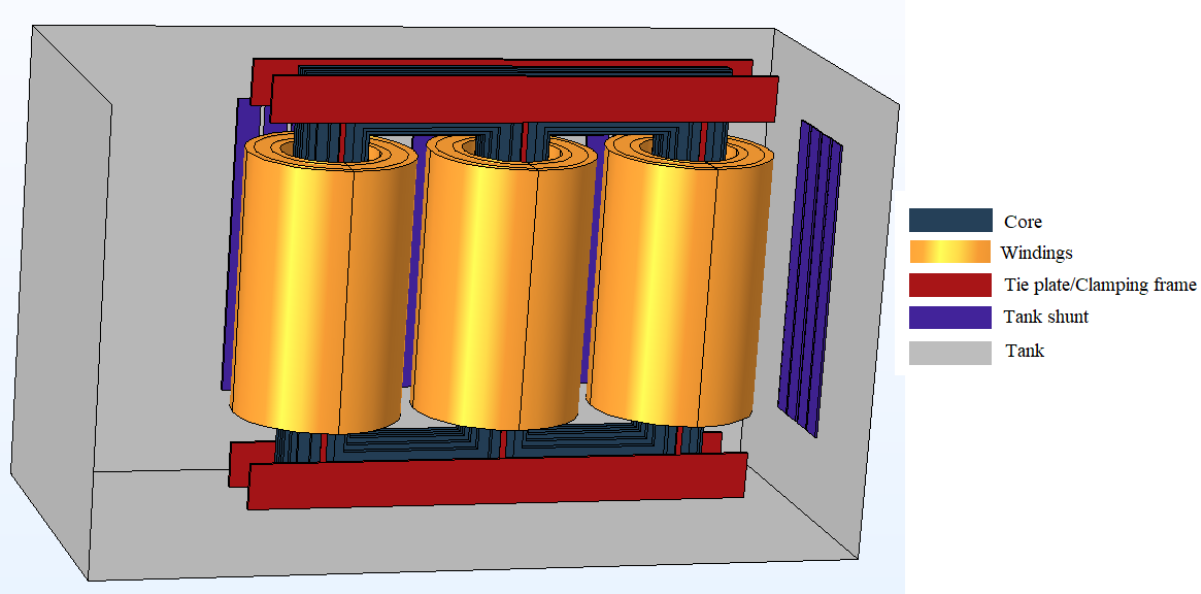

Figure 1-5. A 3D view of a three-legs transformer

The main components of a transformer are the core, windings, insulation and cooling systems,

bushing, tap changer, tank, and structural parts, some of which are shown in Figure 1-5 for a three-legs three-phase transformer.

The core of transformers is responsible for creating the magnetic circuit, one of the most important active parts of a transformer. The magnetic circuit consists of a laminated iron core and carries flux linked to windings. Energy is transferred from one electrical circuit to another through the magnetic field carried by the core. The iron core provides a low reluctance path to the magnetic flux thereby reducing magnetizing current [8]. As discussed before, the core is the primary source of transformer losses since it creates no-load losses. The load losses come from the aggregation of the winding losses with the stray eddy current losses. Hence, determining core loss is very important to transformer manufacturers as it enables them to design transformers to meet specific customer requirements [9]. The no-load losses, consisting of hysteresis loss and eddy loss, are minimized using a better grade of core material and thinner laminations [8].

Windings are conductors formed in different shapes such as helical, disc, and cylindrical, which generates Magnetomotive Force (MMF) carried by the core to other windings. The number of turns and the current in the winding primarily determine the choice of winding type. For the core type transformers, cylindrical windings with rectangular cross sections are widely used to utilize the available space effectively. With increasing conductor area, the conductor must be divided into two or more parallel conductor elements in order to reduce the eddy current losses in the winding. The rectangular-shaped conductor element is called a strand. Each strand is insulated either by paper lapping or by an enamel lacquer [10].

The tie plate (also called flitch plate) is located just outside the core in the space between the core and innermost winding. It is a structural plate that connects the upper and lower clamps. Tension in this plate provides the clamping force necessary to hold the transformer together should

a short circuit occur. It is usually made of magnetic or stainless steel and could be subdivided into several side-by-side vertical plates to help reduce the eddy current losses [11].

The tank is primarily the container for the oil and physical protection for the active part. It also serves as a support structure for accessories and control equipment. Before filling the oil, the tank with the active parts inside it is evacuated to remove all air that would endanger the dielectric strength of the transformer insulation. Hence, the tank is designated to withstand the pressure from the atmosphere with minimum deformations [10]. The shape of tank is rectangular cubic and made of soft magnetic steel with a thickness of about a few centimeters [8].

Bushings are one of the most important components of transformers. They provide the necessary insulation between the winding electrical connection and the tank, which is at earth's potential. Bushings also provide required insulation in the external medium [10]. The two most common types of bushings used on transformers as main lead entrances are solid porcelain bushings on smaller transformers and oil-filled condenser bushings on larger transformers. Solid porcelain bushings consist of high-grade porcelain cylinders that conductors pass through. High voltage bushings are generally oil-filled condenser types. Condenser types have a central conductor wound with alternating layers of paper insulation and tin foil filled with insulating oil. This results in a path from the conductor to the grounded tank, consisting of a series of condensers. The layers are designed to provide approximately equal voltage drops between each condenser layer [12].

GIC events have the most significant impact on power transformers linked to transmission lines. The GIC enters the star-connected windings of the transformer via the neutral ground point, and it is distributed evenly across all three phases [3], [13], [14]. When zero-sequence quasi-dc currents such as GIC flows through the transformer windings, a DC magnetic flux is produced in the core,

the size of which is proportional to the GIC flow. This DC flux is subsequently overlaid on the AC flux in such a manner that the magnetic cores of the transformers experience asymmetrical saturation, known as half-cycle saturation, as shown in Figure 1-6. The saturation of the transformer causes a number of significant issues, the most significant of which are overheating, the formation of harmonics, and a rise in the use of reactive power [15], [16]. The saturation curve of the transformer's core is shifted by one-half of a cycle in the opposite direction, depending on the direction of the GIC. During the half-cycle, when the magnitude of the magnetic flux is greater,

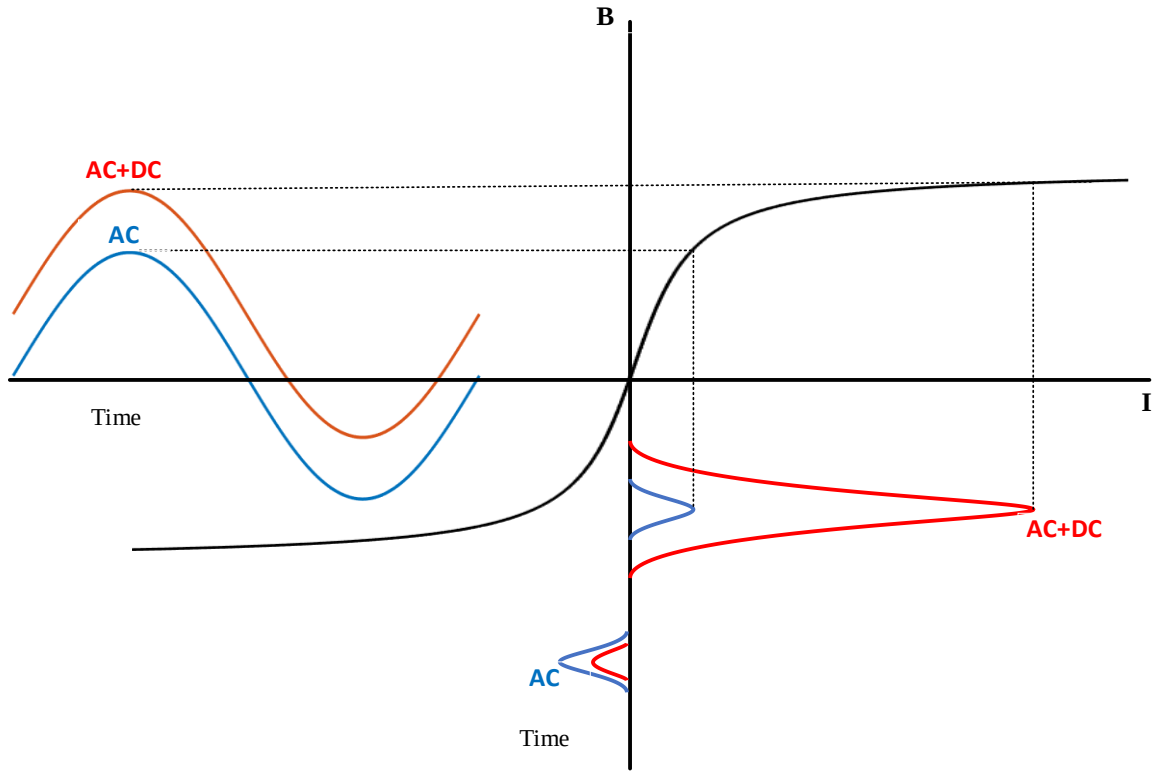

Figure 1-6. Half-cycle saturation of transformer core during GIC.

the operating point of the transformer moves closer to the saturation area. Because of the 90-degree phase angle difference between the exciting current and the voltage, the transformer consumes a significant amount of reactive power. This is because of the discrepancy. The most crucial issue that arises from the half-cycle saturation is generating hot spot heating in different transformer

parts.

Unlike normal conditions, when half-cycle saturation occurs, a bigger portion of the flux escapes outside the core since there is no return magnetic path in the core. This causes more eddy currents in several transformer components, including core, winding, and structural parts like the tie plates, clamping beams, and the tank. The result is extra heating in these areas, which may result in gassing or at least result in faster aging of the cellulose insulation owing to thermal breakdown [17]. Both of these outcomes are undesirable.

1.3 Motivation

Power Transformers are one of the most critical and expensive pieces of equipment in power systems. They play a vital role in the interconnection of power systems at different voltage levels, and without them, it would not be possible to use electric power in the many ways it is used today. Furthermore, they can isolate circuits from each other and increase or decrease the apparent value of a capacitor, an inductor, or a resistance [5]. The reliable and efficient fault-free operation of the high-voltage transformer has a decisive role in the availability of electricity supply. In recent years, there has been growing interest in the condition assessment of transformer insulation. This is because of the increasingly aged population of transformers in utilities around the world. With the growing complexity of power systems, minimizing interruption to customers and service reliability is paramount. Transformer failure could take place in terms of tripping that results in an unscheduled or unseen outage. Hence, a good maintenance strategy is a crucial component to have in a power system in order to avoid unexpected failures, which is of great industrial interest [18]–[20].

The transformer oil-paper insulation gets degraded under a combination of thermal, electrical,

chemical, mechanical, and environmental stresses during its operation. Among those, thermal stress is of paramount importance because it is a critical factor during the operation of transformers. In fact, the temperature of a transformer has a major impact on the life of the insulation. Continuous online monitoring of the transformer oil temperature, along with a thermal model of the transformer, can give an estimate of the loss of life of the transformer due to overheating [21]. However, the multi-physics behavior of transformers and the nonlinearity of some transformer parameters make thermal transformer modeling a challenging task.

Furthermore, to meet the accelerating demand for electricity, power utilities tend to overload transformers instead of replacing the new ones to minimize costs. The high demand on generation and transmission of electricity combined with modified load cycles can lead to load flows not planned before. During an overload circle, accelerated aging and damage must be strictly avoided [22]. However, the hot spot temperature of transformers limits the overload capability. The loading capability of transformers depends strongly on their thermal conditions, which can be investigated by means of a dynamic thermal model [23]. As a result, the thermal modeling of transformers plays a vital role in the design and operation stage.

Since the transformers are in a great danger during the GIC, it is vital to estimate the HST of different parts. However, the thermal impacts of this natural disaster have not been adequately investigated. This thesis aims to develop a more accurate transformer model for representing the thermal behavior of transformers, especially during transient phenomena such as Geomagnetically Induced Current (GIC).

To do that, an electromagnetic-thermal research of a transformer is then conducted under both normal and GIC circumstances. It is demonstrated that the structural components, such as the tank, clamps, and tank shunts, are highly saturated with GIC. However, increasing currents cause the

transformer core to become saturated, which causes more stray losses in the structural components. The tank is the component that is most at risk, according to the results. On the basis of the FEM-modified thermal equivalent circuit (TEC) model, also, a novel method is suggested for calculating the HST of OIP bushings in both steady-state and transient.

In this thesis, a 3-phase, 3-leg, core type transformer with Y-Y connection is considered. It is because, this type of the transformer is widely used in the power systems and more prone to face GICs. The GIC study is also performed under no-load conditions. All thermal analysis is based on 30 ^{0}C ambient temperature. For the bushing, it is assumed that the current rating is the same as transformer current rating.

1.4 Outline of the thesis

In this thesis, the low and mid- frequency electromagnetic modeling of transformers is discussed in Chapter 2. It is shown that the inductance of airgap between the core and tank has a significant effect on the GIC studies. Because of that, a correction factor is proposed to accurately calculate the airgap inductance based on the analytical formula. Then, all types of transformers' thermal modeling, including steady-state and dynamic loading models, are discussed, and previous research works are reviewed in Chapter 3. Chapter 4 describes the governing equations for electromagnetic-thermal-fluid analysis of a power transformer. Then, a case study is modeled to perform electromagnetic-thermal analysis under normal and GIC conditions. Chapter 5 provides a literature review of transformer bushings and proposes a novel transformer bushing thermal model which is more accurate than previous works. In addition, the HST of the bushings is obtained under GIC, and a simple yet precise model is developed to estimate the HST of the bushing under such transient events. Finally, the conclusion and future works are presented in chapter 6.

Chapter 2

Advanced Electromagnetic Transformer Model

2.1 Introduction

Electromagnetic modeling of transformers is immensely complicated due to the nonlinear and frequency-dependent parameters of transformers. One use of this kind of modeling is the calculation of winding currents under various situations, such as short-circuit, switching, and inrush. Other design tools, such as FEM software simulation, may use these currents to calculate stresses and do thermal analyses. The needed precision and sophistication of the model are determined by the study's objectives. Also, the frequency range is an essential feature that impacts the level of model complexity [24]. In this thesis, the investigation of the DC magnetization of power transformers will focus on the spectrum of mid and low-frequency transients.

Most of the transformer models are only modeling the transformer windings and iron core. Each

component of the transformer model serves a distinct purpose depending on the nature of the research being conducted. In ferroresonance simulations, for instance, core representation is essential but is often overlooked in load-flow and short-circuit computations [25]. In general, the transformer models are categorized into three groups, including Matrix Representation (BCTRAN model) [26], Saturable Transformer Component (STC model) [27], [28], and Topology-Based models, which are divided into two sub-groups of Duality-based [29] [30] and Geometric Models [31].

The leakage inductance approach, BCTRAN model, and topological models have been frequently employed for the investigation of transformer transients among the available transformer models. While BCTRAN's depiction of leakage fluxes inside and between phases is highly accurate and flexible, it lacks a core topology and nonlinearities model because it is based on a matrix representation. Topological transformer models, on the other hand, are able to depict the leg, yoke, and windings of a transformer, but they do not adequately account for leakage fluxes. To address these limitations, the implemented method combines the models into a hybrid model.

2.2 Components of the transformer model

The components of the chosen transformer model [32] is shown in Figure 2-1. As can be seen, the model includes the magnetic core equivalent, leakage inductance equivalent, winding turn ratio, winding resistance, and winding capacitances.

The transformer model is dependent on the transformer type. As this thesis focuses on the three-phase three-legs transformer, the transformer model of this type is presented in this section. The equivalent duality-based electric circuit of the transformer with the construction of Figure 2-2(a) is depicted in Figure 2-2(b). The derivation of the magnetic circuit equivalent is based on the

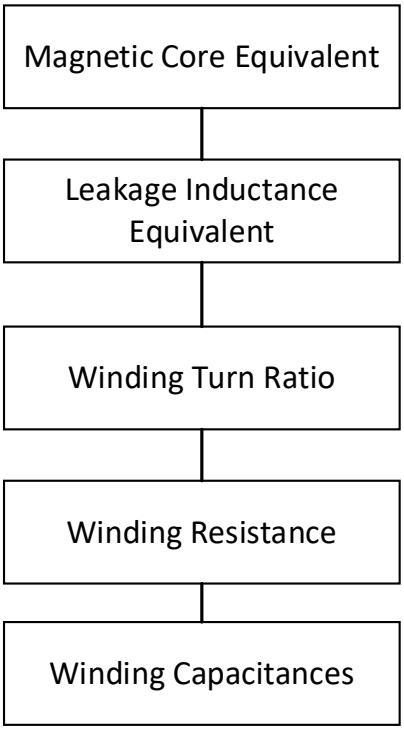

Figure 2-1. Components of electromagnetic transformer model.

duality principle, which refers to a common number of windings. Unlike the single-phase transformer, the phases are magnetically linked in the three-phase transformer. In the equivalent circuit of Figure 2-2(b), L_{0-air} is the inductance of air path surrounding the outer most winding, L_{shield} is the inductance of tank magnetic shield, and $L_{air-shield}$ is the inductance of the linking flux air paths to the magnetic shield. Also, L_{yoke} is the equivalent of top and bottom parts of the yoke between the two associated adjacent limbs. Finally, L_{mA}, L_{mB}, and L_{mC} represent the hysteretic characteristics of the main limbs.

The leakage inductance equivalent is a linked inductive network and connects the magnetic circuit equivalent to the ideal transformer. It can be modeled in a matrix form or based on a magnetically coupled circuit equivalent based calculated from the standard test data. The turn ratio of windings is represented by the ideal transformer, which isolates the magnetic part from the

winding's capacitance and resistance. The winding resistance is also can be modeled by the frequency-dependent circuits, such as Series Foster [33] and the Cauer equivalent circuits [34] shown in Figure 2-3. Finally, the capacitances of the windings are obtained from the routine dielectric tests of the transformer.

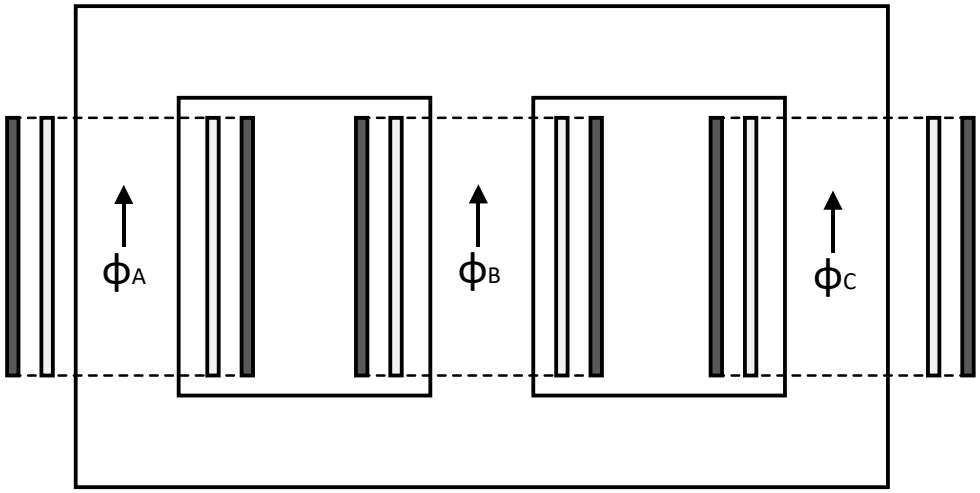

(a)

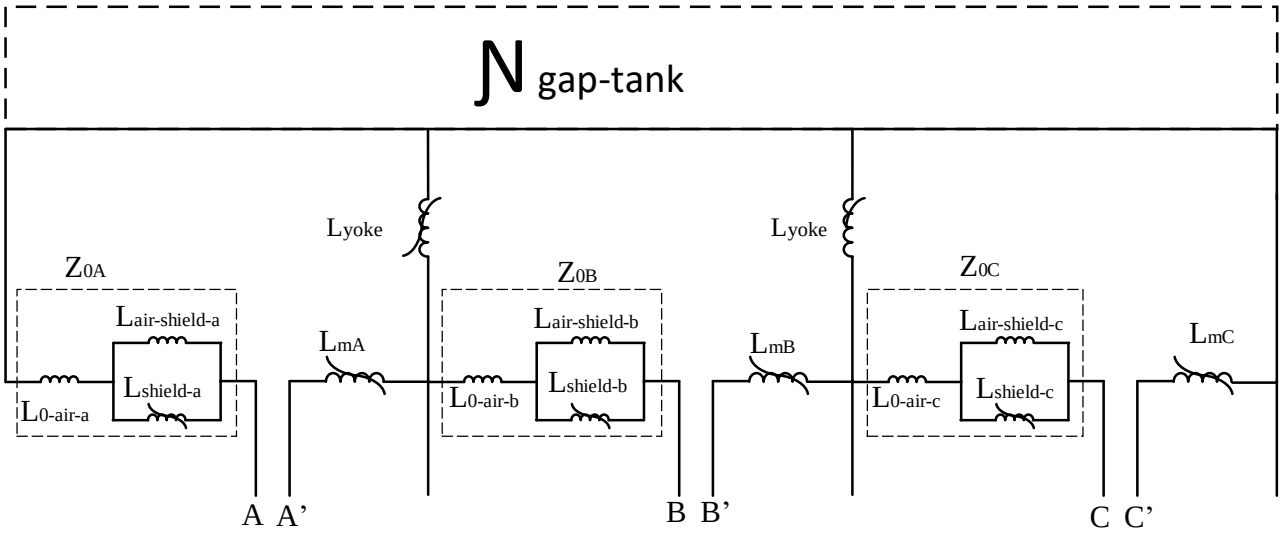

(b)

Figure 2-2. Three legs core construction (a), and its duality-based equivalent circuit (b)

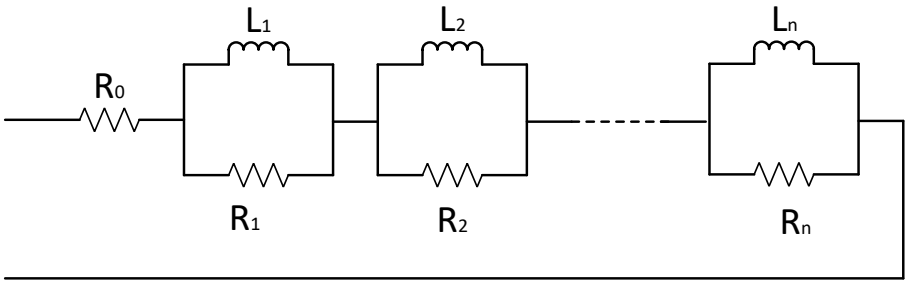

(a)

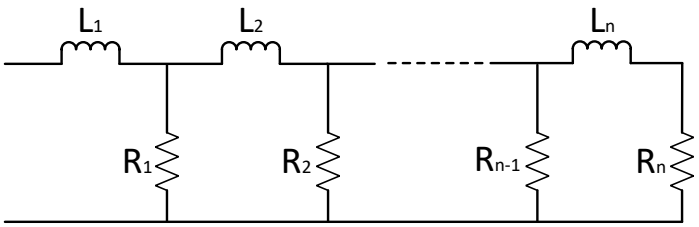

(b)

Figure 2-3. Frequency dependent circuit equivalents to represent the winding resistance: (a) Series Foster circuit and (b) Cauer circuit.

The last component in the transformer model is the equivalent network of the tank and the air gap, which is shown as $\mathcal{N}_{gap-tank}$ in Figure 2-2. This network is the main source of the power loss in the transformer zero-sequence tests. Since the yokes represent the high inductances during the zero-sequence test, the $\mathcal{N}_{gap-tank}$ is connected in series with L_{0-air}. As the GIC is a zero-sequence current, an accurate estimation of $\mathcal{N}_{gap-tank}$ parameters is vital in GIC studies. On the other hand, as explained, all transformer model parameters can be obtained by the standard tests except the parameters of $\mathcal{N}_{gap-tank}$. The concept of the hybrid model is elaborately explained in [35]. However, this model suffers from inaccuracy in calculating the air gap and tank inductances of $\mathcal{N}_{gap-tank}$. As these inductances play a vital role in the GIC studies, an accurate method based on FEM is proposed to modify the widely used analytical formula for air gap inductance

calculation.

2.3 Inductance Calculation of Air Gap Between Core and Tank

Despite numerous studies devoted to developing an accurate model of transformers [36][37], only a few can adequately represent the transformer structural parts and tank effects. Modeling these parts is vital for the determination of the transformer zero-sequence characteristic. Such a characteristic plays a vital role in the transformer's behavior under unbalanced operation and core saturation conditions. Nevertheless, many power transformers in service do not have sufficient zero-sequence data to allow an accurate analysis of the transformer behavior [37].

In most topological transformer models, zero sequence impedance is considered as a linear inductance in parallel with a resistance [25], which is not accurate due to the nonlinearity of the iron parts. Also, other models [37] with nonlinear zero-sequence characteristics suffer from some limitations pertaining to correct physical interpretation. In [32], a transformer model is proposed based on an enhanced topological representation of the transformer core, flux air paths, and tank. The model of [32] introduces the inductance of the air gap between the core and tank as a crucial parameter of the zero-sequence characteristic, with significant impacts on the observed behavior of the transformer under core saturation conditions, such as GIC and ferroresonance. An analytical method was employed to calculate the air gap inductance considering nonuniform air gap length and fringing flux effects [32]. For the simulated transformer under study with relatively small air gap, the model built based on the analytical result shows a good agreement with the experimental results of the GIC tests [35]. However, the accuracy of the analytical method requires to be verified for applying it to any transformer with different dimensions and core constructions.

In general, modeling the air gap reluctance and inductance is divided into two methods, i.e.,

analytical and numerical. The analytical methods such as [38] mainly use conformal mapping approaches to transform the main geometry to a well-defined geometry, obtain the inductance, convert the geometry back to its original shape and obtain its inductance. On the other hand, numerical solution techniques [38] using the finite element method (FEM), boundary element method (BEM), and boundary integral method (BIM) are accurate and form an important part of the design procedure. However, they require significant computing resources and modeling with a high computational runtime [38].

This section presents a new approach for calculating the air gap inductance of the transformer, considering the fringing flux between the transformer tank and core. The proposed model is based on both numerical and analytical techniques. First, the air gap inductance is calculated using FEM, and then a factor is proposed to correct the analytical result obtained from the traditional inductance calculation method. The FEM results are also compared with the analytical results deduced from the conformal mapping [32]. Comparing the results of these methods shows significant differences, especially with the increase of the air gap length. To investigate the impacts of the values of different parameter on the transformer behavior, a detailed topological transformer model is developed in the EMTP-RV environment, and the transformer response to GIC is simulated in the time domain. The study results highlight the importance of the correct representation of the air gap inductance for the transformer transients.

2.3.1 Magnetic Circuit with Air Gap

Among the existing transformer models, duality-based magnetic circuit equivalent models have been widely used for the analysis of transformer transients. This model, which is a type of topology-based model, is derived from a magnetic circuit model using the principle of duality [25]. Figure 2-4 shows the flux paths and relevant reluctances for one leg of the transformer,

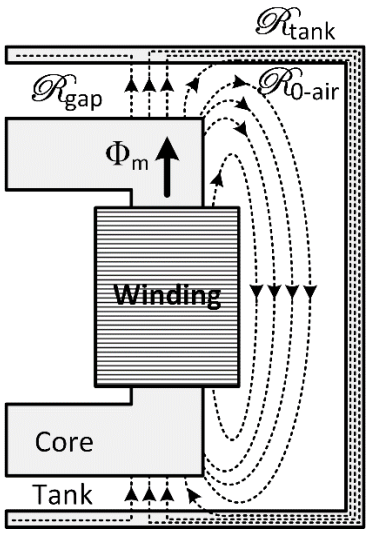

Figure 2-4. Flux paths for a transformer considering core, winding, and the tank.

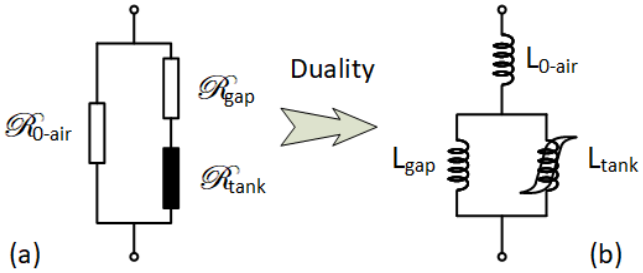

Figure 2-5. Off-core flux paths equivalent (a) magnetic circuit, and (b) dual electric circuit.

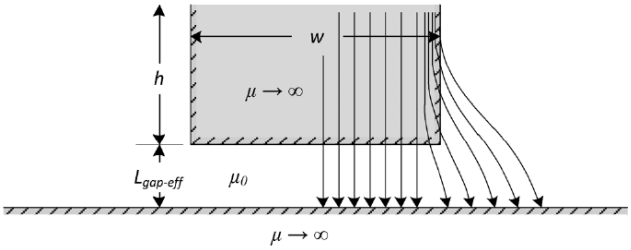

Figure 2-6. Increase of effective air gap area due to fringing flux between planar and rectangular iron surfaces.

considering the winding, core, and tank. $\mathfrak{R}_{gap}$ presents the reluctance of air gaps between the core and tank, $\mathfrak{R}_{tank}$ is the reluctance of tank, and $\mathfrak{R}_{0-air}$ is the reluctance of the shown air path flux. The equivalent circuit associated with the flux paths of Figure 2-4 is obtained as shown in Figure 2-5(a) which can be converted to the equivalent circuit of Figure 2-5(b), using the principle of

duality. The inductances L_{gap}, L_{tank}, and L_0 are the equivalent representations of $\Re_{gap}$, $\Re_{tank}$, and $\Re_{0-air}$, in the dual circuit respectively. Among these, finding L_{gap} is rather complicated because of two reasons. First, it is difficult to precisely determine the air gap length in non-uniform air gaps [25], and second, the fringing flux effect in the air and around the edges of the iron core makes the calculation of the effective cross-section area of the flux path difficult.

In the case of uniform air gap length, the air gap reluctance and inductance can be calculated using the traditional equations [32]:

$$\Re_{gap} = \frac{l_{gap}}{\mu_0 A_{gap}} \tag{2-1}$$

$$L_{gap} = \frac{N^2}{\Re_{gap}} \tag{2-2}$$

where l_{gap} is the mean length of the air gap, A_{gap} is the cross section area, μ_0 is the permeability of the air, and N is the winding number of turns. For very small air gaps, ((2-1) and (2-2) yield acceptable results due to low fringing flux effects. However, due to considerable air gap length in transformers, fringing flux affects the reluctance. In addition, the air gap length between the tank and the yoke is nonuniform. Hence, as proposed in [32], ((2-1) should be modified as

$$\Re_{gap} = \frac{l_{gap-eff}}{\mu_0 A_{gap-eff}} \tag{2-3}$$

with the effective air gap length $l_{gap-eff}$and effective area $A_{gap-eff}$ which are affected by the nonuniform air gap and the fringing flux, respectively. In order to calculate these effective variables, the following fringing flux factor (FFF) is defined based on a conformal mapping approach [32],[38]

$$FFF = 1 + \frac{4l_{gap-eff}}{w\pi}(1 + \ln(\frac{\pi h}{4l_{gap-eff}})) \quad (2\text{-}4)$$

where *w* and *h*, in Figure 2-6, are the width and height of the unwound part of the transformer leg. Although [38] showed the accuracy of ((2-4) with the FEM model, but it is acceptable for very short air gap lengths and is not verified for larger air gaps.

A solution that considers both the nonuniform air gap length and fringing flux for any air gap length is to employ an inductance enhancement factor (IEF) based on the FEM model to correct the air gap inductance calculated by the traditional method. With this proposed factor, not only the nonuniformity of air gap length and the fringing flux effects are considered, but also the lengthy setup and elaborate modeling of FEM is avoided. Hence, the following IEF is defined as

$$IEF = \frac{L_{FEM}}{L_{gap}} \quad (2\text{-}5)$$

where L_{FEM} is the air gap inductance based on the FEM model, and L_{gap} is calculated based on ((2-1) and (2-2).

2.3.2 Results and Discussion

In order to show the limitation of FFF given by ((2-4), the airgap inductance between the planar and a rectangular iron surface, Figure 2-7, is calculated with both ((2-4) and the FEM method. Figure 2-7 shows the magnetic flux density and the fringing flux paths in the vicinity of the air gap with white lines, which is constructed and simulated by the FEM model.

Since the two important factors are air gap distance l_{gap} and the surface of rectangular iron w, they are considered as variables while h is constant. The air gap inductance is calculated for the different ratios of l_{gap}/w to compare IEF with FFF, which is shown in Figure 2-8. The results show that FFF matches well with IEF for very short air gaps, up to about l_{gap}/w=0.18. However,

increasing the ratio of l_{gap}/w leads to significant difference between FFF and IEF. For instance, with l_{gap}/w=0.5 and l_{gap}/w=1 the IEF is 10.3% and 23.5% higher than FFF, respectively.

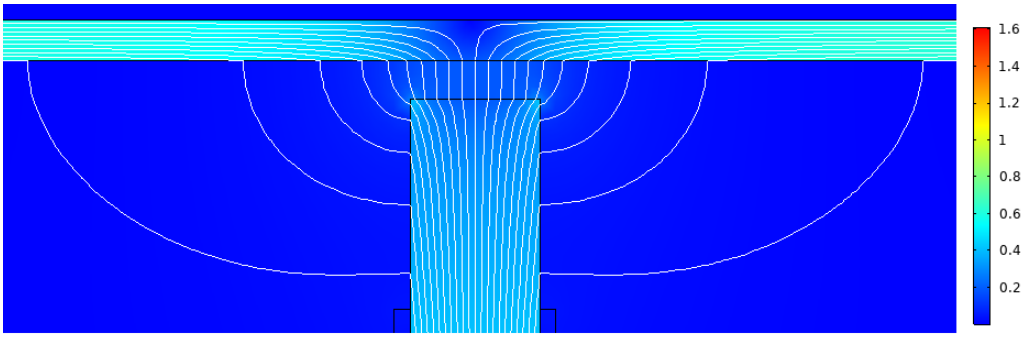

Figure 2-7. FEM model showing the magnetic flux density (T), including fringing flux paths.

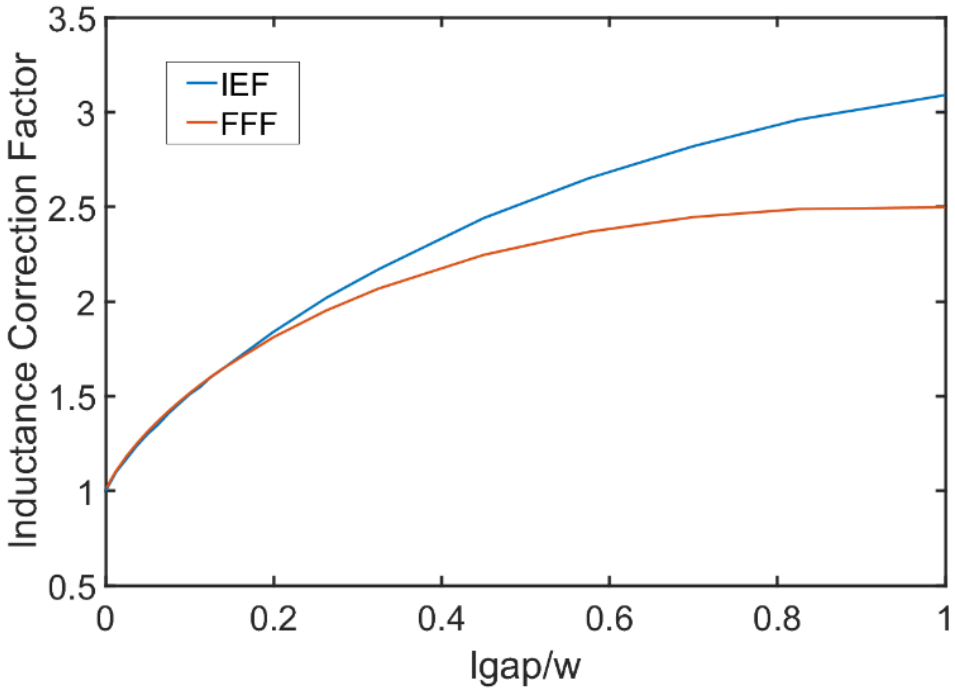

Figure 2-8. The comparison between IEF and FFF based on different l_{gap}/w ratio

This noticeable difference can have profound effects on the low and mid-frequency transients of power transformers, such as the transformer response due to GIC. During geomagnetic disturbance (GMD), the GIC flows in the system transformers with grounded neutrals. The GIC magnitude and polarity in all phases are identical and constitute a zero-sequence current in the transformer.

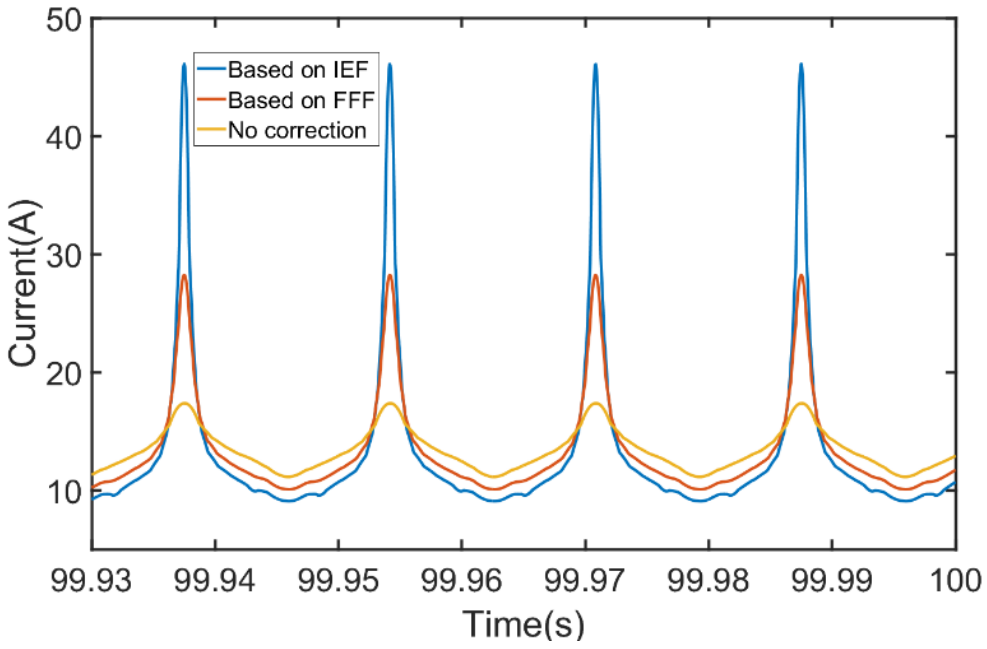

Figure 2-9. Magnetizing current of a 230/27.6kV three-phase 3-leg transformer based on two air gap inductances obtained from FFF and IEF, under the neutral GIC of 40A

Hence, the zero-sequence characteristic of the transformer is of paramount importance under the GIC conditions [35]. To investigate the difference between the estimated air gap inductances from FFF and IEF, the GIC injected from the grid into the HV side of a 230/27.6kV three-phase, 3-leg transformer is simulated in the EMTP-RV. The detailed transformer model of [32], [35] is adopted in this study, and the saturation level of the transformer under the neutral GIC of 40A is investigated by analyzing the core magnetizing current. Figure 2-9 compares the phase-A magnetizing currents of the transformer HV winding with the air gap inductances obtained from FFF and IEF and for $l_{gap}/w=0.75$. The peak of the currents is 28.07 A and 46.1 A for FFF and EIF, respectively, corresponding to a difference of 64.23%. These results clearly demonstrate the noticeable difference in transformer response to the GIC with different air gap inductances.

2.4 Transformer Current under GIC Conditions

As discussed before, the zero impedance characteristics play a prominent role in GIC studies.

It was also shown that the analytical method may not be sufficient to obtain such characteristics. Although we proposed a FEM-based correction factor for the analytical formula, a detailed 3D FEM model of the case study transformer is modeled in COMSOL Multiphysics to calculate the zero-sequence characteristics. The details of modeling with geometry and material specification are presented in section 4.3.

In order to consider the saturation of structural parts as well as the core, the nonlinear relation between the magnetic flux density *B* and the magnetic field intensity *H* is considered based on [39]. Figure 4-2 and Figure 4-5 illustrate the B-H curve for the core and structural parts, including the tank and clamping plates, respectively. As can be seen, the tank and clamping plates will be saturated at 1.85T. Also, the core remains unsaturated up to 2.1 T.

When determining the zero sequence characteristics, a DC current of the same amplitude and direction is injected into each winding, and the magnetic flux for each of the three phases is then computed. For currents up to 100A, the magnetic flux values are shown in Table 2-1. As predicted, the magnetic flux rises as the current increases.

The outcome of Table 2-1 is utilized to modify the transformer model described in [32], [35], and then to calculate the magnetizing current during the GIC. The proposed model is implemented in EMTP-RV for the case study which is a 3-legs, 3-phases 125 MVA autotransformer with the rated voltages of 230/115 kV. The induced voltage in the ground is responsible for GIC; thus, it flows into transmission lines linked to transformers with a grounded neutral. In this study, the autotransformer is connected to a 230kV power system through a transmission line with a resistance of 0.6607 Ω/phase. In addition, the connection of the HV winding is the neutral star. The size of the GIC for a given GMD is governed by the system resistances, with the dominant transmission line resistance being the most important factor. This is because the GIC has a quasi-

dc characteristic.

Table 2-1. Zero sequence characteristics for the case study autotransformer

Current (*A*)	Φ_A *(wb)*	Φ_B *(wb)*	Φ_C *(wb)*
1	0.010802	0.010819	0.010673
3	0.031903	0.03197	0.03157
5	0.052708	0.052835	0.052208
7	0.073261	0.073454	0.072617
10	0.10236	0.10268	0.10167
12	0.11939	0.11981	0.11878
15	0.14054	0.14099	0.13979
18	0.15909	0.15966	0.15812
20	0.1706	0.17124	0.16946
22	0.1816	0.18234	0.1802
24	0.19203	0.19286	0.19059
26	0.20213	0.203	0.20054
28	0.21171	0.213	0.21009
30	0.22124	0.22241	0.21968
40	0.26653	0.26853	0.26533
50	0.30848	0.31065	0.30792
60	0.34817	0.3499	0.34836
70	0.38574	0.38666	0.38644
80	0.42232	0.4218	0.42328
90	0.45825	0.45648	0.45976
100	0.49412	0.49077	0.49549

To examine the behavior of the transformer to the GIC injected from the transmission system, a dc voltage source is fed to the HV winding neutral of the transformer. The magnetizing current and its dc component, which is equivalent to the injected 200A GIC at neural (66.6A per phase), are shown in Figure 2-10. Because the transformer is saturated under GIC, the currents and voltages are distorted and consist of different harmonics. As seen in Figure 2-11, the current contains both odd and even harmonics up to harmonic thirteenth.

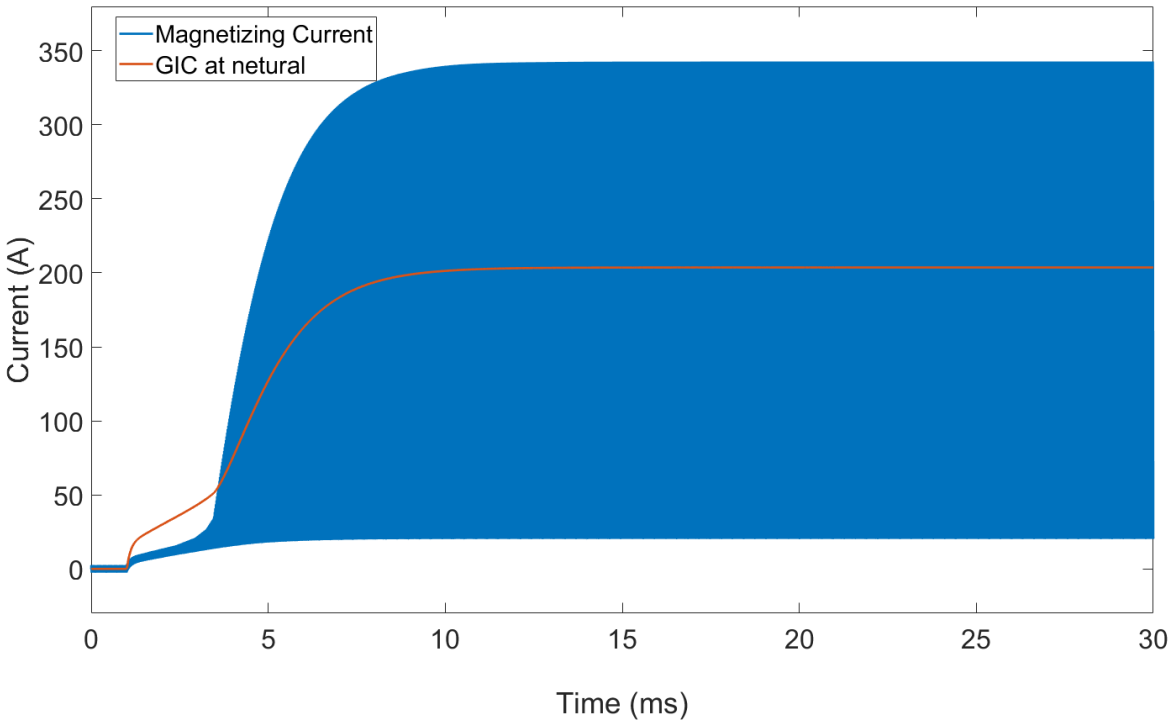

Figure 2-10. Magnetizing current under 200A GIC at neutral of the transformer

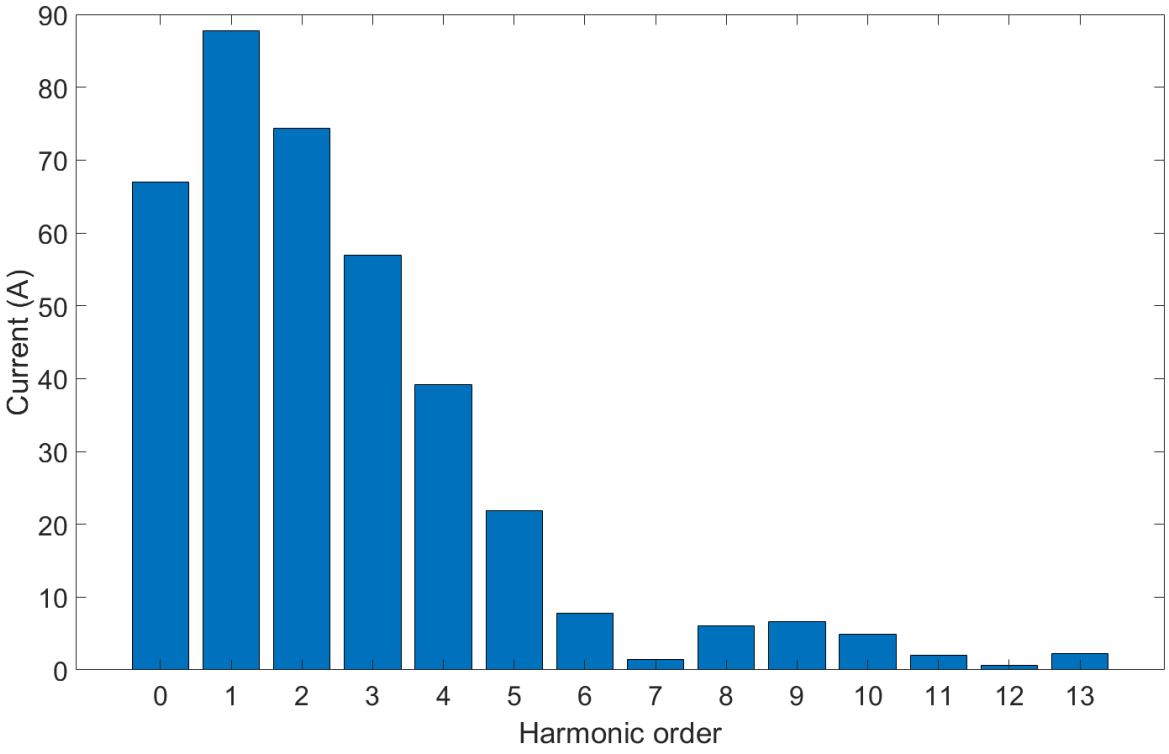

Figure 2-11. Harmonic order of the distorted current under 200A GIC at neutral

2.5 Conclusion

This chapter presents a new inductance enhancement factor (IEF) for calculating the air gap inductance of the transformers for the transformer topological model. The proposed IEF is derived from FEM, taking into account the fringing flux effects. The IEF is also compared with the analytical-based FFF method. It is shown that the FFF is accurate for small air gaps, and its error increases with the air gap length, whereas the proposed IEF can be used for any air gap length.

To demonstrate the effects of proposed estimation of the air gap inductance on the transformer behavior, the response of a three-phase 3-leg 230kV/27.6kV transformer is investigated with time-domain simulations under the neutral GIC of 40A. The study results show that the saturation level of the transformer is noticeably higher when the air gap inductance is calculated based on the proposed IEF as compared with the FFF method. The corresponding magnetizing currents reveal a 64.23% higher peak current for IEF-based air gap inductance compared with that of the FFF-based parameter. This study further highlights the significance of conducting a zero-sequence test as a part of the factory acceptance test of the transformers. Finally, the magnetizing current of the case study transformer is calculated under 66.6A GIC per phase using the modified method in EMTP-RV.

Chapter 3

Various Approaches for the Transformer Thermal Modeling

3.1 Introduction

Transformer losses are broadly classified as no-load and load losses. The no-load losses are composed of two components: (1) the hysteresis loss and (2) eddy current loss. The hysteresis loss is the energy loss when the magnetic material goes through a cycling state. The eddy current loss is caused when the flux lines pass through the core [40]. Load losses occur when the output is connected to a load so that current flows through the transformer from input to output terminals [11]. Losses of energy appear as heat which is the major cause of transformer temperature rise and its aging. Among the several factors that affect the transformer performance, the location of the maximum temperature of the solid insulation named ‘hot spot temperature’ (HST) and its temperature level have been identified as the main reasons for transformer aging and failures [41]–[43]. In fact, high temperatures in a transformer will drastically shorten the life of insulating

materials used in windings and structures. For every 8 degrees Celsius (°C) temperature rise, the transformer's life is cut by one-half; therefore, maintaining cooling systems is critical [12]. In worst cases, the high HST may lead to transformer failure and explosion. When the internal temperature of a transformer reaches 150–300 °C under abnormal conditions, the mineral oils produce hydrogen and methane gases due to chemical decomposition. At temperatures above 300 °C, ethylene is formed, and above 700°C, large amounts of hydrogen and ethylene are produced. These gases tend to dissolve partially or entirely in the mineral oil and can form combustible/flammable mixtures if they escape the transformer oil compartment, leading to unexpected fire/explosion accidents [44]. Consequently, excellent thermal design is paramount in transformer design since it determines insulation aging and life [45].

The thermal modeling of the transformer can be divided into two general categories [23]. The first category is physical and semi-physical modeling describing a transformer's complex heat transfer modes with simple differential equations such as correlation, lumped, and equivalent circuit models. The other category is the computational fluid dynamic (CFD) modeling approach based on numerical methods such as finite element and finite volume methods, which is very accurate but time-consuming and requires the design detail of the transformer for modeling.

3.2 Correlation Models

The simplest transformer models are based on a set of correlations that model the thermal behavior of the transformer under steady state and transient conditions using the results of experimental tests. The correlations consist of some thermal parameters which should be obtained by heat run tests. IEEE C57.91-2011 [46] and IEC 60076-7 [47] suggest well-known correlation models for estimating the hot spot temperature of transformers. In these models, the hot spot

temperature is assumed to consist of three components: the average ambient temperature, the top-oil rise over ambient temperature, and the winding hot spot rise over top-oil temperature. The standards present a set of correlations to calculate these components based on some parameters with a related estimation table for each.

Transformers usually operate on a load cycle that repeats every 24 h. Hence, the proposed models try to estimate the hot spot temperature of the transformer considering load variation. Based on the proposed thermal model in [46], the hot spot temperature is:

$$\theta_H = \theta_A + \Delta\theta_{TO} + \Delta\theta_H \tag{3-1}$$

where

θ_H is the winding hottest-spot temperature, °C

θ_A is the average ambient temperature during the load cycle to be studied, °C

$\Delta\theta_{TO}$ is the top-oil rise over ambient temperature, °C

$\Delta\theta_H$ is the winding hottest-spot rise over top-oil temperature, °C.

The top-oil temperature rise is calculated by the following expression:

$$\Delta\theta_{TO} = \left(\Delta\theta_{TO,U} - \Delta\theta_{TO,i}\right)\left(1 - e^{-\frac{t}{\tau_{TO}}}\right) + \Delta\theta_{TO,i} \tag{3-2}$$

where

$\Delta\theta_{TO}$ is the top-oil rise over ambient temperature, °C

$\Delta\theta_{TO,U}$ is the ultimate top-oil rise over ambient temperature for load *L*, °C

$\Delta\theta_{TO,i}$ is the initial top-oil rise over ambient temperature for $t = 0$, °C

e is the base of the natural logarithm

τ_{TO} is the oil time constant of transformer for any load *L* and for any specific

temperature differential between the ultimate top-oil rise and the initial top-oil rise, h.

The initial and ultimate top oil rise are calculated by:

$$\Delta\theta_{TO,i} = \Delta\theta_{TO,R}\left[\frac{K_i^2 R + 1}{R + 1}\right]^n \tag{3-3}$$

$$\Delta\theta_{TO,u} = \Delta\theta_{TO,R}\left[\frac{K_u^2 R + 1}{R + 1}\right]^n \tag{3-4}$$

where K_i, and K_u are the ratio of initial and ultimate load L to the rated load, per unit. Also, R is the ratio of load loss at rated load to no-load loss on the tap position to be studied. And finally,n is an empirically derived exponent used to calculate the variation of $\Delta\theta_{TO}$ with changes in load. The value of n has been chosen for each cooling model based on Table 3-1 [46].

Table 3-1. Proposed values of n for different types of cooling

Type of cooling	$\boldsymbol{n}$
ONAN	0.8
ONAF	0.9
Non-directed OFAF or OFWF	0.9
Directed ODAF or ODWF	1.0

3.3 Lumped Models

The correlation models [46], [47] are simple and generally acceptable. However, these models lead to a conservative estimation of HST, which is mainly settled on the thermal behavior of a specific transformer and needs detailed information that is not likely available or constant with the

time evolution [48],[49], [50]. Thus, researchers have tried to predict the HST of transformers more accurately. To do so, they have developed their estimation based on lumped models. This type of modeling consists of different components, and energy conservation is applied to each part. It is called a lumped model because it simplifies the description of behavior of the physical systems into a topology with discrete elements.

In [51], the authors develop a thermal model for an oil-immersed, forced air cooled transformer considering the transformer to be comprised of three major components: the core and coil assembly, the insulating oil, and the external transformer tank. For each of these components, an energy balance is performed, leading to three ordinary, first-order differential equations. Then, this set of equations is solved simultaneously using numerical methods to find the HST. However, the results show a major difference of 5 ^{0}C between the estimation and test results. Although the lumped models have a few drawbacks, such as losing information, but they offer equivalent circuits based on the thermal-electrical analogy, which makes the static and dynamic analyses easier [52].

3.3.1 Thermal-Electrical Analogy

Two systems are considered to be analogous when they both have similar equations and boundary conditions, and the equations describing the behaviors of one system can be transformed into the equations for the other by simply changing the symbols of the variables [53]. Thermal and electrical systems are two such analogous systems, as shown in Table 3-2. In the thermal-electrical analogy, temperature plays the role of voltage which causes heat to flow in a similar fashion to the flow of charge in an electrical circuit. Also, the two critical thermal parameters of a material such as cooling transformer oil are its heat capacity and thermal conductivity [54]. The electrical and corresponding thermal laws of resistance and capacitance are as follows:

$$v = R_{el}.i \quad and \quad i = C_{el}.\frac{dv}{dt} \tag{3-5}$$

$$\theta = R_{th}.q \quad and \quad q = C_{th}.\frac{d\theta}{dt} \tag{3-6}$$

where the symbols are defined in Table 3-2.

It should be mentioned that, for the heat transfer case, the thermal resistance may be non-linear as follows [54]:

$$\theta = R_{thR}.q^n \tag{3-7}$$

where R_{thR} is the rated value of R_{th}, i.e., the value for a known set of θ, q, and n.

Table 3-2. Thermal Electrical analogous quantities

Thermal Equivalent Circuit	**Electrical Circuit**
Temperature T	Voltage V
Heat flow Q	Current I
Thermal Resistance R_T	Electrical Resistance R
Thermal Capacitance C_T	Electrical Capacitance C
Heat Source	Current Source

G. Swift et al. [55], [56] present a simple equivalent circuit to represent the thermal heat flow equations for power transformers. The proposed equivalent circuit is shown in Figure 3-1, which consists of two winding-to-oil and oil-to-ambient models. In order to represent the effect of air or oil cooling convection currents, a nonlinear resistor is assumed. Also, the heat generated by power losses and ambient temperature are represented by current and voltage sources, respectively. This model considers three inputs, including the iron loss (q_{fe}), the copper loss (q_{cu}), and the ambient temperature. The oil thermal resistance (R_{oil}) is a combination of the oil and the interface resistance

with the moving air layers. In addition, the hot spot resistance (R_{hs}) consists of the insulation resistance and the interface resistance with the moving oil next to the insulation. It should be noted that, for the lumped capacitance, it is assumed that the temperature distribution within the medium (oil) is uniform at any given instant, which is a reasonable assumption [55].

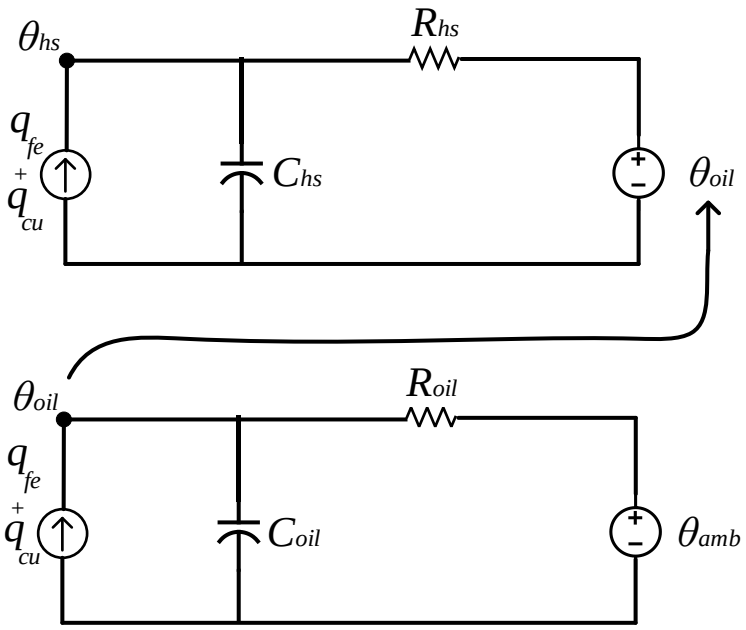

Figure 3-1. Simple equivalent circuit for calculating the HST proposed by [55], [56].

The differential equation related to Figure 3-1 for the oil-to-ambient model is:

$$q_{fe} + q_{cu} = C_{oil}.\frac{d\theta_{oil}}{dt} + \frac{1}{R_{oilR}}.[\theta_{oil} - \theta_{amb}]^{1/n} \tag{3-8}$$

where C_{oil} is the thermal capacitance of the oil, and R_{oilR} is the thermal resitance of the oil at rated conditions. If we define R as the ratio of q_{cu} and q_{fe} at rated load, then ((3-8) reduces to:

$$\frac{I_{pu}^2 R + 1}{R + 1}.[\Delta\theta_{oilR}]^{1/n} = \tau_{oil}.\frac{d\theta_{oil}}{dt} + [\theta_{oil} - \theta_{amb}]^{1/n} \tag{3-9}$$

where $\Delta\theta_{oilR}$ is the difference of θ_{oil} and θ_{amb} at rated load, and τ_{oil} is the oil time constant which can be obtained as follows:

$$\tau_{oil} = R_{oilR} C_{oil} \tag{3-10}$$

Hence, the difference equation corresponding to (3-9 is:

$$D\theta_{oil} = \frac{Dt}{\tau_{oil}} . \left[\frac{I_{pu}^2 R + 1}{R + 1} . [\Delta\theta_{oilR}]^{1/n} - [\theta_{oil} - \theta_{amb}]^{1/n} \right] \tag{3-11}$$

where *D* is the difference operator, indicating a slight change in the associated variable.

As is shown in Figure 3-1, the winding-to-oil model is analogous to the oil-to-air model. So, the equation for calculating the θ_{hs} would be similar to ((3-11).

In [57], an equivalent heat circuit is presented to model the thermal behavior of an oil-immersed power transformer based on its actual heat transfer mechanisms. Unlike [55], in this model, the top-oil temperature (TOT) and the bottom-oil temperature are considered for obtaining the HST. Figure 3-2 shows the basic transformer heat exchange schematics, which shows how generated heat by losses is transferred into the oil. It also illustrates a transformer's three cooling mechanisms, including conduction, convection, and radiation. In this schematic, Q_{fe} and Q_{cu} represent the core and copper losses, G1 is the heat conductance of winding to the oil, G2 is the heat conductance of core to the oil, G12 is the heat conductance of heat exchange between the winding and core, and G3 is the heat conductance of oil to the tank and cooling medium.

The electrical equivalent circuit corresponding to the heat exchange schematic of Figure 3-2 is shown in Figure 3-3. In the proposed model [57], the transformer is comprised of four main components, including core, core assembly, insulating oil, and transformer tank and external cooler. Each node shows an average temperature of a part of the transformer, such as windings, transformer oil, and core.

The parameters of the equivalent circuit [57] are as follows:

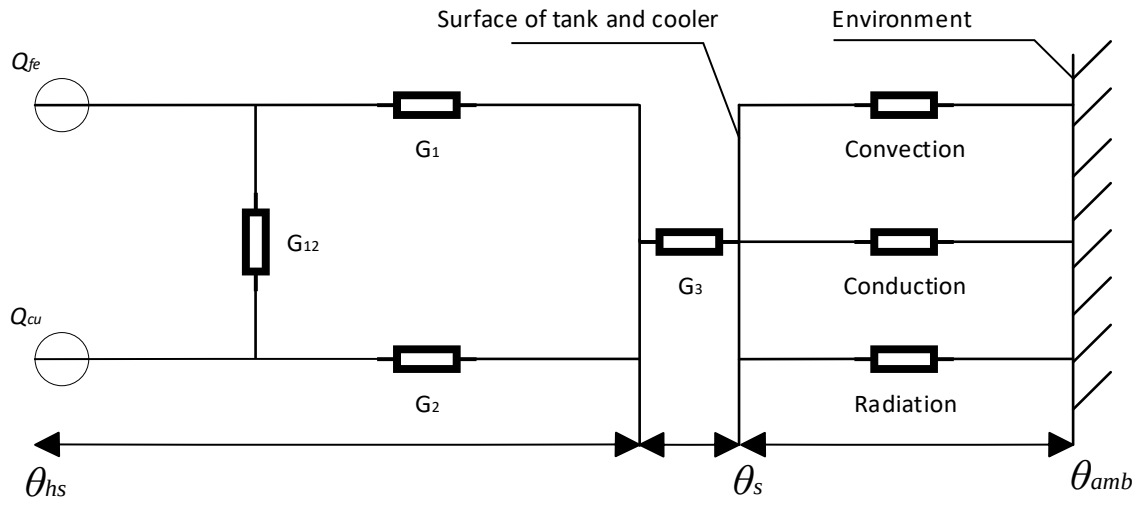

Figure 3-2. Basic transformer heat exchange mechanism [57].

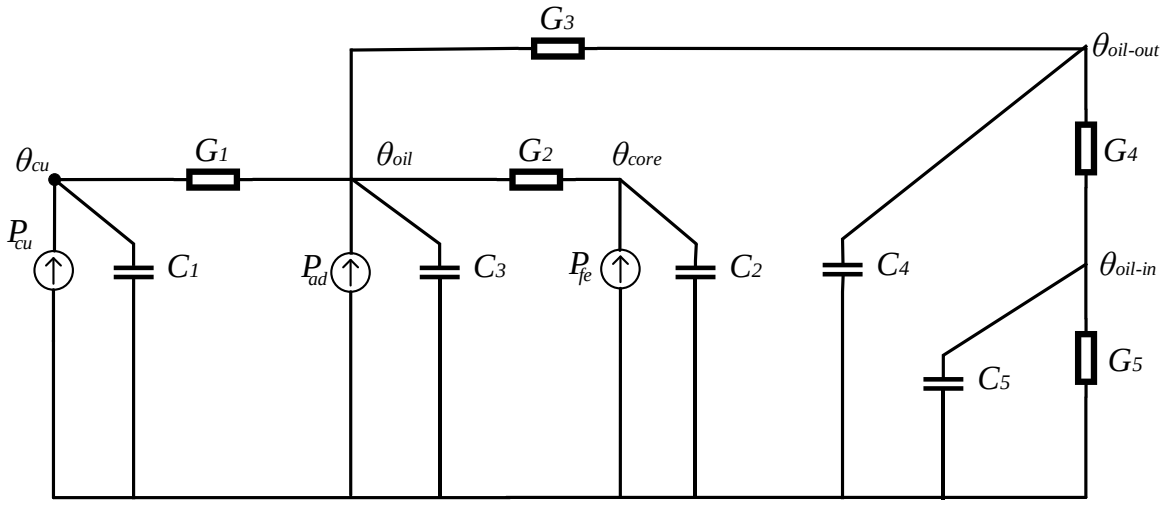

Figure 3-3. The proposed equivalent heat circuit of the transformer in [57].

$\theta_{cu}, \theta_{oil}, and\ \theta_{core}$	are the average temperature rise of winding, oil, and core, respectively
$\theta_{oil-out}, and\ \theta_{oil-in}$	are temperature rise at oil outlet (TOT) and inlet (BOT), respectively
$P_{cu}, P_{fe}, and\ P_{ad}$	are the copper, core, and stray losses, respectively

G_i are the thermal conductors

C_i are the thermal capacitors

Once the model is defined, determining the thermal parameters is challenging. The first approach for obtaining such parameters is performing experimental tests which is used in [46], [47], [55], [56], [58]. However, this needs expensive test facilities and is not practical for online transformers. In addition, the common parameters cannot be determined precisely enough because of the complexity of the phenomena and quantitative variations with the evaluation of time [57]. Therefore, researchers have tried to utilize alternative methods, such as optimization methods, neural networks, and fuzzy techniques, to estimate thermal parameters of equivalent circuits [59]–[62]. One of the first examples of using optimization methods is presented in [33]. In this work, a genetic algorithm (GA) is employed as a search method, based on a few on-site measurements, to estimate the equivalent circuit parameters. However, the equivalent circuit is constructed by five nodes, which means a relatively large number of thermal parameters need to be optimized. Therefore, a simplified model of [57] is presented in [50], which is made of 3 nodes and is shown in Figure 3-4. In the simplified model, all power losses including copper, iron, and stray losses are denoted by P_{all}. Also, all capacitances of core, windings, and part of the contained oil are combined into one lumped capacitor C_1.

Jauregui-Rivera et al. [63], [64] select the four top-oil models [46], [55], [65], [66] that require only parameters available from heat-run data to assess their acceptability. Then, some metrics are defined to quantitatively measure adequacy, consistency, and accuracy of the models and rank them based on their acceptability. The result shows that nonlinear top oil model of classical equation [46] is unacceptable while the linear top oil model [65] is acceptable just for oil-forced air forced (OFAF) cooling. On the other hand, Susa et al. [66] and swift et al. [55] models may be

acceptable for both OFAF and oil-natural air-forced (ONAF) cooling. Nevertheless, [64] argues that further investigation using larger data set is needed for the models of [55], [66].

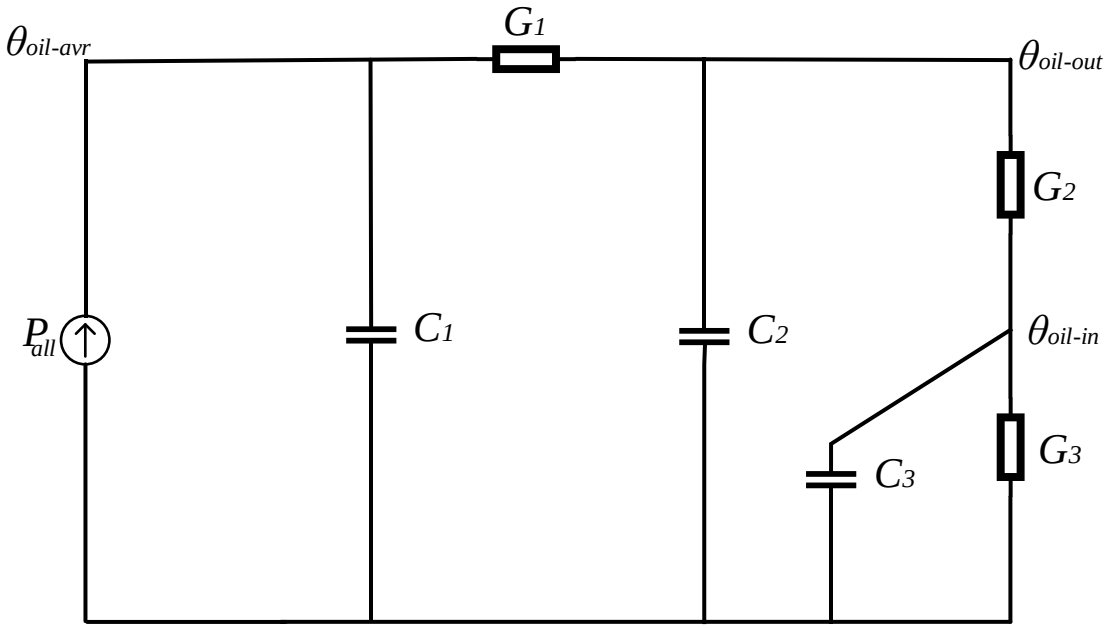

Figure 3-4. Simplified equivalent circuit of [57].

Susa et al. [66] developed the thermal model of swift et al. [55] by focusing specifically on the nonlinear thermal resistance of the transformer oil. In this model, the oil viscosity is considered as a parameter that varies with temperature. Therefore, the equivalent circuit is the same as [55]; however, the final form of the differential equation is as follows:

$$\frac{I_{pu}^2 R + 1}{R + 1}.[\Delta\theta_{oilR}]\mu_{pu}^n = \mu_{pu}^n \tau_{oilR}.\frac{d\theta_{oil}}{dt} + \frac{[\theta_{oil} - \theta_{amb}]^{1+n}}{{\Delta\theta_{oilR}}^n} \tag{3-12}$$

where μ_{pu} is the per unit value of oil velocity (μ) and calculated by:

$$\mu_{pu}^n = \frac{\mu}{\mu_{rated}} = \frac{1.3573 \times 10^{-6}.e^{[2797.3/(\theta_{oil}+273)]}}{1.3573 \times 10^{-6}.e^{[2797.3/(\Delta\theta_{oilR}+273)]}} = e^{[2797.3/(\theta_{oil}+273) - 2797.3/(\Delta\theta_{oilR}+273)]} \tag{3-13}$$

After discretizing with backward Euler (3-12) becomes to:

$$D\theta_{oil} = \frac{Dt}{\tau_{oilR}} . \left[\left[\frac{I_{pu}^2 R + 1}{R + 1} \right] . \Delta\theta_{oilR} - \frac{[\theta_{oil} - \theta_{amb}]^{\frac{1}{n}}}{(\mu_{pu} . \Delta\theta_{oilR})^{(\frac{1-n}{n})}} \right] \quad (3\text{-}14)$$

In addition to adding the oil velocity to the thermal parameters, Susa et al. [66] consider different values of n compared with [55], [56]. Table 3-3 determines the proposed values of n based on the initial oil circulation and type of cooling.

Table 3-3. Proposed values of constant n for the top-oil thermal model [66].

Oil circulation	n	
	ONAF/OFAF	ONAN
Initial oil circulation speed=0 (cold start)	0.5	0
Initial oil circulation speed >0	0.25	

Although the thermal top oil temperature models of Susa et al. [66] and Swift et al. [55] are the same, the no-load loss is not taken into account for the hot spot temperature thermal model of [66]. Figure 3-5 shows the proposed equivalent circuit of [66] for calculating the HST of the transformer based on the top oil temperature in which q_{cu} is the heat generated by load losses, $R_{th-hs-oil}$ is nonlinear winding to oil thermal resistance, and C_{th-wdg} is winding thermal capacitance.

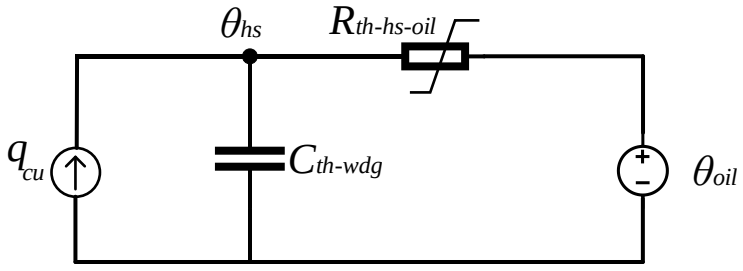

Figure 3-5. The hot spot temperature thermal model of Susa et al. [66].

Similar to the theory given for the top oil temperature model, the final equation of the hot spot temperature model is:

$$[K^2.P_{cu,pu}(\theta_{hs})].\mu_{pu}^{n}.\Delta\theta_{hsR} = \mu_{pu}^{n}.\tau_{wdg,R}.\frac{d\theta_{hs}}{dt} + \frac{(\theta_{hs}-\theta_{oil})^{n+1}}{\Delta\theta_{hs,rated}^{n}} \quad (3\text{-}15)$$

where the $P_{cu,pu}(\theta_{hs})$ is the load loss dependent on temperature and obtained by:

$$P_{cu,pu}(\theta_{hs}) = P_{cu,dc,pu}.\frac{235+\theta_{hs}}{235+\theta_{hs,R}} + P_{cu,eddy,pu}.\frac{235+\theta_{hsR}}{235+\theta_{hs}} \quad (3\text{-}16)$$

In (3-16), $P_{cu,dc,pu}$ and $P_{cu,eddy,pu}$ describe the dc and eddy losses variation with temperature.

Susa et al. [67], [68] improved their previous model [66] so as to present more accurate temperature calculation methods. In this model, the oil viscosity changes and loss variation with temperature are taken into account. In addition, the impacts of oil velocity changes on transformer time constants are considered. The equivalent thermal capacitances of the transformer oil for the different transformer designs and winding-oil circulations are also estimated by suggested equations, which is shown in Figure 3-6.

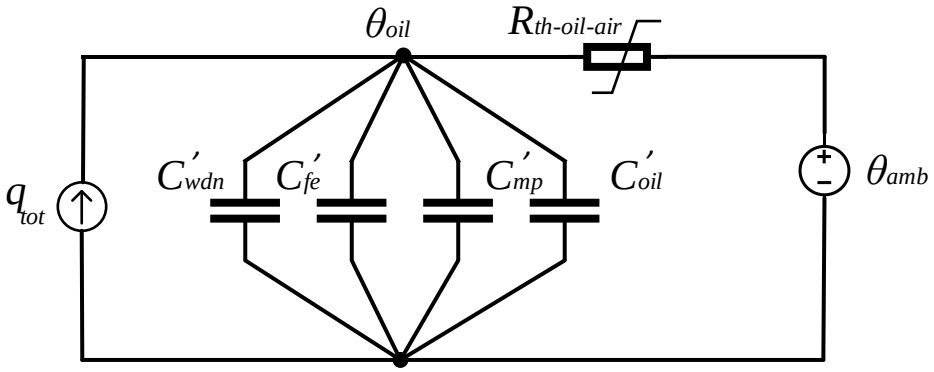

Figure 3-6. Thermal capacitance circuit proposed by Susa et al. [67].

In the thermal capacitance circuit, q_{tot} is the load losses in the transformer composed of the winding dc, eddy losses, and stray losses in the metal parts. Hence,

$$q_{tot} = q_{fe} + q_{wdn} + q_{st} \quad (3\text{-}17)$$

Also, the thermal capacitances for the different branches can be denoted as follow:

$$C'_{wdn} = Y_{wdn} C_{wdn} \quad (3\text{-}18)$$

$$C'_{fe} = Y_{fe} C_{fe} \quad (3\text{-}19)$$

$$C'_{mp} = Y_{st} C_{mp} \quad (3\text{-}20)$$

where C_{wdn}, C_{fe}, and C_{mp} are thermal capacitances of the copper, core, and transformer tank, respectively. Also, Y_{fe}, Y_{wdn}, and Y_{st} are the portions of the core, winding, and stray losses in the total transformer losses, respectively, and can be obtained as follows:

$$Y_{fe} = \frac{q_{fe}}{q_{tot}} \quad (3\text{-}21)$$

$$Y_{wdn} = \frac{q_{wdn}}{q_{tot}} \quad (3\text{-}22)$$

$$Y_{st} = \frac{q_{st}}{q_{tot}} \quad (3\text{-}23)$$

3.3.2 Thermal- Hydraulic Network Model (THN)

In brief, network modeling reduces the complex pattern of the oil flow inside a transformer winding down to a matrix of simple hydraulic channel approximations interconnected by junction points or nodes [69]. Figure 3-7, for example, shows the geometry approximated for a 2D network model of windings of a transformer and its corresponded THN model [45].

The detailed THN model of windings comprises two hydraulic network and thermal network models. The hydraulic part involves a network of ducts and junctions describing the oil flow distribution. In this modeling, the oil flow and pressure drop correspond to the electrical current

and voltage, respectively. The thermal model considering all types of heat transfer mechanisms is coupled with the hydraulic models to evaluate the thermal performance of winding and obtain the HST of the transformer [45].

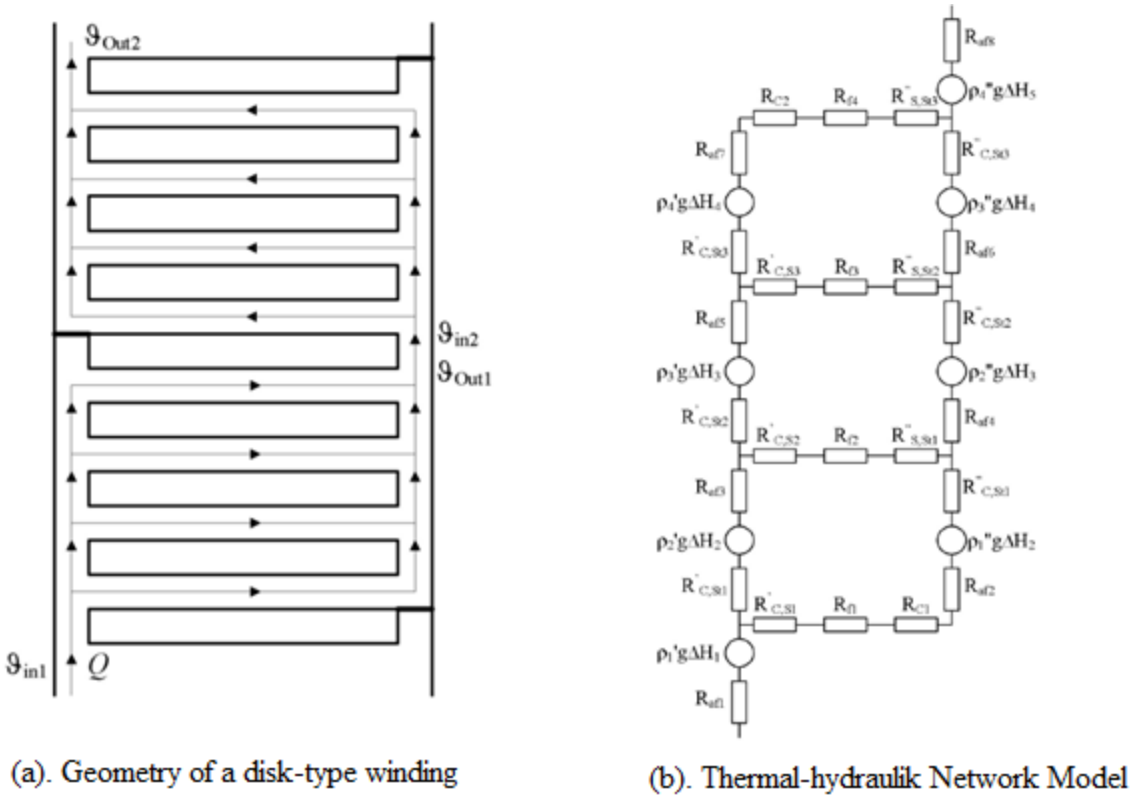

Figure 3-7. 2D geometry of a disc-type transformer winding related THNM [45]

Several physical assumptions are made to find a practical set of equations to describe the THN model. Firstly, the oil is considered a laminar flow between a pair of an infinite parallel flat plate since the Reynolds number is low [69], [70]. The second assumption is that the oil temperature rises linearly. Also, it is assumed that oil flow is completely mixed at nodes hydraulically and thermally [71]. Considering the mentioned assumptions, the set of equations for the THN models are obtained from the following [71]:

(i)- Conservation of mass applied to each node

(ii)- Conservation of thermal energy applied to each node

(iii)- Pressure-drop equation applied to each path

(iv)- Heat-Transfer equation applied to each path

Various studies have been performed to evaluate THN models' performance in estimating transformer HST. Rahimpour et al. [72] use 11 thermocouples in the ON-cooled transformer disc-type winding and measure the temperature of different discs. In spite of the excellent accuracy of THN model results for the overall temperature distribution, the complexity of oil dynamics modeling causes some discrepancies locally [73]. Also, the result of [74], [75] demonstrated that the original THN model equations might not be accurate enough, especially for describing the oil flow velocity. Therefore, the authors proposed new equations based on CFD simulation data for the Nusselt number and friction coefficient.

In fact, although the thermal models based analytical methods can offer acceptable accuracy in some cases, in most practical engineering applications, various assumptions and simplifications need to be made to enable the analytical solution of the differential equations representing the physical solution. This limits the applicability of these methods to simple type problems or limits the validity of the solutions if too many assumptions and simplifications are made [76]. However, the advent of digital computers has offered a solution to solve differential equations by numerical methods, which can deal with these drawbacks. For several years significant effort has been devoted to describing the thermal behavior of solid/fluid substances based on numerical methods, resulting in computational fluid dynamics (CFD) modeling.

3.4 Computational Fluid Dynamic (CFD) Modeling

Computational fluid dynamics (CFD) is a theoretical method of scientific and engineering investigation used for a unified cause and effect-based analysis of a fluid dynamics, heat, and mass transfer problem [77]. In CFD, the governing partial differential equations are mathematically operated to derive a system of linear algebraic equations (LAEs) called as discretization method, such as Finite Element Method (FEM), Finite Volume Method (FVM), and Finite Difference Method (FDM). The system of LAEs resulting from the algebraic formulation acts as the governing equations for CFD, and consist of the three flow-properties including velocity, pressure, and temperature as the unknown field variables [77]. The CFD governing partial equations, known as Navire-Stokes equations derived by applying the mass, momentum, and energy conservation laws to an elemental fluid/solid control volume.

3.4.1 Mass Conservation Law

The law of mass conservation is a general statement of kinematic nature, which expresses the empirical fact that in a fluid system, mass cannot disappear from the system nor be created [78]. If ρ is the fluid density, then the balance of mass ρU entering and leaving an infinitesimal control volume (Figure 3-8) is equal to the rate of change in density as expressed by the relation

$$\frac{\partial \rho}{\partial t} + \nabla.(\rho U) = 0 \tag{3-24}$$

where U is the velocity vector of fluid (m/s) and $\nabla.$ is known as the divergence operator and operates as follows:

$$\nabla. A = \frac{\partial A}{\partial x} + \frac{\partial A}{\partial y} + \frac{\partial A}{\partial z} \tag{3-25}$$

(3-24 is also called the continuity equation [79].

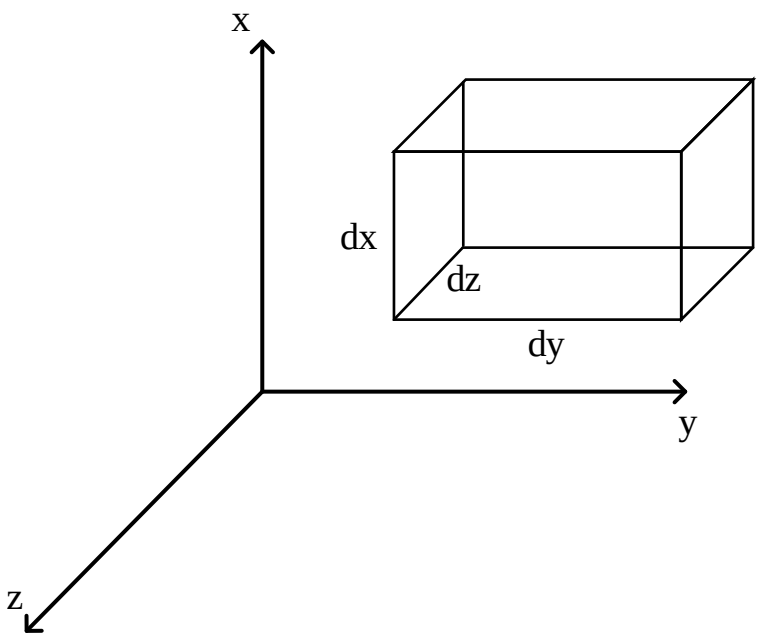

Figure 3-8. Coordinate direction and the infinitesimal control volume

3.4.2 Momentum Conservation Law

Momentum is a vector quantity defined as the product of mass and velocity. In order to determine all the terms of the conservation equations, it is necessary to define the sources for the momentum variation. According to Newton's law, the sources for variation of momentum in a physical system are the forces acting on it. These forces consist of external volume force and internal forces defined per unit mass, such as the pressure force, the viscous force, and the external body force[78]. Hence, the momentum conservation equation is:

$$\frac{\partial(\rho U)}{\partial t} + \nabla.(\rho U \times U) = -\nabla p + \mu(\nabla^2 U) + F \tag{3-26}$$

where p is the pressure, μ is the dynamic viscosity of the fluid, and F is external body force.

3.4.3 Energy Conservation Law

The first law of thermodynamics states that the sources for the variation of the total energy are

the work of forces acting on the system plus the heat transmitted to this system. Hence, with regard to the sources of energy variations in a fluid system and according to Fourier's law of heat conduction for transferring heat in a solid substance, the conservative form of the energy equation is

$$\frac{\partial(\rho c_p T)}{\partial t} + \nabla.\left(\rho c_p U T\right) = \nabla.(k\nabla T) + S_E \tag{3-27}$$

where c_p is specific heat capacity, T is temperature, k is thermal conductivity, and S_E is the heat source.

3.4.4 CFD Modeling Steps

CFD development follows a numerical methodology that consists of five main steps as follows [77]:

Step 1- Grid generation: A method to subdivide the complete domain into a certain fixed number of control volumes (CVs).

Step 2- Discretization method: A method is applied to the conservation laws at each internal grid point and boundary conditions at each boundary point to obtain one linear algebraic equation (LAE) from each grid point with unknowns as flow properties. Finite element, Finite volume, and finite difference methods are the most popular discretization methods.

Step 3- Solution methodology (Solver): It consists of the solution method, implementation details, and solution algorithm. The solution method is used for solving the system of linear algebraic equations (LAEs) based on explicit and implicit methods for unsteady state conditions and iterative methods for steady-state conditions.

Step 4- computation of engineering parameters: After step 3 and computing the flow properties,

the engineering parameters are obtained. The local value of parameters is computed at all the boundary grid points using numerical differentiation. Then, numerical integration uses the local boundary grid-point values to calculate the total value of an engineering parameter at a boundary.

Step 5- Testing: It is done by setting and running the model (code) for certain problems called benchmark problems, for which accurate numerical or experimental results are available in the published literature.

3.4.5 CFD Applications for Thermal Modeling of Transformers

In general, CFD modeling could be utilized to describe the thermal and fluid behavior of all components of the transformer. However, a large amount of transformer losses are related to the winding losses, and the winding hot spot temperature is a decisive factor in the aging of the transformer. Thus, many researchers have focused on detailed modeling of transformer windings [80]–[85]. Also, previous studies [80], [86]–[88] indicate that modeling the oil dynamics in a disc-type transformer winding is quite challenging due to the high flow sensitivity to several geometrical and operating parameters, such as duct size, number of discs, flow regime, etc. [73]. Hence, the CFD model has been applied almost solely to the windings, often as an extension to the THN model [45]. Hosseini et al. [89] studied the effect of different geometrical parameters on the cooling of the transformer winding using CFD. Also, it is shown that the inclusion of eddy current losses improves the prediction of the HST position while ignoring this loss could lead to inaccurate perdition of HST position and value. In [81], CFD modeling is used to evaluate the degradation rate based on the HST values for the transformer with vegetable oil. It is due to the fact that HST inside the windings of the transformer is one of the most crucial factors in the aging of the insulation system. An optimal mutual configuration of coils and cooling ducts for the effective cooling of a dry-type transformer is presented in [90] based on CFD and genetic

algorithm. The objective function value is computed using the CFD model, considering all heat transfer modes.

There have been several studies to investigate the accuracy of CFD modeling with experimental data for obtaining the HST of transformers [91]–[94]. For instance, Smolka et al. [95] present experimental validation of a numerical model of coupled physics involving heat, fluid flow, and electromagnetics within a three-phase dry-type electrical transformer. The comparison of numerical and experimental results shows that the prediction of the temperature distribution within the analyzed transformers and their surrounding was very accurate. In another attempt [91], a comparison between the 2D CFD simulations and experimental data is carried out, which shows a maximum of 3 ^{0}C difference in the temperature of winding discs. Lee et al. [92] utilize 2D CFD simulations of a zig-zag shaped winding in both OD (Oil- Direct) and ON transformers in order to acquire the pressure drop and heat transfer correlations as a function of non-dimensional numbers, such as friction factor, Reynolds number (*Re*), and Nusselt number (*Nu*). From the comparisons between numerical and experimental results, it is concluded that the correlations can predict the temperature rise of the zig-zag winding and oil, and pressure drop properly within about 10% error bounds. In an interesting study by Torriano et al. [73], an experimental setup comprises a closed cooling loop including all the main components of a power transformer equipped with thermal and fluid sensors to measure the HST and oil velocity. Moreover, 3D conjugate heat transfer simulations are performed using a CFD solver considering two different scenarios; simulation of the whole cooling system and simulation of the winding region only. The results show that the accuracy of CFD modeling is significantly improved by considering only the winding region instead of modeling the whole cooling system.

CFD simulation of a transformer is not restricted to only windings. In [96], an analytical,

numerical, and experimental investigation is conducted on the cooling performance of radiators in oil-filled power transformers. The CFD simulation is utilized on radiators to validate the predicted temperature distribution by the analytical study. Paramane et al. [97], [98] investigate the thermal performance of radiators under the effect of two blowing directions of both horizontal and vertical fan configuration in power transformers. The CFD simulation results show that, although the vertical blowing configuration is expected to have the highest efficiency theoretically, horizontal blowing is more efficient.

3.4.6 Conclusion

Accuracy and cost are two crucial factors in engineering modeling, and the optimum balance of these factors plays a decisive role in the process of modeling. The analytical methods, such as correlations and THN models, suffer from inaccuracy, especially regarding fluid flow issues. However, these methods are fast and easy to use. On the other hand, the CFD method provides a detailed resolution of thermal performance of all parts of the transformer with highly accurate estimation but with high calculation time. In addition to the long simulation runtime, CFD requires elaborate design data and specialist knowledge to be applied. Since the application of CFD on a transformer or even the windings is highly time-consuming, and THN models may show a good balance between performance and accuracy, an important role of CFD can be the improvement of the correlations and THN models by deriving more accurate coefficient formulations which depend on simplified geometries and assumptions about the temperature and flow distributions [45], [99]. For example, authors in [74], [75] used the CFD simulation to obtain the required data sets to process and then present more accurate heat transfer equations for transformer cooling oil flow in a THN model. Furthermore, CFD can be utilized in the design stage of various components of transformers, fan-cooled radiators, or bushings, for instance.

Bushing failure is identified as one of the major causes of transformer breakdown in different reported studies [100]. In fact, the bushing appears to be a fragile part of a transformer in a way that more than 20% of transformer failure is related to the bushing failure [101]. Although these outages are due to several factors, the most significant one with 32% is overheating and hot spot temperature issues of bushing [100]. However, the impact of the bushing on the thermal performance of power transformers has been neglected in previous studies. This issue is more critical, especially for the overload capability of transformers, because the planned load will carry through bushings. Nevertheless, the overload capability of bushings is not involved in all existing dynamic thermal modeling of transformers. On the other hand, the HST estimation of bushings has been scarcely investigated from the theoretical point of view.

On the other hand, the absolute majority of the existing transformer thermal models are valid for balanced loading conditions, whereas there are many abnormal or unbalanced situations that cannot be accurately represented by these models. One of such unusual phenomenon is the Geomagnetically Induced current (GIC). During a geomagnetic disturbance, a slowly varying current, which is referred to as the geomagnetically induced current (GIC), is injected into the grounded neutral transformers [102], [103]. This DC current results in the half-cycle saturation of the transformer core, which induces additional power loss into different parts of the transformer, such as metallic structural parts. The consequence is additional heating at these locations, at best, some of the useful life of the cellulosic insulation is lost, and, at worst, the unit is at a higher risk of incurring an imminent failure due to the gassing, causing transformer failure [104]–[107].

Furthermore, the transformer power losses and magnetic flux distribution in the transformer are different during balanced and unbalanced loading conditions. In fact, during the unbalanced loading, the stray flux cannot be neglected due to increases in leakage flux [108]. Stray losses may

result in a temperature rise in the transformer tank. Since the temperature rise in the tank walls depends on both the stray losses and the oil flow condition around them, the analytical methods might not be precise enough to estimate it. Hence, CFD modeling would be beneficial for predicting the local oil flow, which is quite complicated [45]. To the best knowledge of the author, there has not been any investigation of the temperature rise of the tank due to the stray losses based on CFD modeling. Hence, the existing models would not be accurate to be applied in unbalanced loading conditions.

Chapter 4

FEM Modeling of Transformers

4.1 Introduction

A significant number of coupled multi-physics simulations are necessary for the study, design, fabrication, and operation of electrical devices. The study of loss, heating and cooling, electromagnetic force, vibration, and noise, etc., is based on the analysis of electromagnetic fields in engineering. For electrical devices, these performance characteristics have a direct impact on their ability to operate reliably, safely, cost-effectively, and ecologically. Large-scale electromagnetic and thermal fields are challenging to properly assess for a variety of reasons, including but not limited to the following problems [109]:

1- The complicated mathematical formulation and numerical implementation of linked multi-physics issues,
2- Challenging modeling and simulation of very large electromagnetic devices due to the existence of multiscale and complex geometries,

3- Shallow depth of field penetration (e.g., less than 1 mm),
4- Variation of material characteristics by an external condition such as excitation or external stress.

Despite advances in numerical approach, software applications, and technology over the last several years, it is not feasible to create a comprehensive model of transformers. As a consequence, the modeling is simplified, and occasionally numerical techniques must be supplemented with analytical approaches in the postprocessing phase in order to achieve the expected results.

4.2 Governing equations

4.2.1 Low-frequency Electromagnetic Equations

In order to investigate the hot spot heating of a transformer during a GMD event, it is necessary first to obtain the heat source, which is the power loss. No-load and load losses are the two types of transformer losses. The no-load losses are due to magnetization current in the core; Thus, it is known as core loss. Load losses are divided into two categories: I^2R losses caused by Joule heating in the coils and stray losses caused by stray flux colliding with metal objects such as tank walls, clamps, other structural parts, and coils. Because coil conductors are frequently stranded and transposed, the I^2R losses are typically dictated by the DC resistance of the windings. The stray losses are determined by the conductivity, permeability, and form of metal objects. Induced eddy currents in these items are the primary cause of these losses [6].

Transformers are constructed to work in the linear zone of their magnetizing characteristic and survive the hot spot heating caused by losses in this region. However, when GIC flows into a transformer winding, the operating point moves, which, depending on the level of GIC current and

the core configuration of the transformer, can cause half-cycle saturation of the core [110], [111]. Consequently, a greater amount of flux escapes beyond the core, generating more eddy currents in various core and winding assembly components, such as the tie plate, clamps, and tank walls. The upshot is increased heat loss, temperature rise, and the production of hot patches.

The governing partial differential equations for describing the low-frequency electromagnetic behavior of transformers are Maxwell's equations consist of the following three basic equations:

$$\nabla \times E = -\frac{\partial B}{\partial t} \tag{4-1}$$

$$\nabla \times H = \frac{\partial D}{\partial t} + J \tag{4-2}$$

$$\nabla . B = 0 \tag{4-3}$$

where H is the magnetic field intensity (A/m), E is the electric field (V/m), B is the magnetic flux density (T), and D is the electric flux density (C/m^2). Also, Ohm's Law describes the link between E and J as:

$$\mathrm{J} = \sigma E \tag{4-4}$$

where σ is the electrical conductivity (S/m). In low and mid-frequency and when wave effects can be neglected, by applying Ohm's Law to Maxwell Equations, the governing equation is simplified as:

$$\nabla \times \frac{1}{\sigma} \nabla \times H = -\frac{\partial B}{\partial t} \tag{4-5}$$

$$\nabla . B = 0 \tag{4-6}$$

In the above-mentioned equations, the displacement current term, which is only significant at very high frequencies, has been disregarded. By solving these equations, the linkage and leakage fluxes in all transformer parts can be obtained. The stray losses can be obtained based on the

leakage flux and eddy currents generated on each part. In addition, the eddy losses in the winding should be added to the winding load losses. These losses will vary in various regions of the winding. To calculate the overall eddy current loss, a winding's average loss density is multiplied by the winding's entire mass or volume. However, in order to determine local winding temperatures and, in particular, the temperature of the hot spot, we must know how these losses are distributed throughout the winding [110]. Because of that, in this thesis, instead of considering an integrated cylinder, the critical disks of the windings are modeled. In that case, the leakage flux injected into those disks is determined, and the non-uniform loss distribution of winding can be imported to the CFD model for finding the location as well as the value of winding HST. This modeling is crucial, especially in the presence of GICs with half-cycle core saturation.

4.2.2 Thermal and Fluid Equations

Computational Fluid Dynamics (CFD) can describe the thermal behavior of an event considering the fluid flow and pressure as well as temperature distribution. This computational approach is based on the solution of the Navier–Stokes equations, which assert the conservation of mass, momentum, and energy for fluid flow. For an incompressible fluid (such as oil), these equations may be formulated as following [73]:

Continuity equation:

$$\frac{\partial \rho}{\partial t} + \nabla.(\rho U) = 0 \tag{4-7}$$

where ρ is the local fluid density, and U is the velocity vector.

Momentum equation:

$$\frac{\partial(\rho U)}{\partial t} + \nabla.(\rho U \times U) = -\nabla p + \mu(\nabla^2 U) + g(\rho - \rho_\infty) \tag{4-8}$$

where p is the pressure, μ is the dynamic viscosity of the fluid, and F is the buoyancy force. In ((4-8), the terms on the right-hand side of the equation are the pressure force, the viscous force, and the buoyancy force, respectively. The last term refers to the force that is responsible for driving the flow during the natural convection mode. This force is associated with the density gradients that exist within the fluid.

And, the last equation of Navier–Stokes equations is the Energy equation:

$$\frac{\partial(\rho c_p T)}{\partial t} + \nabla.(\rho c_P U T) = \nabla.(k \nabla T) + S_E \tag{4-9}$$

where $c_p$is specific heat capacity, k is thermal conductivity, and $S_E$is the heat source. Also, to determine the temperatures of the solid domain, ((4-9) is simplified to the following equation, known as the conduction equation.

$$\frac{\partial(\rho c_p T)}{\partial t} + \nabla.(\rho c_P U T) = \nabla.(k \nabla T) + S_E \tag{4-10}$$

4.3 FEM Modeling

Depending on the nature of the problem, magnetic and thermal solutions for big power transformers may be modeled in either a three-dimensional (3D) or two-dimensional (2D) space. Since it is not feasible to model all parts with fully detailed geometry, each component of the models may be constructed with a significant amount of geometric detail. For the magnetic model, the active parts, including the transformer core and windings, and structural parts, such as clamping plates, tie plates, and the tank are paramount. Since heat moves from one place to another by conduction, the thermal model has fewer parts than the magnetic model. The surrounding air and oil are not included in the thermal model, but the transmission of heat via convection or radiation to the surrounding environment is represented by providing the coefficients of heat transfer for

convection and radiation on the surfaces of the items. Further explanation about the magnetic and thermal modeling of the electromagnetic devices can be found in [109].

4.3.1 Geometry and Material Specifications

The geometry of the transformer is clearly explained in section 1.2. The core is comprised of very thin laminations of electrical steels that overlap in the joint zones. Due to a large number of needed elements, solving a finite element problem for such geometry is impractical in reality.

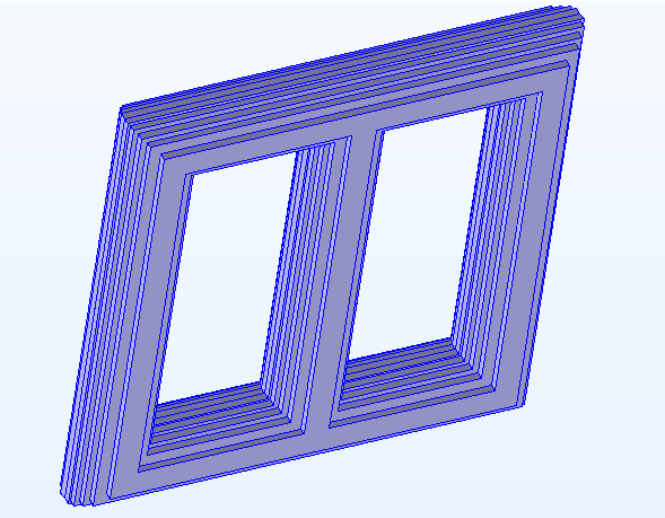

Figure 4-1. 3D core modeling of transformer with laminations

Therefore, simplification strategies are required for such research. At the frequency range of this research, it should be emphasized that the skin depth of the core material is much more than the thickness of the lamination. This indicates that the influence of eddy currents on the overall flux density distributions can be disregarded. In addition to the leg and yoke dimensions, the cross-section of the transformer's core plays an important role in the electromagnetic analysis. As illustrated in Figure 4-1, it is crucial to design the geometry with precise cross-sectional when considering lamination.

Magnetic phenomena are characterized by magnetic flux density B and magnetic field H where

H denotes the movement of charges, whereas *B* represents the force applied to charges. Both amounts adhere to the law of cause and effect. The modeling of the relationship between these two parameters is another difficult aspect of electromagnetic modeling. When the transformer is operating normally, we may assume that this relationship is linear and could be expressed as

$$B = \mu_0 \mu_r H \tag{4-11}$$

where μ_0 is the free space permeability of $4\pi \times 10^{-7}$ (H/m), and μ_r is the relative permeability and varies based on the material. However, this simplification cannot be implemented if the value of *B* goes behind the saturation level. In our studies, since the GIC causes the half-saturation in the transformer core, ((4-11) is no longer valid. Consequently, it is important to describe the nonlinear relationship between *B* and *H* using the *B*-*H* curve similar to Figure 4-2. It should be noted that this curve changes depending on the material used in the core; hence it is essential to know the specific composition of the core. In addition, the electrical conductivity of the core material is set

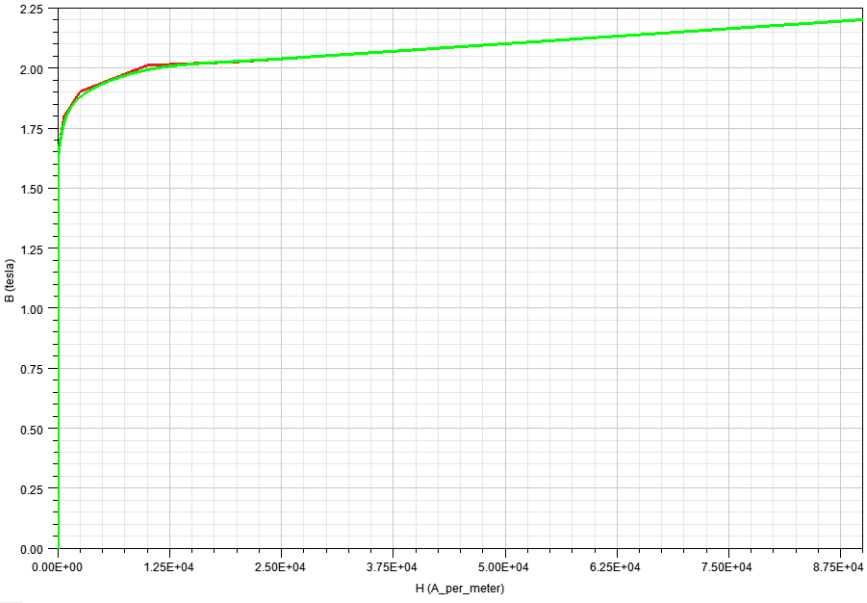

Figure 4-2. B-H curve for the core

to zero since the eddy current effects are disregarded.

Windings are the other active parts of the transformer consisting of copper conductors with multi-turns, paper insulation, and oil ducts for cooling the winding. The winding of the case study transformer is disc-type and shown in Figure 4-3, including the conductor strands, paper, and oil

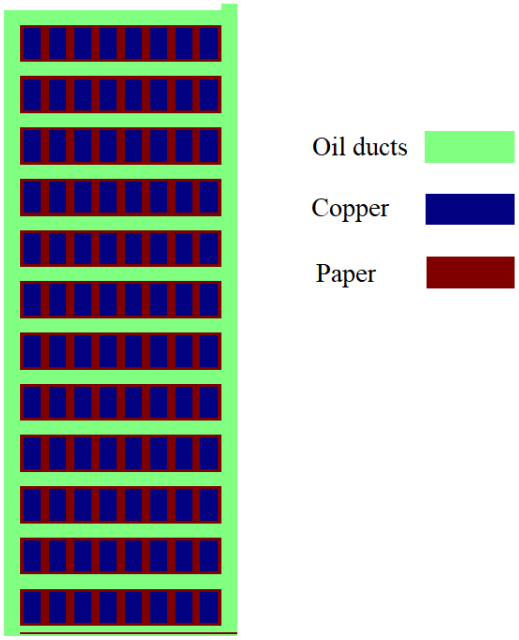

Figure 4-3. 2D geometry of winding for thermal modeling

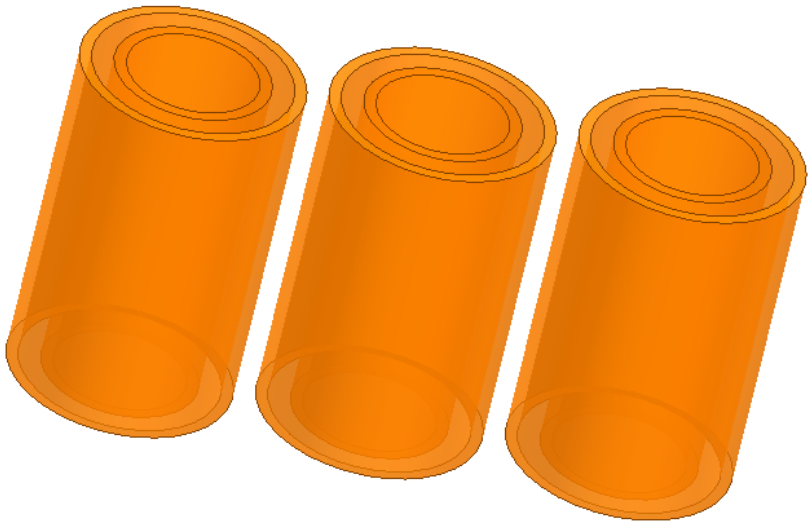

Figure 4-4. 3D geometry of winding for magnetic modeling

during the zero sequence studies. Therefore, a nonlinear relation between B and H is considered channels. Although all these details are essential for the thermal analysis of winding by CFD, in electromagnetic studies, the winding can be modeled as a simple cylinder with a cross-sectional area, as shown in Figure 4-4. Since copper is a non-magnetic material, the relative permeability of the windings is considered to be 1.

The geometry of a tank is regarded to be a thin, rectangular, empty box. The additional structural components, including the core clamps, tie plates, and tank shunts, may all be represented in a cube-based reduced geometry model. In most models, it is assumed that the material of the tank has a constant relative permeability between 500 and 1000 and no electrical conductivity. However, this assumption is not valid in this research due to the tank saturation for the mild-steel material [39], comprising the tank and clamping plates, shown in Figure 4-5. Notably, including

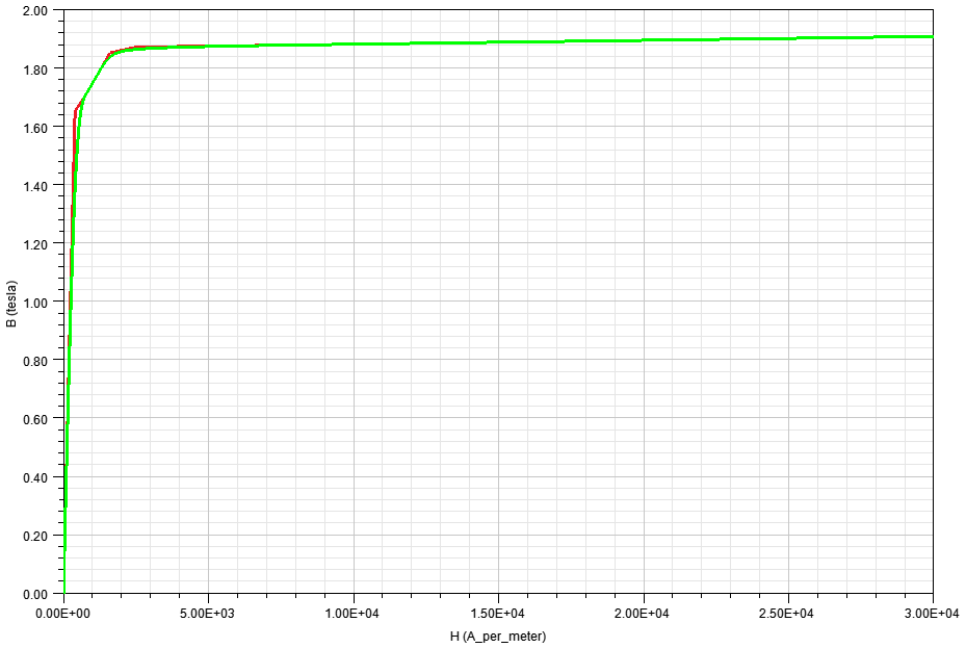

Figure 4-5. B-H curve for the tank and structural parts

eddy currents inside the tank and clamping plates necessitates a substantial increase in the number

of elements, which might result in a very large computational burden [24].

4.3.2 Excitation and Electromagnetic Boundary Conditions

The excitation of the model is by the determination of the winding currents. Usually, by applying the voltage and resistance of the winding or coupling the FEM model to the circuit model inside the commercial software, the model is launched. In this case, the winding current is unknown, and the software calculates it. The second way is to excite the winding directly by inserting the known winding current. Calculating the current injected into the winding during the GIC needs an elaborate low-frequency transformer model, and implementing such a model in FEM commercial software is extremely challenging. Thus, as explained in Chapter 2, the current is obtained by EMTP-RV according to the low-frequency transformer model presented in [32], [35]. Next, the obtained current is injected into the cross-sectional area of the winding. By using this technique, there is no need for soft-energization of the transformer.

4.3.3 Transformer losses

Transformer losses may be categorized generally as no-load and load losses. When the transformer is powered with its rated voltage at one set of terminals, but the other sets of terminals are open-circuited such that no load or through current flows, no-load losses occur. In this instance, total flux is present in the core, but just the required excitation current travels through the windings. Due to hysteresis and eddy currents caused by the time-varying flux in the core steel, the losses are mostly core losses. Load losses occur when the output is linked to a load such that current flows from the input to the output terminals of the transformer. Typically, load losses can be broken down into two categories: I^2R losses, which are caused by Joule heating produced by current flow in the coils, and stray losses, which are caused by the stray flux as it comes into contact with metal objects like tank walls, clamps, or bracing structures, as well as the coils themselves [11]. As

different techniques and models are required to calculate these losses, we describe each one separately.

4.3.4 Core Losses

Calculating core losses is one of the most difficult aspects of transformer design. The first reason is the complex interaction between core losses and the flux density waveform, and the second is to determine the spatial distribution of flux density over time. The relationship between flux density waveform and resulting losses is determined by the material properties of the core. The flux density distribution is nonetheless determined by the applied voltage, core design, and material parameters. Due to the three-dimensional core shape and nonlinear behavior of the core materials, this job requires a complicated numerical technique [24]. As we will be calculating the HST of transformer structural components and winding in this study, the core loss is not modeled.

4.3.5 Winding Losses

There are two types of losses in transformer windings. The first is the resistive loss due to the flow of the normal current into the winding conductors, and the second is the ohmic loss created by eddy currents. In a conductive medium, eddy currents are generated when time-varying fluxes are passed across the medium. The windings' eddy currents are created by leakage fluxes penetrating the windings. Leakage fluxes are produced directly by winding currents and have the same phase as the winding currents. On the other hand, the phases of the eddy currents and the derivatives of the leakage fluxes are identical to each another. Therefore, winding currents and induced eddy currents are aligned in a direction that is perpendicular to one another. With this knowledge, we are able to distinguish between the losses caused by the various processes. Therefore, winding losses are the total of ohmic losses owing to effective DC current (RMS value of currents), which are also known as DC losses, and ohmic losses due to induced eddy currents

[24].

The DC losses can be obtained using:

$$P_{DC} = I_{rms} R_{DC}^2 \tag{4-12}$$

where I_{rms} is the effective value of winding current and R_{DC} is the DC resistance of windings. It should be noted that to calculate the DC losses during GIC; first, we should obtain the effective current based on the exciting harmonics in the GIC current as,

$$I_{rms} = \sqrt{I_0^2 + \frac{(I_1^2 + .. + I_k^2)}{2}} \tag{4-13}$$

where I_i is ith harmonics of the injected current into the transformer windings during GIC.

However, the challenging part is obtaining the eddy current losses. As explained before, eddy currents are currents in a conductive domain that are caused by the time-varying electric field produced by the time-varying flux density. Consequently, there will be an ohmic loss in the region proportional to the square of the current density, known as eddy losses or stray losses. Figure 4-6 shows the stray fluxes that create stray losses in different parts of the transformer.

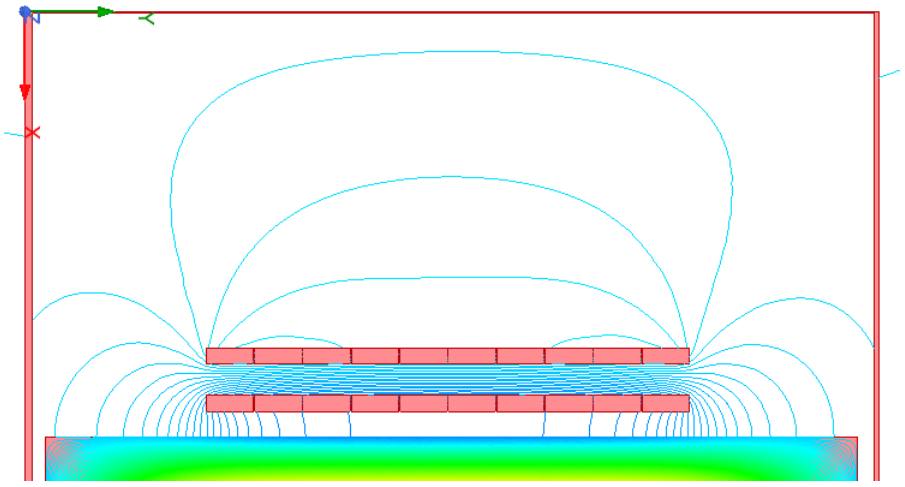

Figure 4-6. The stray flux paths into the tank and windings.

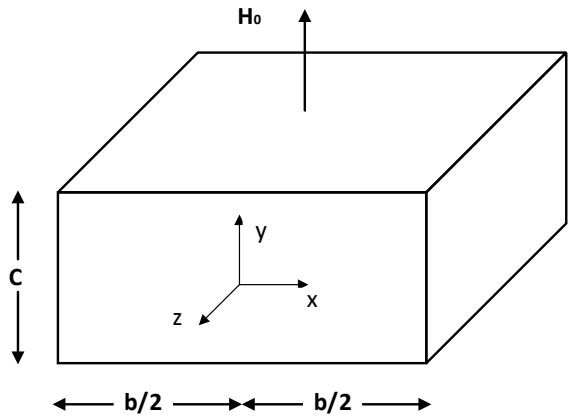

Figure 4-7. Geometry of a conducting strand in the winding for calculating the stray losses

To investigate how stray flux contributes to losses in the coils, we focus on a single strand with a rectangular cross-section, shown in Figure 4-7. In our idealized geometry, the strand has a length of zero in the z-axis. This indicates that no electromagnetic field depends on the z-axis. We also assume that the exterior and internal magnetic fields each only have a y component. With these assumptions, we can solve Maxwell's equations using the SI system and get:

$$\nabla \times E = -\frac{\partial B}{\partial t} \quad \overset{yields}{\Longrightarrow} \frac{\partial E_x}{\partial x} = \mu \frac{\partial H_y}{\partial t} \tag{4-14}$$

$$\nabla \times H = J \quad \overset{yields}{\Longrightarrow} \frac{\partial H_y}{\partial x} = J_z \tag{4-15}$$

$$\nabla . B = 0 \quad \overset{yields}{\Longrightarrow} \frac{\partial H_y}{\partial y} = 0 \tag{4-16}$$

where μ is the permeability, *E* is the electric field, and *H* is the magnetic field. Also, in the metallic conductor, ignoring the displacement current, the current density *J* can be calculated by Ohm's law as follow:

$$\mathrm{J} = \sigma E \quad \overset{yields}{\Longrightarrow} J_z = \sigma E_z \tag{4-17}$$

where σ is the electrical conductivity. Combining the last four equations together and considering the H_y with a sinusoidal time dependence of the form $H_y(x,t) = H_y(x)e^{jwt}$ We will have

$$\frac{\partial^2 H_y}{\partial x^2} = j\omega\mu\sigma H_y = k^2 H_y, \quad k^2 = j\omega\mu\sigma \tag{4-18}$$

By setting the boundary condition that $H_y = H_0$ at $x = b/2$, where b is the strand width perpendicular to the field direction and H_0 is the maximum amplitude of the external field, we may solve ((4-18) as

$$H_y(x) = H_0 \frac{\cosh(kx)}{\cosh(\frac{kb}{2})} \tag{4-19}$$

and based on ((4-15)

$$J_z = -kH_0 \frac{\sinh(kx)}{\cosh(\frac{kb}{2})} \tag{4-20}$$

Now, after finding the eddy current density, we can find the eddy current loss per unit length in the z-direction as

$$P_{ec} = \frac{c}{2\sigma}\int_{-b/2}^{b/2} |J_z|^2\, dx = \frac{cH_0^2|k|^2}{\sigma|\cosh(\frac{kb}{2})|^2}\int_0^{b/2} |sinh(kx)|^2 dx \tag{4-21}$$

where c is the strand dimension along the y direction. Using the expression for k, and performing the integration calculation, the eddy current loss per unit volume is obtained as [110]:

$$P_{ec} = \frac{H_o^2 q^4 b^2}{6\sigma} = \left(\frac{\pi^2}{6}\right) f^2\mu^2 b^2 \sigma H_o^2 = \left(\frac{\pi^2}{6}\right)\frac{f^2 b^2 B_o^2}{\rho} \tag{4-22}$$

where f is the frequency, ρ is the resistivity, and $B_o = \mu H_o$. A detailed calculation of this method with more explanation can be found in [110].

Based on this method, one may assert that determining the flux distribution in windings is equivalent to determining the stray losses in the winding. Although there are mathematical methods like Rabin's approach [24] for determining the flux pattern inside the windings, they are

not particularly precise. On the other hand, [8] indicates that the 2D FEM model can calculate the leakage flux inside the winding with high precision. In this work, a 2D FEM model is used to determine the leakage flux in the winding in order to calculate the stray loss.

4.3.6 Stray Loss in Structural Parts

In the previous section, it is discussed how eddy currents are induced in metallic structural elements by the time-varying induced leakage flux on their surface. As the structural parts are exposed to the leakage flux, the eddy currents will be generated in those parts, resulting in stray losses. Most of the stray loss in a transformer happens in its structural components, such as its clamps and the tank. These components are generally composed of magnetic steel and have a thin skin dept compared with the thickness of the material. This small skin dept requires a large number of finite elements to capture the eddy currents.

Since power transformers have a complex and non-symmetric shape that contains nonlinear materials, precise estimation of stray eddy current losses is a highly challenging electromagnetic problem. In addition, this is a time-dependent electromagnetic issue [24]. In normal conditions and without saturation, it is not an issue in 2D, but when modeling a large object such as a clamp or tank in 3D, the number of components and solution timeframes would be impractical. Consequently, a technique known as the impedance boundary approach has been created to overcome this issue [110]. This approach just needs finite components to cover the surface of the substance. These are unique components known as surface impedance elements. In order to determine these components, the relative permeability and conductivity of the material are considered. Then, after the execution of the 3D problem, the answer is processed to yield the loss in Watts according to ((4-23),

$$P_{eddy-st} = \sqrt{\frac{\omega \mu_0 \mu_r}{8\sigma}} \int_{Surface} H_t H_t^* \, dS \tag{4-23}$$

where H_t is the tangential component of the magnetic field vector at the surface in amps/m and H_t^* is the complex conjugate of H_t.

4.4 Simulation Results

4.4.1 Electromagnetic Analysis

In this section, the magnetic and thermal behavior of the transformer case study under normal loading is investigated. As mentioned before, the transformer case study is a 3-legs, 3-phases 125 MVA autotransformer with the rated voltages of 230/115 kV. The magnetic field inside the transformer has been computed using FEM software on a mesh that has been adjusted to achieve the highest degree of precision. In this model, the transformer windings are excited by their nominal values, and the *B-H* curve based on section 4.3.1 is considered for the core, clamps, shunts, and tank. In this simulation, the transient solver with the time step of 500 μs and the time stop of 100 *ms* is implemented. Figure 4-8 and Figure 4-9 exhibit the excitation currents of CV and SV windings, respectively. The RMS values of the currents are 294.5 A, and 302A based on the transformer rating. The magnitude and direction of core's linkage flux density are shown in Figure

Table 4-1. Transformer ratings

Rated Power [MVA]	125
Rated Voltage[kV]	230 Grd Y/115 Grd Y
Rated Current [A] HV/LV	302/596.4
Frequency [Hz]	60
Turn Ratio N_{SV}/N_{CV}	597/613

4-10 at 50 *ms*. At this time, the current of the right leg is crossing zero while in other legs are in the vicinity of positive and negative peaks. As a result, we have the maximum flux density 1.72 T with the opposite direction in the middle and left leg, while the flux density in the right leg is crossing zero. As we expected, the transformer is working in the linear domain of the core's B-H curve with the flux density of 1.72 T. Figure 4-11 demonstrates the linkage flux in the core with the leakage flux penetrated to the structural parts such as the tank, and tank shunts. As it can be seen, the magnitude of the leakage flux is very lower than the magnitude of the linkage flux in the core. Figure 4-11 also indicates that the leakage flux penetrates the tank shunts more than the tank

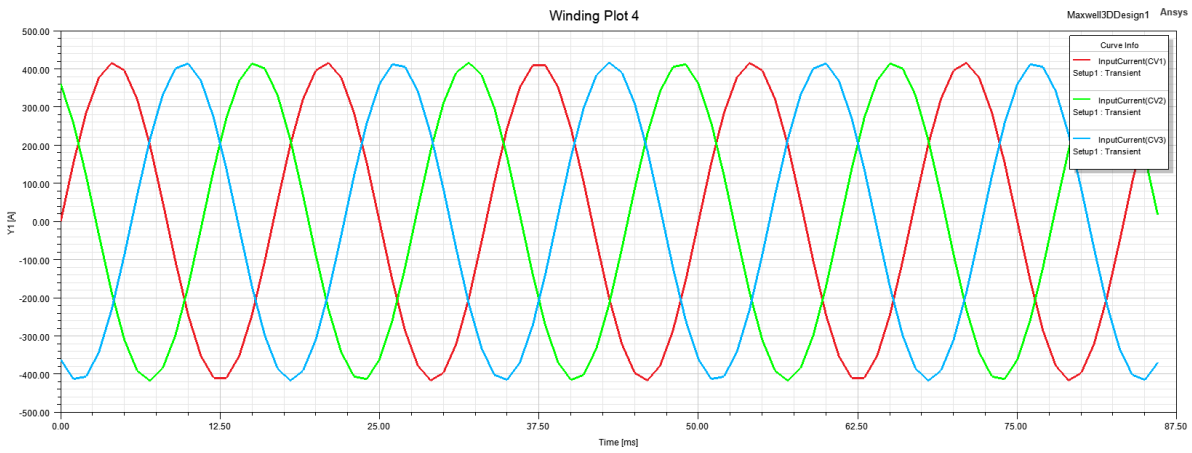

Figure 4-8. The three-phase CV winding excitation in normal loading with the rms value of 302 A

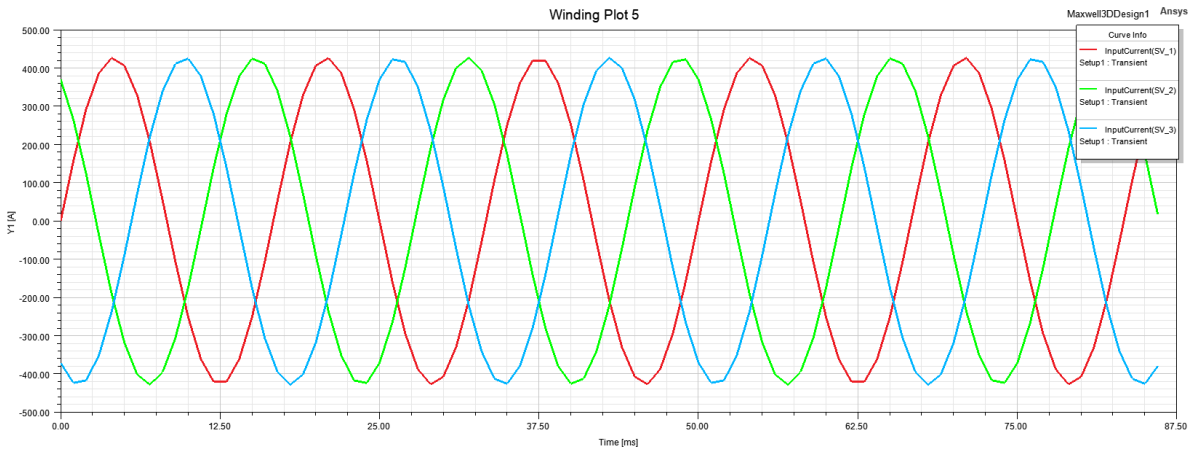

Figure 4-9. The three-phase SV winding excitation in normal loading with the rms value of 294.5 A

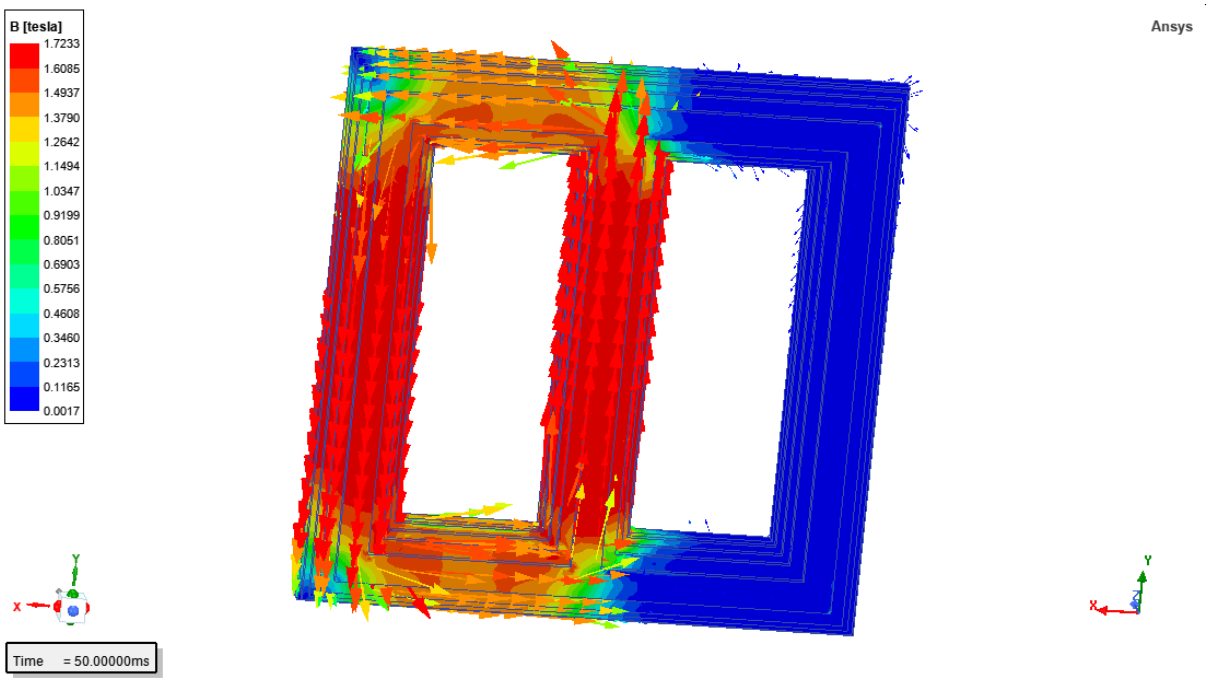

Figure 4-10. The linkage flux density (T) inside the transformer core at 50ms

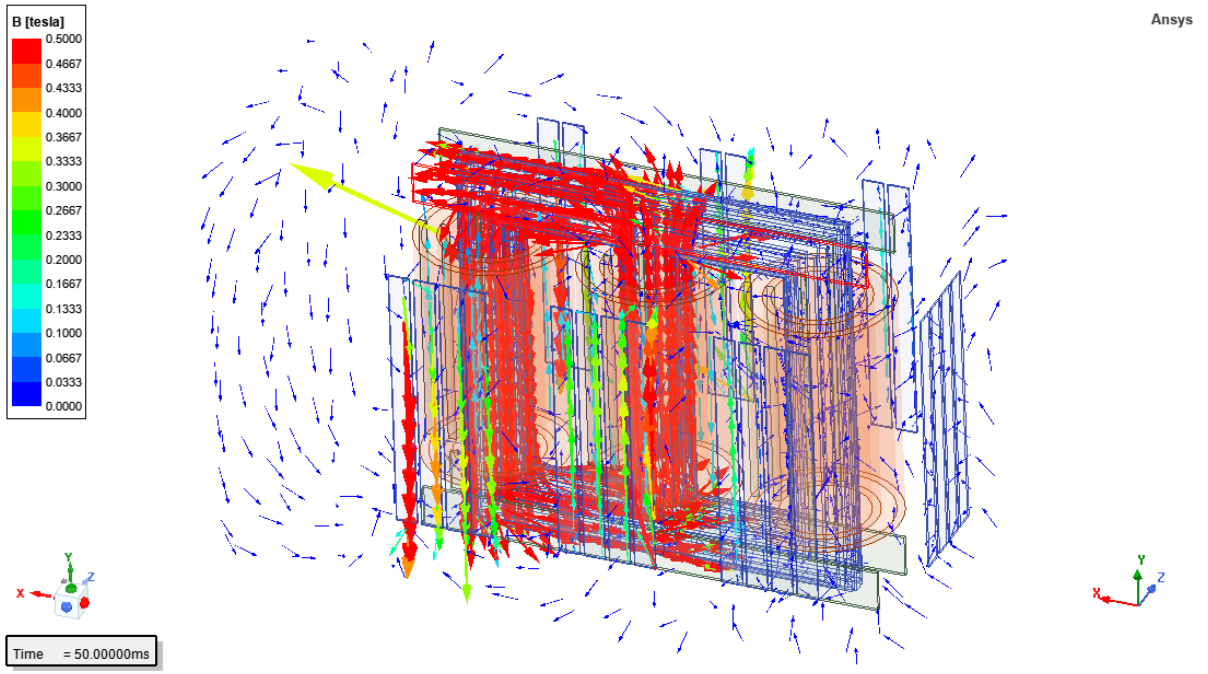

Figure 4-11. Leakage flux density penetrates inside other parts such as tank shunts and tank.

itself, which is precisely why tank shunts are used in transformers. Figure 4-12 and Figure 4-13 provide further information on the leakage flux density within the shunts and the tank, respectively.

As can be observed, the flux density in the tank shuns approaches 0.7 T, while it is less than 0.1 T in the majority of the tank and almost zero in the overlap domain. Since the tank shunts are

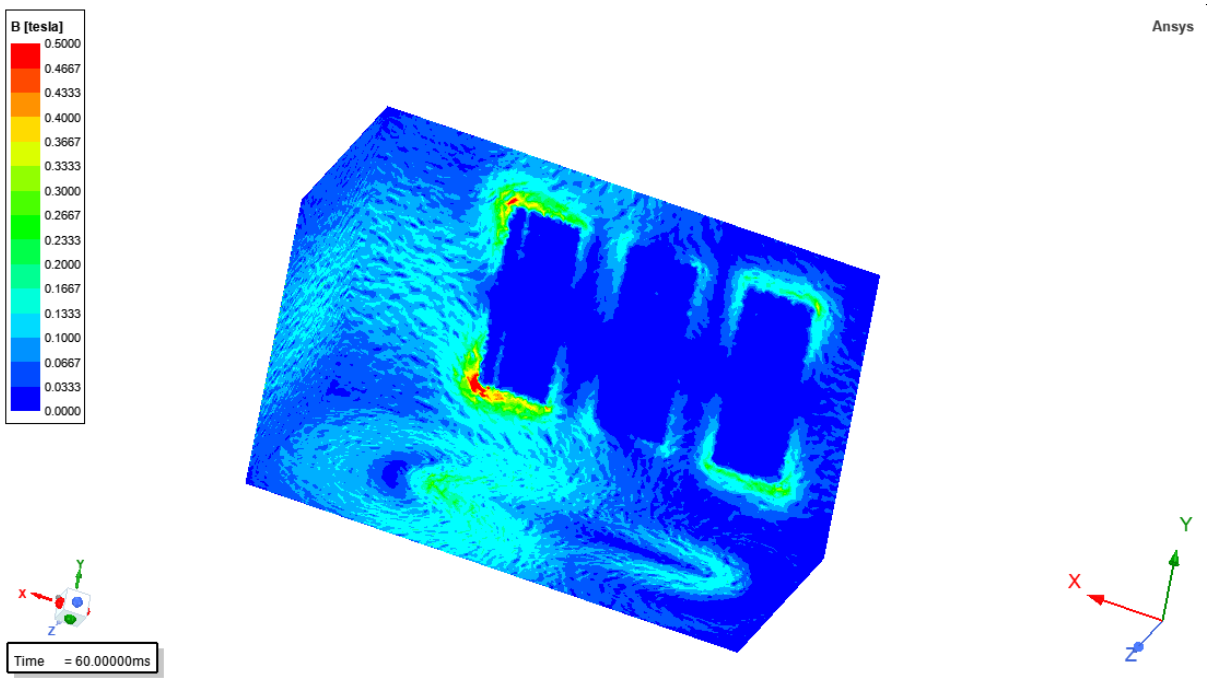

Figure 4-12. The leakage flux density inside the transformer tank

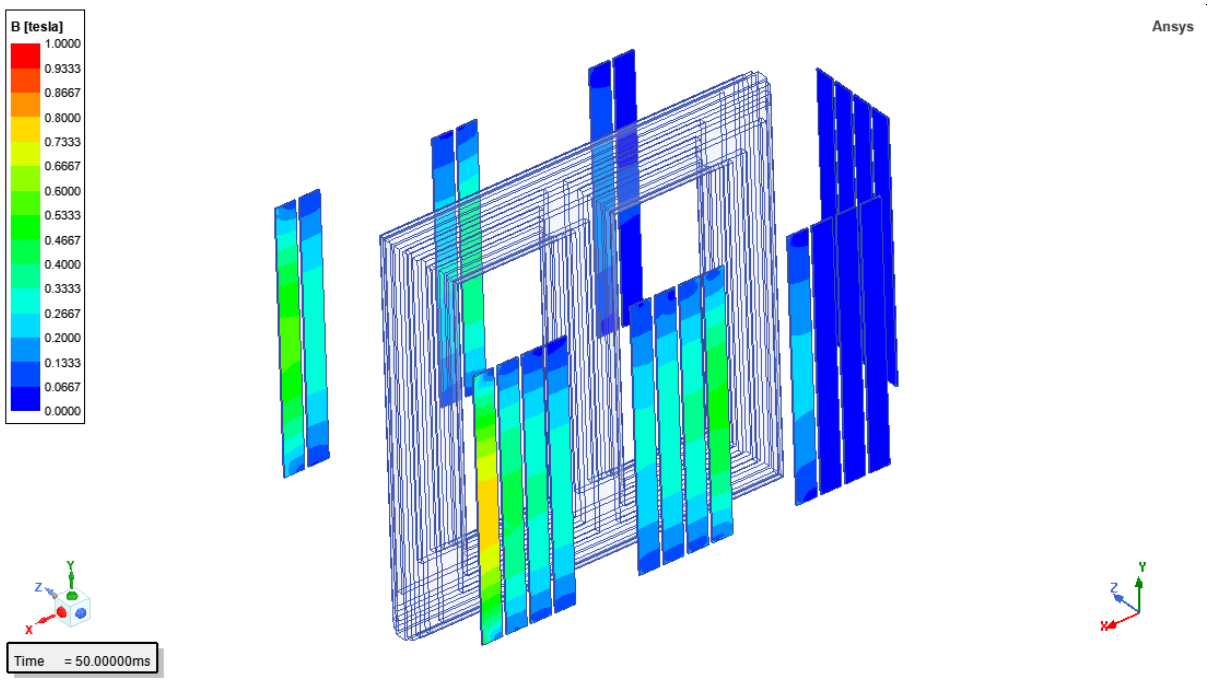

Figure 4-13. Leakage flux density penetrated inside the tank shunts

laminated with a lower electrical conductivity than the tank, the eddy current created by these leakage fluxes would be less than in the absence of tank shunts.

In addition to the 3D model, a 2D model of the case study is created in order to calculate the eddy current loss using the method described in section 4.3.5. In this model, as seen in Figure 4-14, the windings are separated into 10 parts to account for leakage fluxes between the windings and the non-uniformity of eddy currents inside the windings. As expected in normal conditions, the leakage flux in the winding is low and peaks in some sections up to 0.12T. In addition, the flow of leakage is greater in the center of the windings than at the top and bottom.

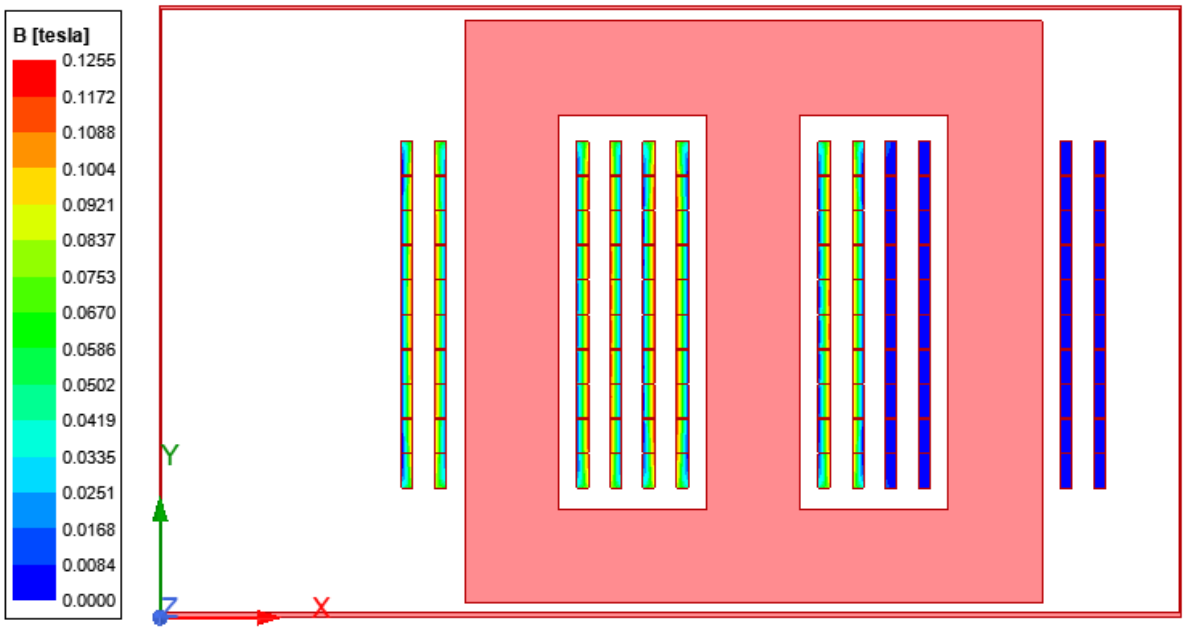

Figure 4-14. The leakage flux density (T) inside the transformer windings in 2D model

When GIC happens, a zero-sequence current with the same direction and magnitude is injected into all the transformer windings, as explained in section 2.4. In this study, it is assumed that this transformer is subjected to the 225 A GIC at the neutral of the winding (75 A per phase), which is the North American Electric Reliability Corporation (NERC) standard suggested limit for the GIC

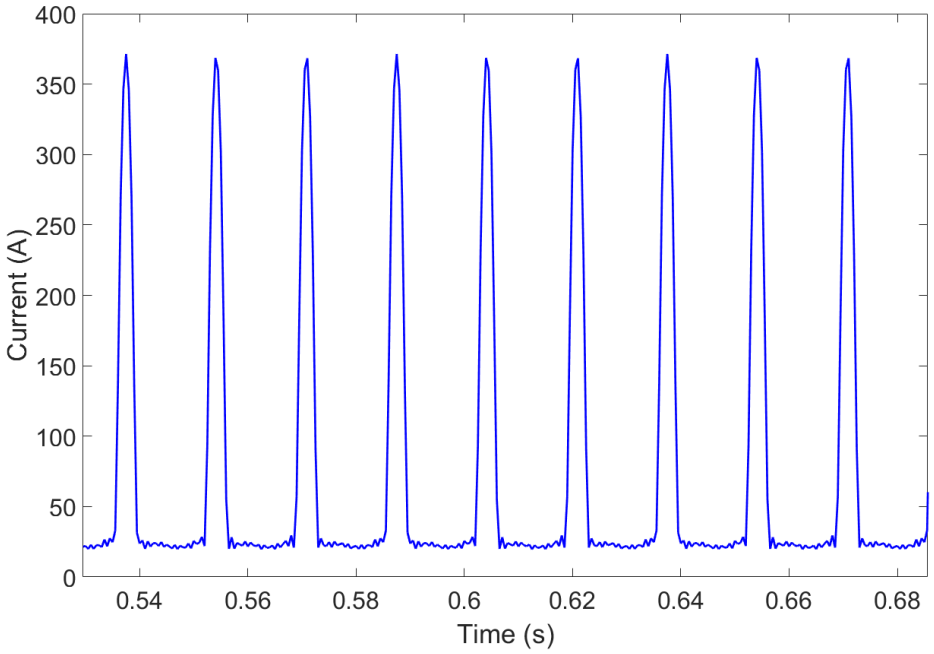

Figure 4-15. The current injected in the transformer windings during the 75 A GIC per phase

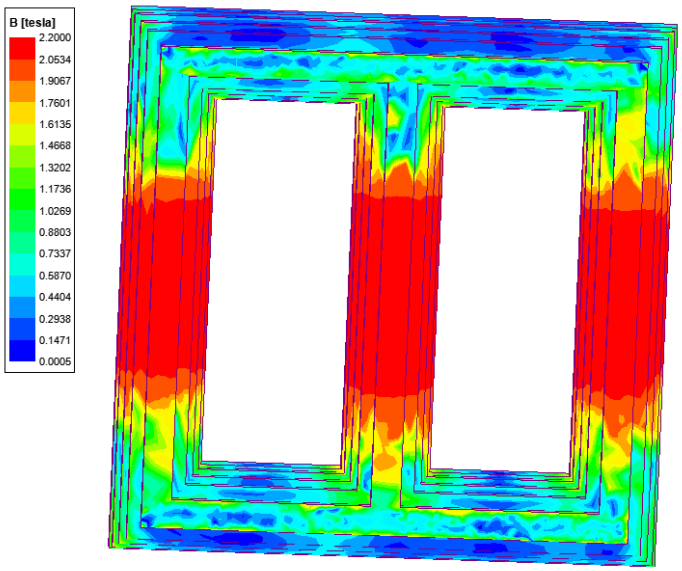

Figure 4-16. Core saturation of the transformer during the 75 A GIC per phase

tests. The injected current into the transformer windings is calculated by EMTP-RV and presented in Figure 4-15. As expected, when this current excites the transformer, it becomes saturated, and the magnetic flux reaches 2.2T, which is the transformer's saturation level. In addition, all structural components of the transformer, including the tank and clamps, are saturated as well.

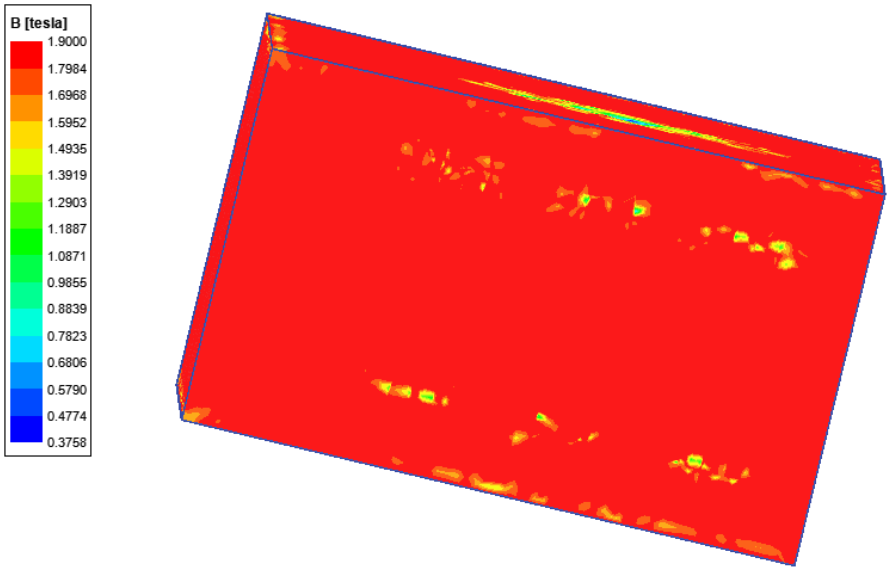

Figure 4-17. Tank saturation of the transformer windings during the 75 A GIC per phase

This indicates that a substantial amount of eddy currents is created in these areas, resulting in substantial stray losses relative to normal conditions. Figure 4-16 and Figure 4-17 present the magnetic flux density inside the transformer during the GIC.

4.4.2 Thermal Analysis of the Structural Parts

After performing the electromagnetic analysis, the electrical loss of the transformer should be calculated to be considered as the heat source in thermal analysis. Figure 4-18 and Figure 4-19 depict the stray loss in the transformer tank and clamps under normal conditions, respectively. The loss distribution resembles the leakage flux distribution because it is the source of eddy currents. The average stray losses in normal loading are 4821.05 W and 4759.66 W for the tank and clamps, respectively. The stray losses of the structural parts under different GIC levels are shown in Table 4-2. As expected, with increasing the GIC level, the stray losses increase drastically compared to the normal condition.

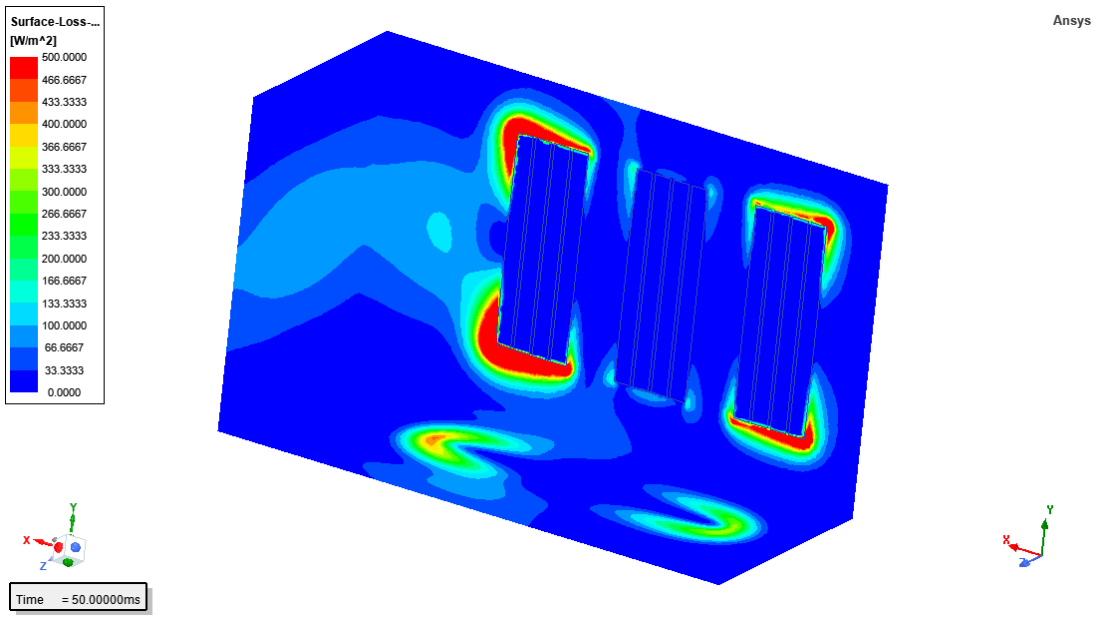

Figure 4-18. Surface loss density at 50ms considering normal loading. The average surface loss density of the tank is 4821.05W

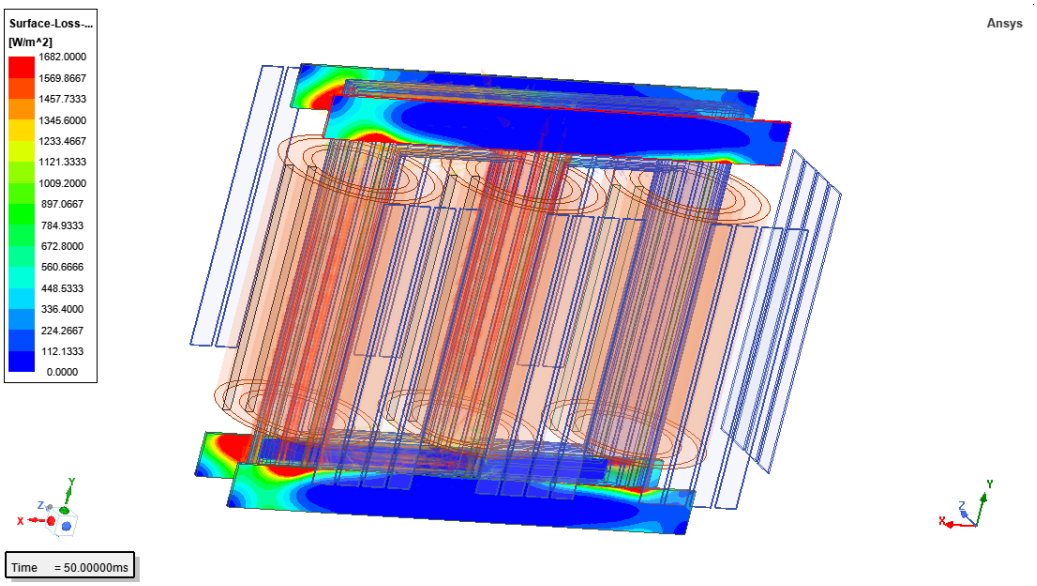

Figure 4-19. Surface loss density at 50ms considering normal loading. The average surface loss density of the clamps is 4759.66W

The structural parts cooling is accomplished mostly by natural convection. Obviously, radiators also cool to some amount by radiation; however, this effect is negligible in comparison to convective cooling [11]. The tank is filled with transformer oil, the temperature of which varies

Table 4-2. Stray losses of the structural parts under different GIC levels

GIC Level per phase (A)	**Stray losses of the tank (W)**	**Stray losses of the Clamps (W)**
Normal- without GIC	4821.05	4759.66
40	36595.2	20413.4
66	123600.1	34166.93
75	144003.25	39647.58
100	217340.28	51978.33

depending on the oil's location. Thus, the clamps are in contact with the natural oil flow inside the tank. On the other side, the ambient temperature cools the tank's exterior walls. Thus, by modeling the internal natural convection by oil for the clamps and both internal and external natural convection by oil and ambient temperature for the tank, the HST of the structural parts can be found. The typical formula of convection modeling is:

$$q_0 = h(T_{ext} - T) \tag{4-24}$$

where q_0 represents the convective heat flux, h represents the convective heat transfer coefficient, and T_{ext} represents the external temperature which is the oil or ambient temperature for the tank walls. In this research, the ambient temperature is always assumed to be 30 ^{0}C. Although oil temperature fluctuates throughout the tank, the top oil temperature is normally 55 ^{0}C to 65 ^{0}C higher than the ambient temperature. On the other hand, the temperature of the bottom oil may rise 17 ^{0}C over the ambient temperature. This makes the upper walls of the transformer and clamps more susceptible to hot spot heating. In addition, the commercial FEM software can calculate the convective coefficient h automatically based on the problem.

As the GIC might be characterized as emergency transformer loading, Table 4-3 presents the allowed temperature limit during the GIC based on the IEEE 60076-7 standard. Any values beyond the stated limit may threaten the transformer's safety and reliability.

Table 4-3. Permissible limits of the temperature during emergency loading based on IEEE 60076-7

Parameter	**Limit values**
Top-oil temperature	110 ^{0}C
HST of windings and metal components adjacent to cellulose insulation	150 ^{0}C
Ambient temperature	30 ^{0}C

Figure 4-20 compares the HST of the tank based on the average stray loss during the normal condition and different GIC levels. It can be seen that when GIC happens, the HST of the tank increases compared with the normal condition, which is 82.61 ^{0}C. The HST increases as the GIC level increases, and it surpasses the IEEE 60076-7 permissible limit of 150 ^{0}C for GIC larger than 66.6 A. The HST of the tank reaches 372.14 ^{0}C under 66.6 A GIC while it is 107.16 ^{0}C for 40A GIC. This is because at 40A GIC, the core is not saturated, and the peak of magnetic flux density is less than 2.1T. However, under 66.6A or higher GIC levels, the core becomes saturated, resulting in higher stray losses in the structural parts, such as clamps and the tank. In addition, the HST is obtained based on the NERC suggested GIC level and one level behind that. Figure 4-20 demonstrates that with 75 A GIC, the HST can easily pass the permissible limit after about 140 min.

The same analysis is performed to compare the HST of the clamps during different GIC levels. Figure 4-21 indicates that even 40A GIC leads to greater HST than normal loading with a HST of

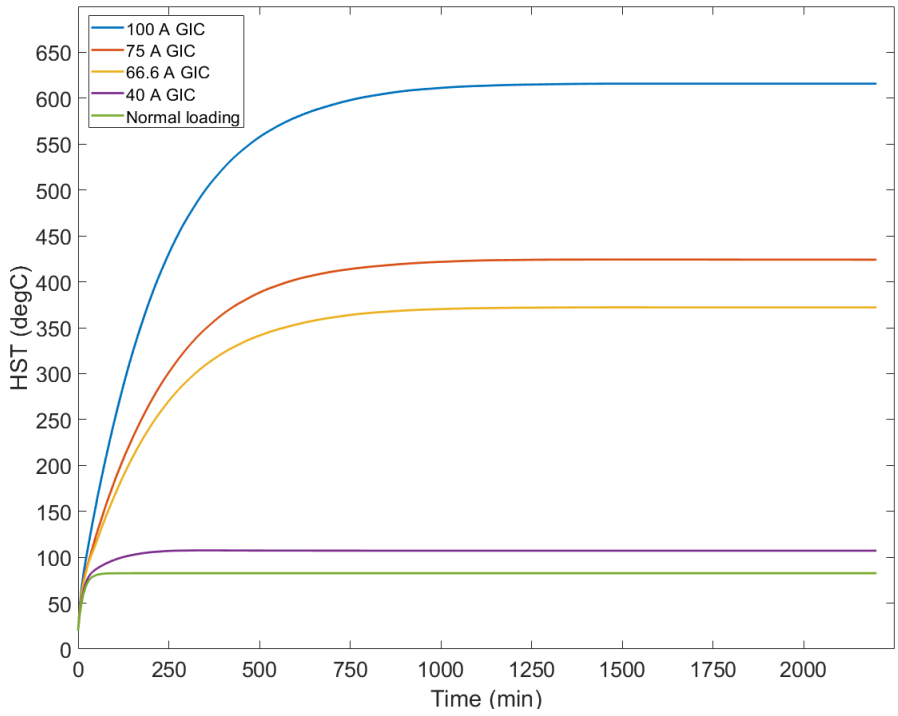

Figure 4-20. HST of the transformer tank during the different GIC level

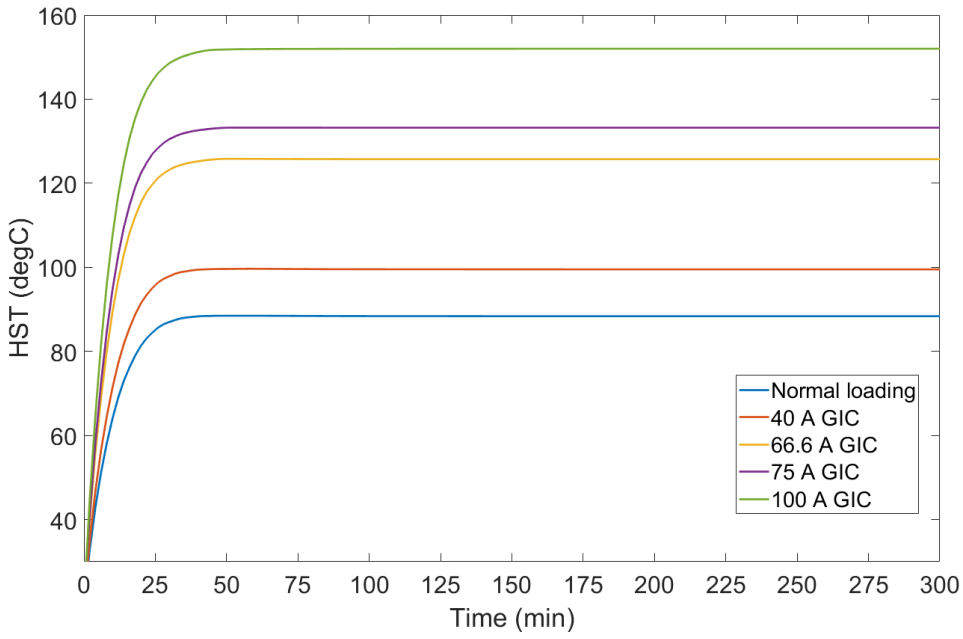

Figure 4-21. HST of the transformer clamps during the different GIC level

88.38 ^{0}C. Similar to the tank case study, due to the core saturation for 66.6 A GIC and higher than that, the HST of clamps under such GIC are significantly greater than the normal condition.

Although for 66.6 A and 75 A the temperature rise over the ambient temperature is 95.72 ^{0}C and 103.21 ^{0}C, the permissible limit is not violated. On the other hand, with 100 A GIC, the HST reaches 152.4 ^{0}C and exceeds the limit.

Figure 4-20 and Figure 4-21 illustrate that the GIC is a hazardous event for the structural parts of the transformer, especially for the tank. Because any temperature rise over the allowable limits reduces the transformer lifetime and danger its reliability. It should be noted that IEEE 60076-7 suggestion for emergency loading is only for two hours. However, the GIC may last up to 24 hours, making the situation more dangerous.

4.4.3 Thermal Analysis of Windings

In order to calculate the temperature distribution inside the transformer windings, the material properties of the mineral oil, paper, and copper are used according to Table 4-4 in which *k* is the thermal conductivity, ρ is density, C_p is the heat capacity at constant pressure, and μ_t is the dynamic viscosity of the mineral oil. Based on Table 4-4, when oil temperature rises, its density, thermal conductivity, and dynamic viscosity all drop, but its specific heat at constant pressure follow the same pattern.

Table 4-4. Thermal material properties of windings

Property	**Mineral oil**	**Copper**	**Paper**
k **(W.m^{-1}.K^{-1})**	$0.1509 - 7.101 \times 10^{-5} \times T$	401	0.19
ρ **(kg. m^{-3})**	$1098.72 - 0.712 \times T$	8933	930
C_p **(J.kg^{-1}.K^{-1})**	$807.163 + 3.58 \times T$	385	1340
μ_t **(Pa.s)**	$0.08467 - 0.0004 \times T + 5 \times 10^{-7} \times T^2$	-	-

A number of horizontal channels that join two vertical channels make up the cooling system of a disc-type winding. Figure 4-22 demonstrates one of 12 passes of the computational domain for the case study SV winding. This pass consists of 12 discs and 13 horizontal channels. The oil washers at the top and bottom of the pass serve to induce zig-zag cooling in the transformer winding by forcing oil to enter from one vertical channel and depart from the opposite vertical channel. The horizontal and vertical oil duct thicknesses are 5 mm and 4.5 mm, respectively.

Along with Navier-Stokes equations presented in section 4.2.2, a set of boundary conditions is implemented for this study. First, the fluid domain has an inlet boundary condition that specifies a mass flow rate (or oil velocity) and an oil temperature. In this study, the inlet boundary is specified at the bottom of the winding with 0.057 m/s oil velocity and 46.7 ^{0}C Temperature. Furthermore, the absolute pressure is adjusted to zero at the domain exit. Finally, the fluid outlet should be placed on the border where the oil will depart. The heat source is also set by the

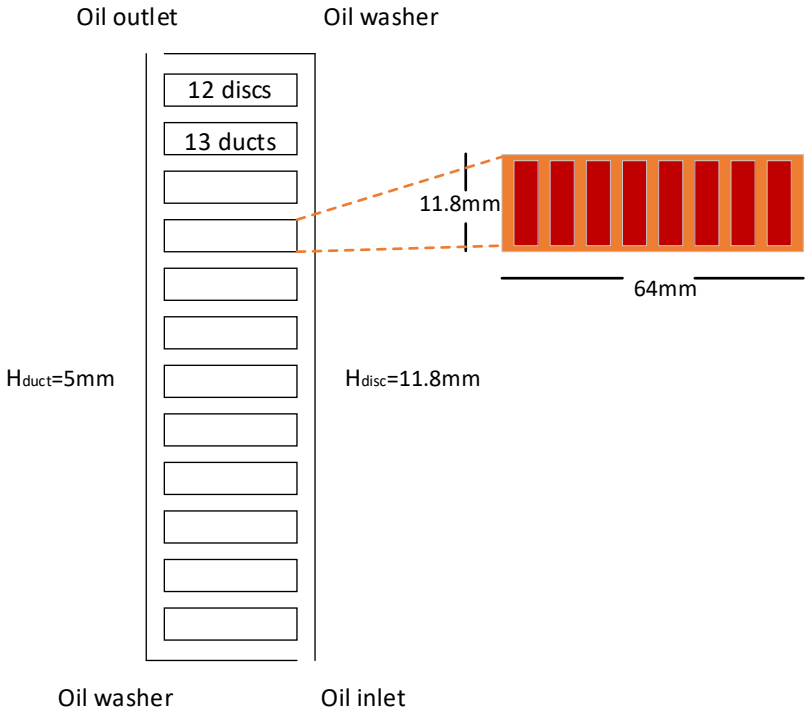

Figure 4-22. One pass of the SV winding geometry

volumetric heat source found by the electromagnetic calculation explained in section 4.3.5. The DC resistance of SV winding is 0.524 Ω. Thus, based on ((4-12) and ((4-22), the DC and eddy current losses in one phase of the SV winding in normal condition is 47.8 kW and 2.15 kW, respectively.

Figure 4-23 presents the temperature distribution inside the SV windings. The HST of the

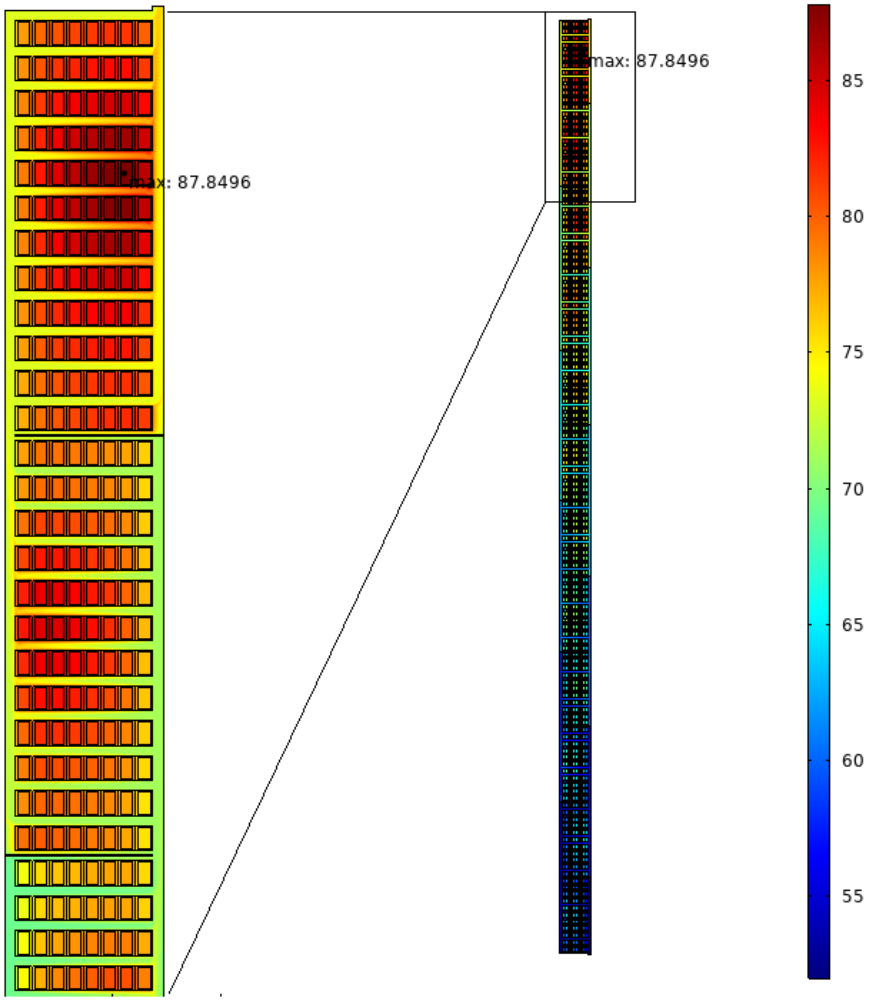

Figure 4-23. Temperature distribution inside the SV winding of the transformer.

windings is 87.85 ^{0}C which is 57.58 ^{0}C more than the ambient temperature. As can be seen, the upper passes of the windings are hotter than the lower passes. This is because the oil with lower temperature enters from the bottom of the windings and transfers the heat by itself to the upper

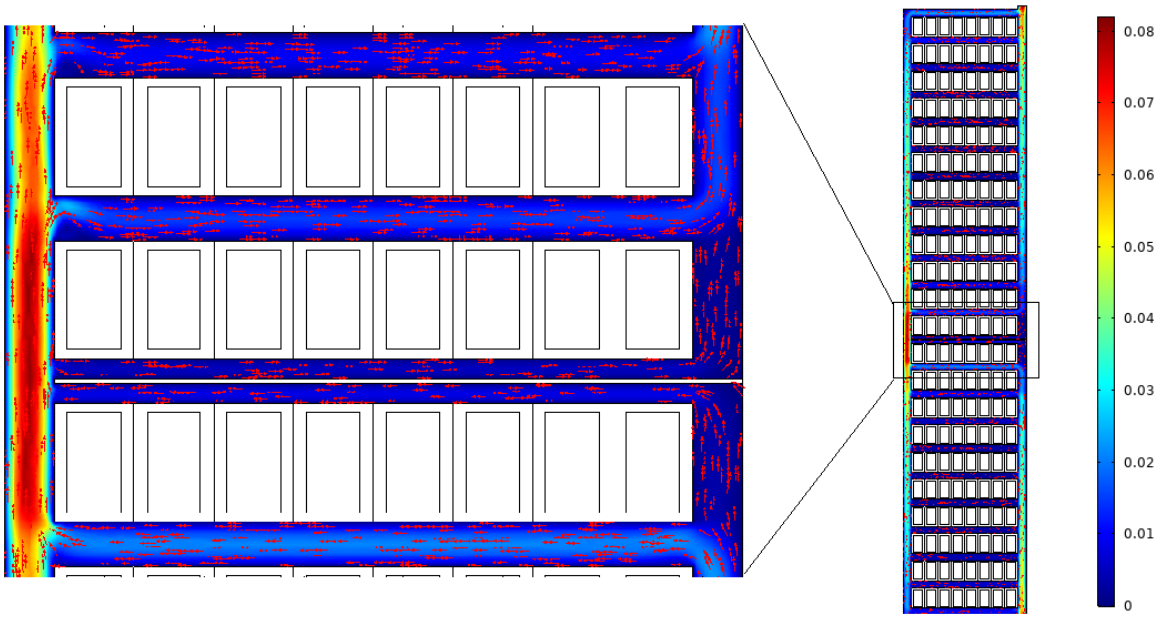

Figure 4-24. Oil flow inside the ducts of the SV winding.

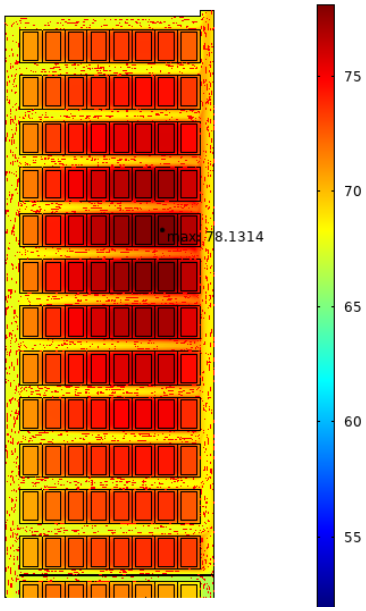

Figure 4-25. Temperature distribution inside the windings during 100A GIC

parts. The HST is located on the fifth disc from the top of the top pass and on the outlet boundary side, which is expected. In addition, by flowing the oil, the hot area moves to the right and left sides of the winding in different passes, which is due to the zig-zag cooling systems by the washers. Figure 4-24 presents the oil flow inside the vertical and horizontal ducts of the winding. Due to

the conservation of mass, the mass of oil remains constant on every pass; thus, at the washer gates, the oil velocity is higher than in other parts.

The same study is performed to find the HST of the SV windings for 100 A GIC per phase. First, the amount of DC and eddy losses are calculated based on ((4-12), ((4-13), and ((4-22) as 21.3 kW and 9.88 kW . Then, considering the same thermal and fluid boundary conditions, Figure 4-25 depicts the HST of the winding with 100 A GIC per phase. In this case, the HST is 78.13^0C which is less than the HST in normal conditions. This simulation shows that unlike the structural parts, the GIC may not create a hazardous situation in the windings of the transformers.

4.5 Conclusion

In this chapter, first, the finite element method was briefly explained. Then, the governing equations for the electromagnetic and thermal analysis of the transformer were presented. The FEM modeling of the transformer was described in detail for both electromagnetic and thermal analysis. The key part of obtaining the HST of the transformer was estimating the transformer losses accurately. To do that, the methods to calculate losses inside both active parts and structural parts were separately discussed. Finally, the results of several simulations were shown to compare the HST of the transformer's components in normal loading and under different GIC levels. The results revealed that the structural parts, such as the tank and clamps, were saturated with a low amount of GIC, resulting in high stray losses. These losses caused the hot spot heating, especially in the tank, in a way that for 40 A GIC, the hot spot heating was 24.55 ^{0}C greater than the hot spot heating under normal loading. However, the situation became even worse when the core was saturated. Due to the core saturation, the HST of the tank and clamps jumped drastically under 66.6 A and higher GIC to peaks at 152.4 ^{0}C and 615.8 ^{0}C for the clamps and the tank under 100A

GIC, respectively. Finally, the effect of GIC on the HST of the windings was investigated. The results showed that no problematic situation may occur for the windings since under the worst-case study, 100 A GIC, the HST is 9 ^{0}C is lower than the HST in normal loading. Therefore, during the GIC, the structural parts are highly in danger and must be monitored and protected to prevent transformer failure.

Chapter 5

Transformer Bushing Thermal Model

5.1 Introduction

Power transformer bushing is one of the most important parts of the transformer. It is an insulating component for carrying the HV conductor through a grounded structure. The reliability of power transformers is highly dependent on the performance of bushings. Several factors affect this performance, such as electrical, thermal, and mechanical stresses. Among these, thermal stress is a major concern because not only does it reduce bushing lifetime, but it also may cause bushing failure.

During the bushing operation, some amount of electrical energy is dissipated in the bushing. These power losses act as a heat source and cause the temperature to increase significantly inside the bushing. Besides, power utilities are becoming increasingly interested in the prospect of overloading the transformers beyond the nameplate rating, even up to 100%, to meet the load demand increase as it is more economically viable than installing a new transformer [112], [113].

Under such conditions, bushings are usually overloaded without considering their overload capabilities. If the bushing temperature rise increases beyond the permissible limits, the bushing failure is likely. Consequently, the prediction of hotspot temperature (HST) and the evaluation of temperature distribution and fluid flow of the bushings is of paramount importance in both design and operation stages.

Various studies have been carried out to determine the HST in the bushings. Generally, the prediction methods of HST and temperature distribution in the bushings can be divided into two different traditional and numerical methods. In traditional methods, researchers try to propose a simple mathematical thermal model using lumped-parameter models, such as thermal-electrical analogy models, to predict HST [113]–[119]. McNutt et al. [114] proposed a simple mathematical thermal model derived from analogous thermal models. This approach presents three constants, which are determined by thermal tests. With these predetermined parameters, this model can only estimate the HST of the bushing. The IEEE standard guide C57.19.100 for the application of power transformer bushing [115] also employs McNutt's equations to estimate the temperature rise at the hottest spot of conductor for bottom-connected bushings with no appreciable dielectric losses and no cooling ducts [114]. Another method [116], [117] presented a model based on an iterative approach. This method has been used to handle the dependency of the model parameters on temperature. In addition, this method can provide a temperature profile along the conductor without any prior temperature measurements. In [118], the authors tried to propose an economical means of determining the HST and performance of high voltage bushing under overloading conditions. They used the finite difference method to solve the thermal-electrical analogous circuit model and estimate the bushing HST. However, the proposed model results are noticeably different from the test results. An improvement to the McNutt's model [114] is suggested in [119] to use

only two parameters instead of three parameters. These traditional methods have proposed fast and simple models to estimate HST; however, the internal natural convection of the bushing is not considered in these models. In fact, since heat convection in the bushing oil is a complicated phenomenon [112], the previous models assume that it can be lumped into thermal conduction, which is not an accurate assumption.

Unlike traditional methods that still rely on analytical formulas, numerical methods are solely based on solving the governing PDEs. In [120], a model is introduced to predict the temperature distribution of resin-impregnated paper (RIP) bushing based on PDEs. The temperature pattern of the whole bushing conductor is calculated by the Bessel function and solving a nonlinear second-order problem. Nonetheless, this model is incapable of dealing with nonlinearity and complex geometries. In [121], the finite element method (FEM) is used to solve joule heating equations and estimate the temperature pattern of RIP oil-SF6 bushing to optimize the inner structure insulation. In [122]–[125], conduction is considered as the main mechanism for heat transfer in the bushings, and the joule heating problem is solved using FEM to find temperature distribution in oil-impregnated paper (OIP) and RIP bushings, under both steady-state and overloading conditions. However, in [122]–[125], internal convection is not considered because CFD was not applied in their methods.

A complete electromagnetic-fluid-thermal analysis has been introduced in [126], [127] for RIP bushing; nevertheless, only the convection of ambient air and oil in the transformer tank are considered, which are external natural convection. Also, [128] performs a CFD analysis on a RIP bushing; however, the oil flow dynamics is not studied since there is no oil inside this type of bushing. Hence, the impacts of internal natural convection of bushing oil on the temperature distribution and HST inside the bushing have not been considered and investigated, mainly due to

its challenging nature. Furthermore, there is no investigation in the existing technical literature on the effects of overloading conditions on the convective thermal behavior of the bushings. On the other hand, the numerical methods have some disadvantages as they typically need intensive computation, longer execution time, and large computer memory, and they subject to runtime divergence concerns.

This chapter presents a new approach for the prediction of temperature distribution and HST in OIP bushings standing on the Thermal Equivalent Circuit (TEC) model, which the FEM model modifies. First, the traditional TEC model is presented using basic electrical-thermal analogous equations. Then, the challenging internal natural convection problem in the bushing oil is modeled by FEM for various load currents, and the associated HST is calculated. In the next step, the TEC model is modified using FEM results by adding convection thermal resistances to deal with the accuracy concerns of the traditional TEC model. The proposed model is applied to a 245 kV, 800A bushing, and then the temperature distribution and oil flow are obtained at the nameplate rated current, using COMSOL Multi-physics. In addition, the analysis is performed considering 1.1pu, 1.2pu, and 1.25pu currents to investigate the effect of typical overloading on the HST of the bushing. Besides these analyses, the impact of oil flow is studied for different transformer top oil temperature (TTOT) and load currents. The results reveal that in the overload cases, the HST exceeds the permissible limits. And finally, the nonlinear characteristics of the convection thermal resistances of the bushing is obtained so that it can be used for future works to overcome the drawbacks of the numerical techniques.

5.2 Modeling of Bushing Thermal Equivalent Circuit

In this section, the concept of heat transfer in a bushing is discussed to demonstrate the role of

different bushing parts in this process. Then, the theory of CFD and thermal-electrical analogy are explained by mathematical equations, and finally, the proposed model is presented.

5.2.1 Heat Transfer Mechanisms and Heat Sources in a Bushing

During the operation of transformers, when electrical current passes through their bushing conductor, a part of electric energy is dissipated and converted to power loss because of the conductor's resistance. Although this power loss is relatively small compared with the total transformer loss, it is the main heat generation source in the bushing and can significantly increase its internal temperature. Also, the bottom of the bushing is submerged in the transformer oil. Hence, the heat from the transformer top oil may increase the temperature rise in the bushing. Insulation dissipation also occurs in the bushings. However, it is noticeably low and can be neglected.

As illustrated in Figure 5-1, the generated heat is transferred to the surrounding insulation and different parts of the bushing. Conduction and convection are the main mechanisms of heat transfer in this structure. Conduction is a mechanism in which the heat inside a bushing is transferred from higher temperature areas to lower temperature areas with physical contact. The other mechanism, i.e., convection, is heat transfer by the movement of the bushing oil. Due to the fact that the density of oil depends on the temperature, the temperature gradient in different parts of the oil leads to the oil density gradient in a bushing. Consequently, because of body force which is due to gravity, the parts of oil with higher density fall, and the lighter part rises. This oil movement helps the bushing to cool down; however, due to the low velocity of oil in the bushing, the effect of convection on the cooling process is low compared with conduction.

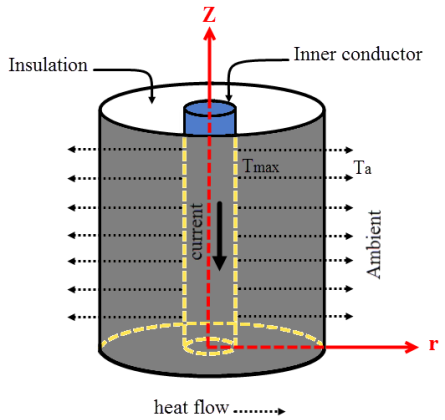

Figure 5-1. The heat flow direction in a bushing

5.2.2 Thermal-Electrical Analogy

Two systems are considered to be analogous when they both have similar equations and boundary conditions, and the equations describing the behaviors of one system can be transformed into the equations for the other by simply changing the symbols of the variables [23]. In the thermal-electrical analogy, temperature plays the role of voltage which causes heat to flow in a similar fashion to the flow of charge in an electrical circuit. Also, like electrical resistance in electrical systems, thermal resistance limits heat flow produced by temperature differences. The analogs equations are [114]:

$$I = \frac{\Delta V}{R} \tag{5-1}$$

$$Q = \frac{\Delta \theta}{R_T} \tag{5-2}$$

where I is electrical current (A), ΔV is the voltage difference (V), R is electrical resistance (Ω), Q is heat flow (W), $\Delta \Theta$ is the temperature difference (K), and R_T is thermal resistance (W/K).

In order to find a TEC model of the bushing, the bushing is divided into three different zones, including the top, middle, and bottom of the bushing, as shown in Figure 5-2. For each zone, the

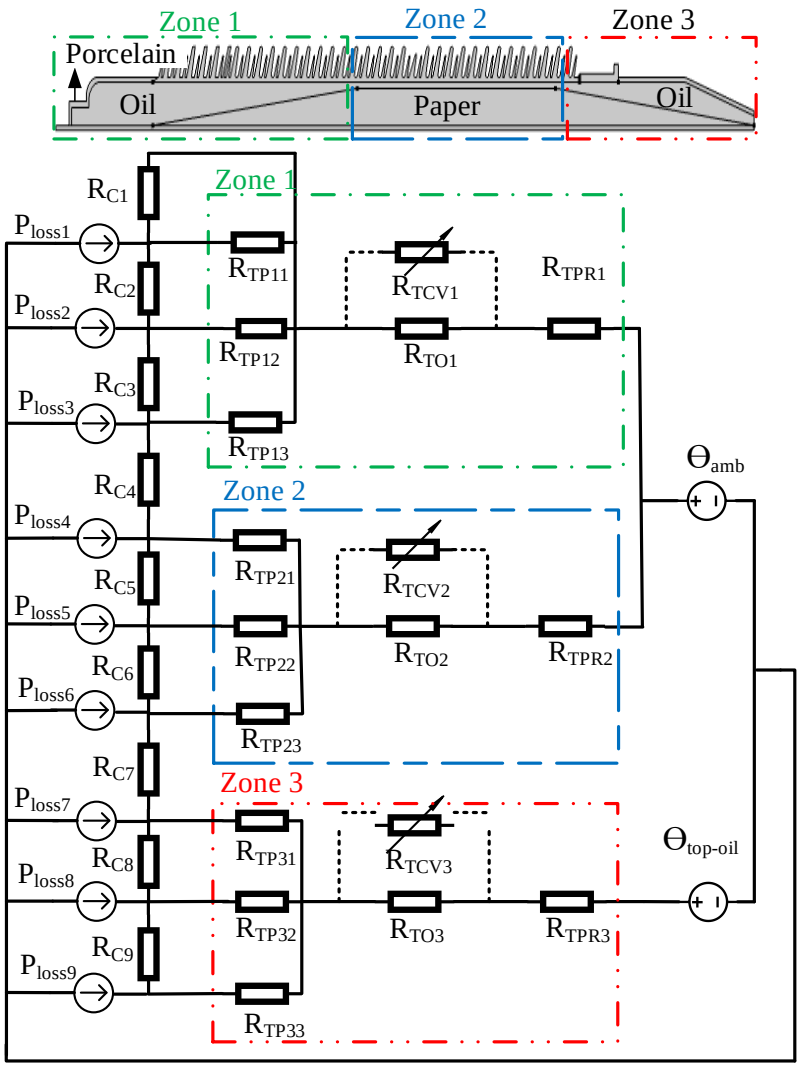

Figure 5-2. Proposed TEC model for OIP bushing under steady-state condition

thermal resistances should be defined according to the heat transfer mechanisms. Also, all heat sources and boundary conditions should be presented by current and voltage sources. To account for the thermal conductance of the conductor, the axial resistances are considered to model the heat transfer along the conductor [125]. The heat generated in the bushing is the power loss which can be expressed as:

$$P_{lossi} = I^2 \times R_{Ci} \tag{5-3}$$

where R_{Ci} is the axial thermal resistance of the conductor at node i. This power loss acts as a current

source in the proposed model shown in Figure 5-2. Also, two voltage sources Θ_{amb} and $\Theta_{top\text{-}oil}$ are presented to model the effects of both ambient temperature and transformer top-oil temperature on HST, respectively.

In order to find conduction thermal resistances, the basic formulas are utilized as follows:

$$R_T = \frac{L}{kA} \tag{5-4}$$

where L is length (m), A is the area (m^2), and k is thermal conductivity ($Wm^{-1}K^{-1}$). Since the bushing has cylindrical geometry, (5-4) becomes:

$$R_T = \frac{\ln(r_o/r_i)}{2\pi Lk} \tag{5-5}$$

where r_o is the outer radius (m), and r_i is the inner radius (m). In this regard, R_{TPi} is the conduction thermal resistance of paper in zone i, R_{TOi} is the conduction thermal resistance of oil in zone i, and R_{TPRi} is the conduction thermal resistance of porcelain in zone i. All these resistances are calculated by (5-5).

Generally, the convection thermal resistance is calculated by (5-6),

$$R_{Tcv} = \frac{1}{hA} \tag{5-6}$$

where h is the convective heat transfer coefficient ($Wm^{-2}K^{-1}$). Also, R_{TCVi} is the convection thermal resistance in zone i. However, finding h is very complicated for considering internal natural convection in a bushing [112]. To deal with this problem, these resistances are calculated by modifying the TEC model based on the FEM model. According to the CIGRE report regarding the transformer thermal modeling [45], the CFD strategy is the best way to improve the accuracy of TEC thermal design models. This may be feasible by deriving more accurate coefficient formulations as compared to the known "textbook" formulations, which depend on simplified

geometries and assumptions about temperature and flow distributions [45]. Although using experimental data would be more accurate, we assume that the CFD method can be utilized to model the convection phenomenon in an OIP bushing as well as the transformer winding. Therefore, in the present paper, the FEM model based on CFD is utilized to find the accurate convective resistances of the bushing. It should be noted that the thermal models for OIP bushing would be different for vertical, horizontal, or inclined mounting due to gravity, and the presented model is based on vertical mounting.

5.2.3 FEM model Based on CFD Strategy

The main idea of FEM is to divide the entire domain into smaller parts, referred to as finite elements, and then obtain the algebraic equations for each element which is much easier than solving the governing equations for the entire domain. The CFD method, which is employed in this study, relies on the solution of the Navier–Stokes equations, which consist of the Continuity equation, Momentum equation, and Energy equation. For an incompressible fluid, e.g., insulating oil, these equations can be written as follows [129]. The continuity equation is expressed as,

$$\frac{\partial \rho}{\partial t} + \nabla.(\rho U) = 0 \tag{5-7}$$

where ρ is the local fluid density, and U is the velocity vector. The momentum equation is presented as,

$$\frac{\partial (\rho U)}{\partial t} + \nabla.(\rho U \times U) = -\nabla p + \mu(\nabla^2 U) + F \tag{5-8}$$

where p is the pressure, μ is the dynamic viscosity of the fluid, and F is the buoyancy force. The right-hand terms of (5-8) are the pressure force, the viscous force, and the buoyancy force, respectively. The latter represents the force that drives the flow in natural convection regime, and

it is related to the density gradients in the fluid [87]. Hence, in natural convection, the buoyancy force is equal to:

$$F = g(\rho - \rho_\infty) \tag{5-9}$$

Simplifying these equations is, however, possible in most applications and the resulting equations constitute the Boussinesq approximation [130]. This method is used in natural convection problems so as to reduce computational costs and achieve convergence. With the Boussinesq approximation, all the fluid properties are constant except in the body force term, where the fluid density varies as:

$$\rho - \rho_\infty = -\rho_\infty \beta (T - T_\infty) \tag{5-10}$$

where ρ_∞ and T_∞ are an arbitrary reference and linked by the fluid state equation, and β is the coefficient of thermal expansion at constant pressure, defined as

$$\beta = -\frac{1}{\rho}(\frac{\partial \rho}{\partial T}). \tag{5-11}$$

Hence, the momentum equation becomes

$$\frac{\partial(\rho U)}{\partial t} + \nabla.(\rho U \times U) = -\nabla p + \mu(\nabla^2 U) - g\rho_\infty \beta (T - T_\infty) \tag{5-12}$$

Finally, the Energy equation is

$$\frac{\partial(\rho c_p T)}{\partial t} + \nabla.(\rho c_P U T) = \nabla.(k \nabla T) + S_E \tag{5-13}$$

where c_p is specific heat capacity, k is thermal conductivity, and S_E is the heat source contribution. In this problem, power loss produces heat, and thus it is considered as the heat source. Therefore, according to the joule heating equation:

$$S_E = I^2 R \tag{5-14}$$

where I and R denote the electric current and electrical resistance, respectively.

It is obvious that for the solid domains, e.g., conductor, the temperatures are computed by solving the heat conduction equation [73]:

$$\frac{\partial(\rho c_p T)}{\partial t} = \nabla.(k\nabla T) + S_E \tag{5-15}$$

Also, boundary conditions play a prominent role in the FEM model. In the proposed model, there are different types of boundary conditions for both heat transfer and electrical physics, such as air convection in the outer boundary, top oil temperature in the transformer tank, rated current and voltage, and the grounded flange.

5.3 Solution Method

To solve the set of equations with coupling multi-physical domains in FEM software environment, the algorithm with the following steps is employed, which is also depicted in Figure 5-4:

Step 1- Geometry and material specification:

In the first step, the geometry of the bushing is drawn. Then, the required material properties of each domain are assigned according to the equations.

Step 2- Mesh generation:

Mesh generation plays a prominent role in solving the problem, and the computational domain should be discretized in a way that helps to avoid any convergence instability. The boundary layer meshing, for instance, is applied to all fluid wall domains, shown in Figure 5-3.

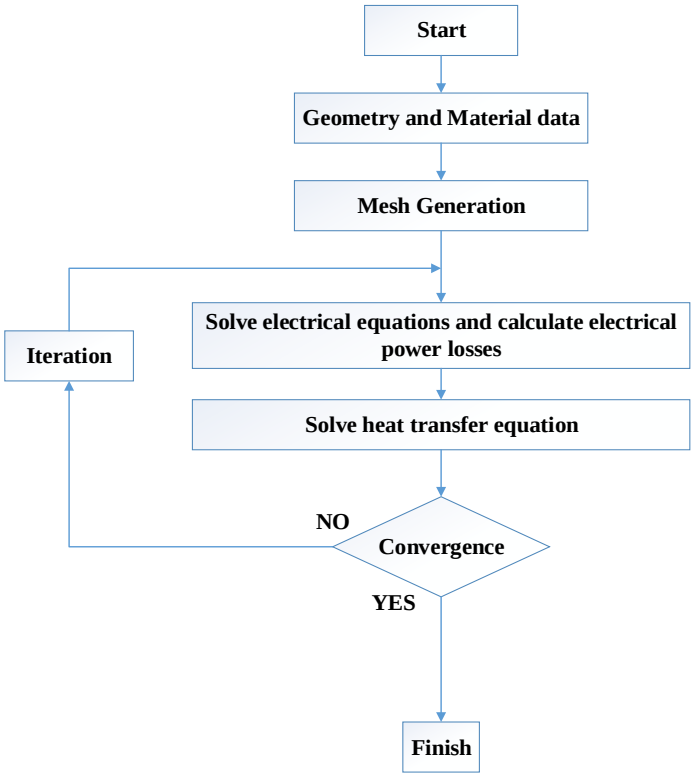

Figure 5-4. The proposed approach for the FEM model.

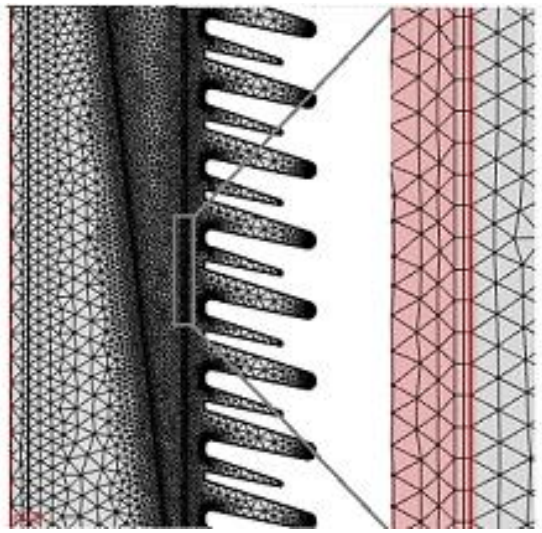

Figure 5-3. The boundary layer meshing around the fluid walls.

Step 3- Solve electrical equations to find electric power losses:

According to the bushing ratings, electric current and voltage are applied as electrical inputs.

Also, the flange domain is connected to the ground. In this step, the electric power losses are calculated according to ((5-3) and will be used as a heat source for the next step.

Step 4- Solve the heat transfer equations in all domains:

Temperature and velocity are calculated by solving Navier–Stokes equations. To do so, in addition to the heat source, which is calculated in Step 3, boundary conditions should be specified correctly. For the heat transfer domain, there are two convection domains to be considered i) the external natural convection with the ambient air for the outer wall of the bushing from the flange to the top, and ii) external force convection with the transformer top oil from the flange to the bottom of the bushing. Although in most literature, the Dirichlet condition (constant temperature) is suggested for the outer wall of the bushing, simulation of the external convection is considered in this study which is more accurate. Besides, the current density and absolute pressure should be defined for electromagnetic and fluid dynamic equations, respectively.

Step 5- Check convergency:

In this step, the conditions of convergence should be checked. It should be mentioned that due to the low velocity of the fluid, achieving convergence may be challenging. To deal with this problem, the variation of parameters or relaxed convergence criteria should be applied in the solver.

Step 6- Iteration:

The above-mentioned steps should be iterated until the convergence condition of Step 5 is satisfied. The number of iterations should be high enough to achieve convergence.

5.4 Simulation Results under Steady-State Condition

In this work, COMSOL Multi-physics is used to implement the proposed algorithm for the FEM model on an 800A, 245kV transformer OIP bushing. Then, the TEC model is developed in MATLAB. The typical structure of the bushing is shown in Figure 5-5, where number 1 is the conductor of the bushing, and it is made of aluminum. Number 2 specifies the insulation, which is OIP. Number 4 is the insulating oil located between OIP and the bushing wall, made of porcelain and identified by number 5. The flange of the bushing is number 6, and it is made of steel. Table 5-1 presents the required material specifications of the different parts of the bushing, including density, specific heat, and thermal conductivity.

Table 5-1. Bushing Material specification

Material	Density (kg/m^3)	Specific heat (J/(kg.m))	Thermal conductivity (m.K)
Aluminum	2700	900	238
OIP	584	1968	0.3
Oil	877	1893	0.124
Porcelain	2400	1085	1.5

To demonstrate the capability of the proposed solution method, a sample 800A, 245kV transformer OIP bushing is considered, and the temperature distribution and hot-spot temperature are calculated. The geometry and dimensions of different parts of the bushing are shown in Figure 5-6 and Table 5-2. In this analysis, the ambient temperature is assumed to be 30 ^{0}C. Furthermore, TTOT is assumed to be 95 ^{0}C which is 65 ^{0}C temperature rise over the ambient temperature,

according to the IEEE C57.19 [115].

Table 5-2. Longitudinal geometry of the bushing

Label	L1	L2	L3	L4	D1	D2
Length (mm)	3518	2150	685	480	30	300

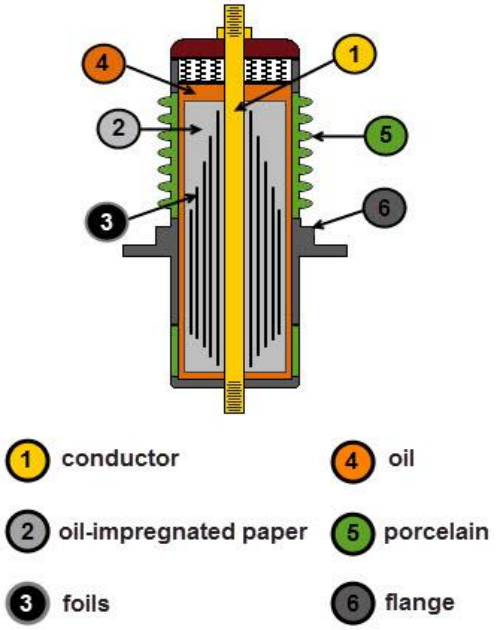

Figure 5-5. A sample OIP bushing showing different parts of the bushing

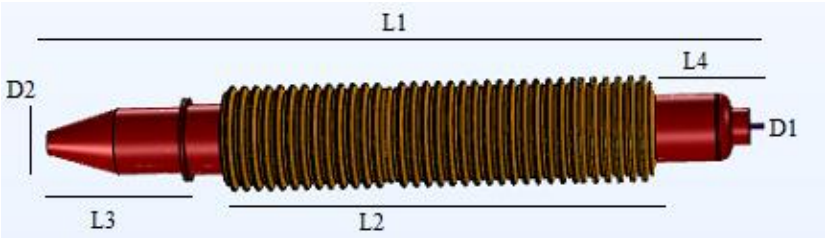

Figure 5-6. OIP bushing under study with dimensions given in Table 5-2.

5.4.1 FEM Model Results

Under the rated bushing current of 800A, the temperature distribution in the bushing in 2D and 2D axisymmetric views are shown in Figure 5-7 and Figure 5-8, respectively. The maximum temperature is 102.84 ^{0}C located in the conductor in the vicinity of the flange. However, the temperature of the conductor varies from top to bottom of the bushing. The different temperature distribution on the top and bottom of the bushing is due to the following reasons. First, the bottom of the bushing is located in the 95^{0}C transformer oil at full load condition, whereas the top part is surrounded by ambient air and cooled by convection. Such a different cooling situation also causes oil circulation with higher velocity flow in the top part of the bushing compared with the bottom.

Figure 5-9 shows the fluid velocity and direction of oil flow in the bushing. The main reason

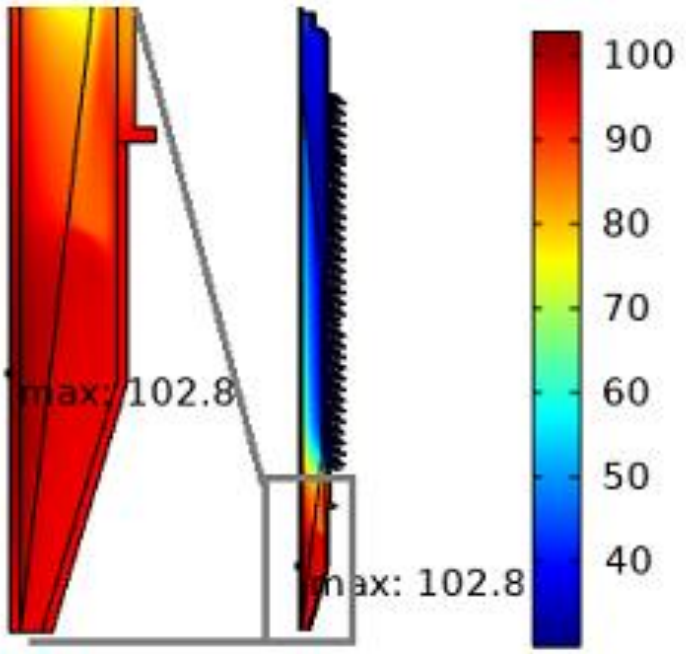

Figure 5-7. The 2D temperature distribution in the bushing, the maximum temperature is 102.8 ^{0}C which is located on the conductor near the flange.

for fluid flow is the temperature difference between the walls surrounding the oil space. Accordingly, with the bushing bottom located in the transformer tank, the difference between the

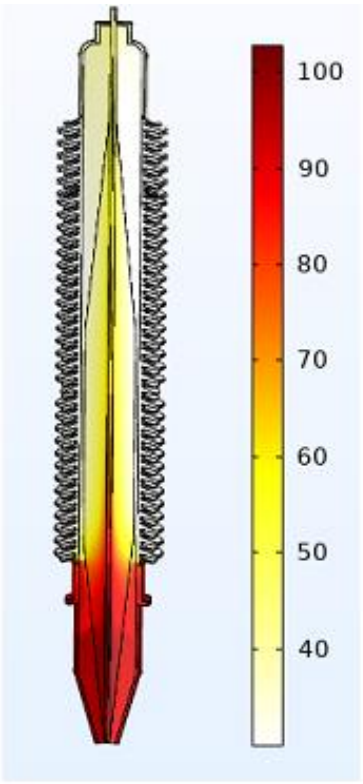

Figure 5-8. The 2D axisymmetric temperature distribution in the bushing (^{0}C)

temperature of the outer wall (equal to TTOT of 95 ^{0}C) and that of the inner wall is relatively low for the bushing bottom oil. As a result, the fluid velocity is very low. On the other hand, in the top portion of the bushing, one of the walls is close to the porcelain with a temperature close to the ambient temperature. Therefore, the bushing top oil flow is faster than the bottom oil flow, reaching a maximum velocity of 3.9e-4m/s. This faster oil circulation also leads to better heat dissipation and a lower temperature in the top part of the bushing, which can be observed in the simulation results of Figure 5-7.

The temperatures of Figure 5-7 and Figure 5-8 show that the operation of the bushing under its nameplate rating is normal, and no problematic situation is noticed. The hotspot temperature rise of the bushing over the ambient is 72.84^{0}C which is less than the suggested maximum temperature rise of 75^{0}C for safe operation, according to the IEEE standard C57.19 [3].

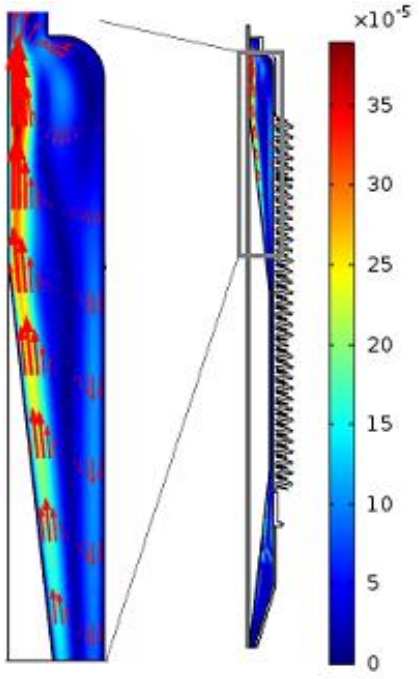

Figure 5-9. The oil circulation velocity demonstrating internal natural convection in the bushing with the maximum top oil velocity of 3.9e-4 m/s

In the second case study, the effect of bushing overloading on its HST is investigated. It is assumed that the rated current of the bushing equals the rated current of the corresponding transformer. When the bushing under study subjects to 10%, 20%, and 25% overloading, the bushing HST varies along the bushing conductor, as shown in Figure 5-10. Although the overall pattern of the temperature variations in Figure 5-10 is the same for the various loading currents, the peak values are noticeably different. In all overloading cases, the HST exceeds the permissible limit of 105 ^{0}C. At 25% overloading, the HST is 115.258 ^{0}C; hence, the temperature rise is 85.258 ^{0}C which is about 10 ^{0}C more than the recommended temperature rise by the IEEE standard C57.19. In addition, it is observed that not only the value of HST is changed, but also its location is slightly shifted towards the top of the conductor. The results show that only 4% overloading is high enough to push the HST beyond the permissible limit.

To determine the role of oil flow in heat transfer which is typically ignored in the technical

literature, Figure 5-11 compares the simulation results with and without oil flow dynamics taken into account for 1pu and 1.25pu currents, i.e., 800A and 1000A, respectively. It can be seen that

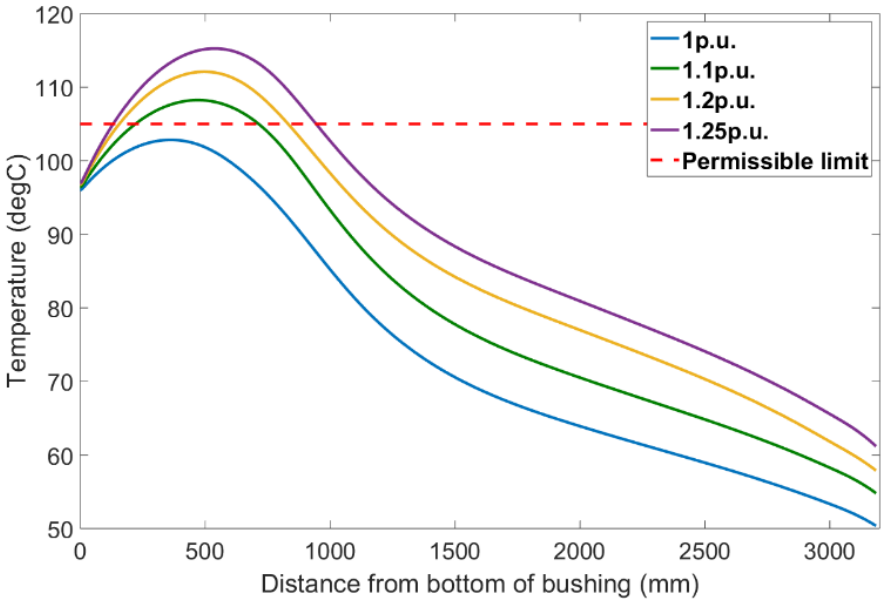

Figure 5-10. Comparison of temperature distribution (^{0}C) along the bushing conductor under different overloading conditions

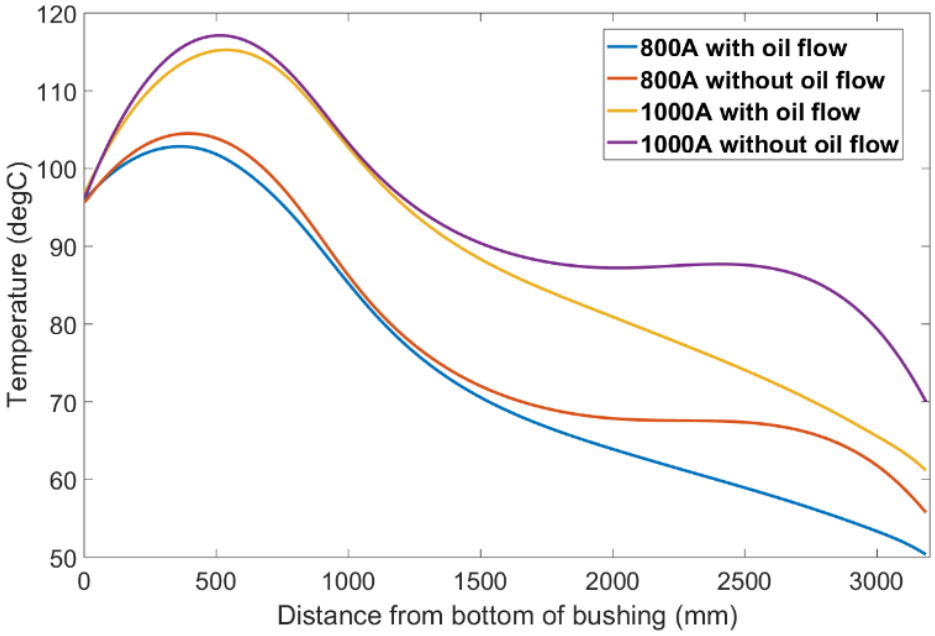

Figure 5-11. Comparison of temperature distribution (in ^{0}C) along the bushing conductor with and without oil flow taken into account for 1pu and 1.25pu loading conditions

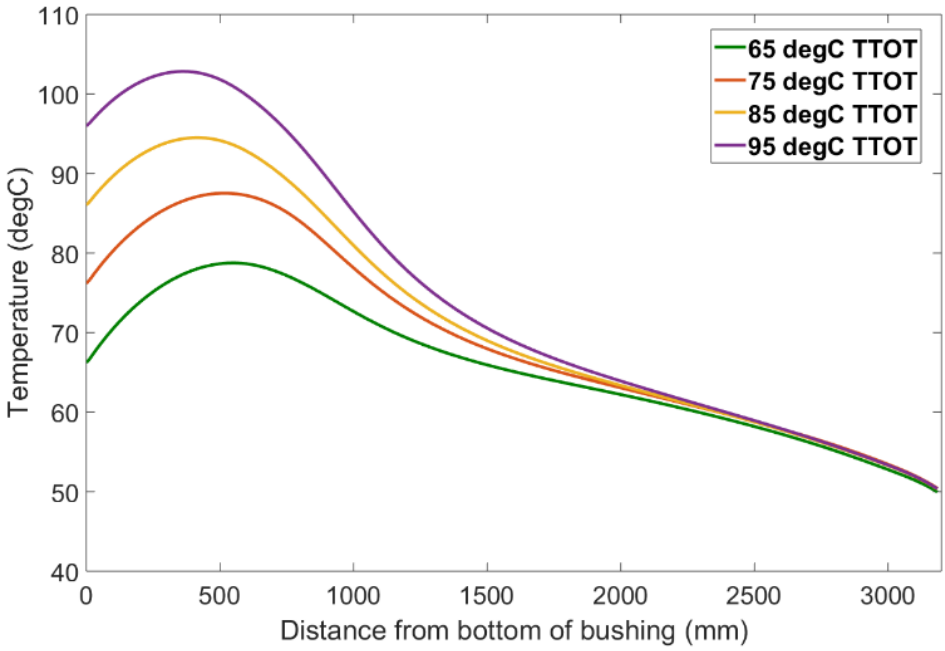

Figure 5-12. Comparison of temperature distribution (in ^{0}C) along the bushing conductor for different transformer top oil temperatures (TTOT)

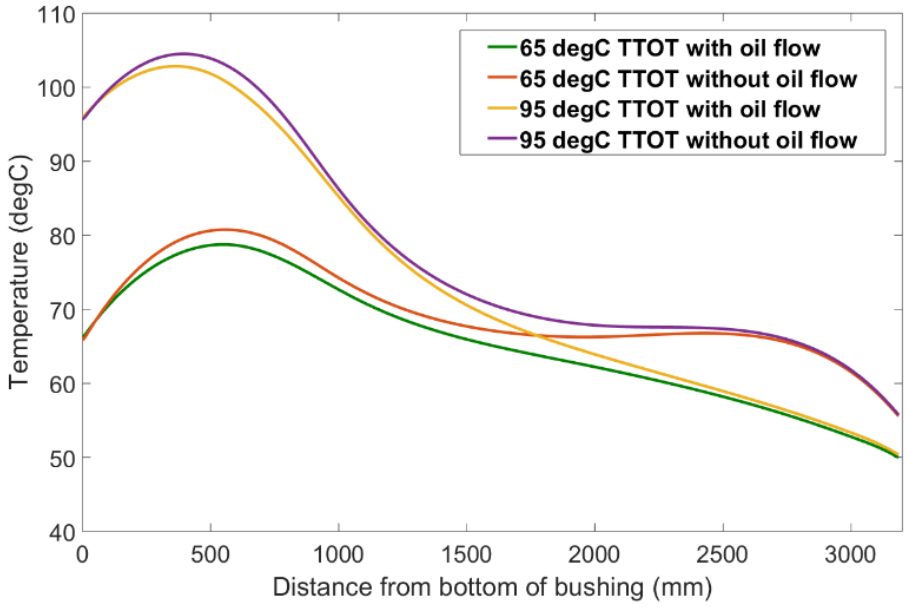

Figure 5-13. Comparison of temperature distribution (in ^{0}C) along the bushing conductor with and without oil flow taken into account for 65 ^{0}C and 95 ^{0}C transformer top oil temperatures (TTOTs)

in both cases, in the top part of the bushing with the higher temperature difference between the walls of oil, the effect of oil flow on transferring heat to the ambient is more than in the bottom of

the bushing, which is located in the transformer tank oil. On the other hand, in the case of 1000A loading, the effect of fluid velocity on reducing the temperature is more than 800A. Moreover, in the middle of the bushing, the difference between temperature distribution with and without oil flow is very small due to the low amount of oil. In addition, it can be observed that oil flow at the top of the bushing reduces the temperature of some parts by more than 10 ^{0}C. It should be mentioned that the overloading condition is based on the bushing rated load (1pu), and it may be different with the overloading of transformers since bushings usually are of a higher rating than transformers.

To determine the effect of TTOT on temperature distribution and oil flow in the bushing, the analysis is carried out with a variation of TTOT between 65 ^{0}C to 95 ^{0}C. The corresponding results are shown in Figure 5-12. It is evident from Figure 5-12 that TTOT has significant effects on HST in a way that by reducing TTOT from 95 ^{0}C to 65 ^{0}C, the HST decreases by 24 ^{0}C. However, due to the effective top oil flow, TTOT does not significantly affect the temperature of the bushing in the top part. Figure 5-13 illustrates the effect of TTOT on oil flow. The difference between the HST with and without considering oil flow is 2.08 ^{0}C and 1.75 ^{0}C for TTOT 65 ^{0}C and 95 ^{0}C, respectively. It shows that for lower TTOT, oil flow can transfer more heat to the ambient, which results in a lower HST.

5.5 TEC Model Results

Based on ((5-4), the conductive part parameters of the TEC of Figure 5-2 are obtained, which are presented in Table 5-3. At 800A rated bushing current, the total power loss is 84.4 W, and if calculated only based on the conduction mechanism, the HST is obtained as 104.8 0C, which is about 2 0C greater than the HST calculated by the FEM model considering internal natural

convection. Considering the FEM model results as a reference, the oil convection thermal resistances are added in parallel with the oil conduction thermal resistances in the TEC model, Figure 5-2. Due to both heat transfer mechanisms, the HST is reduced to 102.8 ^{0}C. The convection resistances vary with power loss and are highly dependent on the temperature difference between the surrounding boundaries. In addition, the oil viscosity is a temperature-dependent parameter. As a result, the convection resistances are nonlinear, which are obtained based on the accurate multi-physics FEM results. On the other hand, the velocity of the oil plays a noticeable role in the heat transfer, as shown in Figure 5-11 for the upper and lower parts of the bushing under study, compared with the middle part which contains very small oil volume with low velocity. Therefore,

Table 5-3. TEC model parameter values

R_{TP11}	R_{TP12}	R_{TP13}	R_{TO1}	R_{TO2}	R_{TO3}	R_{TPR1}	R_{TPR2}	R_{TPR3}
1.34	2.33	3.02	1.9	0.18	0.7	0.11	0.11	0.12
R_{TP21}	R_{TP22}	R_{TP23}	R_{TP31}	R_{TP32}	R_{TP33}	R_{C1}	R_{C4}	R_{C7}
3.45	3.45	3.45	3.02	2.33	1.34	3.01	1.98	1.98

Table 5-4. Convective thermal resistances for different loads

Current (A)	HST (^{0}C)	P_{loss} (W)	R_{TCV2} (^{0}C/W)
800	102.80	84.44	109.28
880	108.24	102.18	33.74
960	112.10	121.60	14.07
1000	115.25	131.94	10.88
1200	133.84	190.00	4.16
1600	180.32	337.79	0.49

it is conceivable to establish the dependency of the nonlinear convection resistances of different bushing parts based on the corresponding oil velocity. According to the FEM model, the average

velocity of the top, middle, and bottom of bushing oil are 5.4093e-5 m/s, 6.4102e-6 m/s, and 3.9663e-5 m/s, respectively. Thus, R_{TCV1} and R_{TCV3} are calculated as follows:

$$R_{TCV1} = 0.12 \times R_{TCV2} \quad (5\text{-}16)$$

$$R_{TCV3} = 0.16 \times R_{TCV2} \quad (5\text{-}17)$$

Table 5-4 presents the HST and the bushing power loss at different loading conditions along with the convection thermal resistance R_{TCV2} values. Also, the nonlinear characteristic of R_{TCV2} versus bushing loading is plotted in Figure 5-14. The results show that with increasing the bushing current, the reference convection thermal resistance R_{TCV2} decreases and drops significantly from a high value of 109.28 ^{0}C/W at the rated current to a very low value of 0.49 ^{0}C/W at 2pu load current.

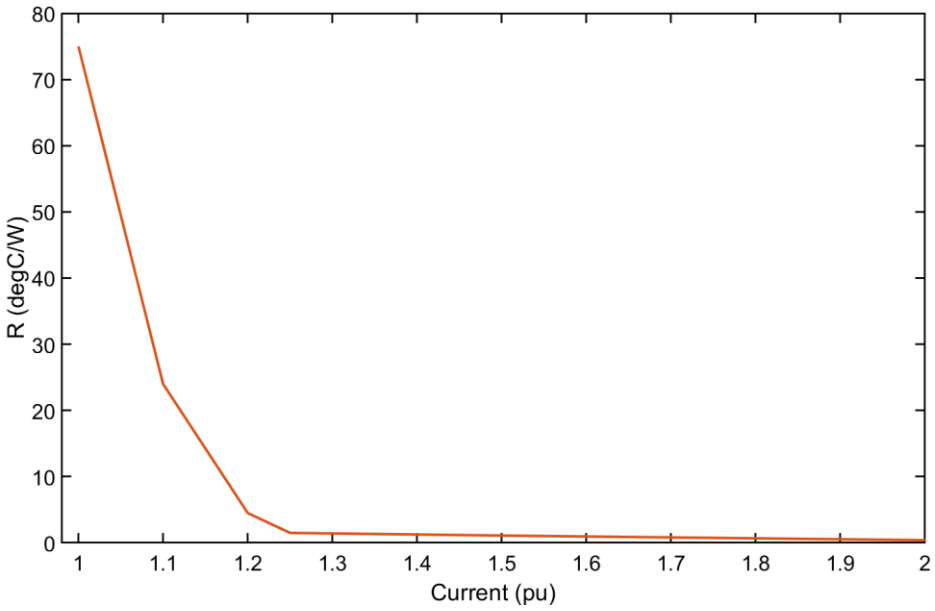

Figure 5-14. Nonlinear characteristic of convection thermal resistance versus bushing load current

With these convection thermal resistances, the proposed TEC model and FEM results at different load currents are aligned, as shown in Figure 5-15. However, without considering these

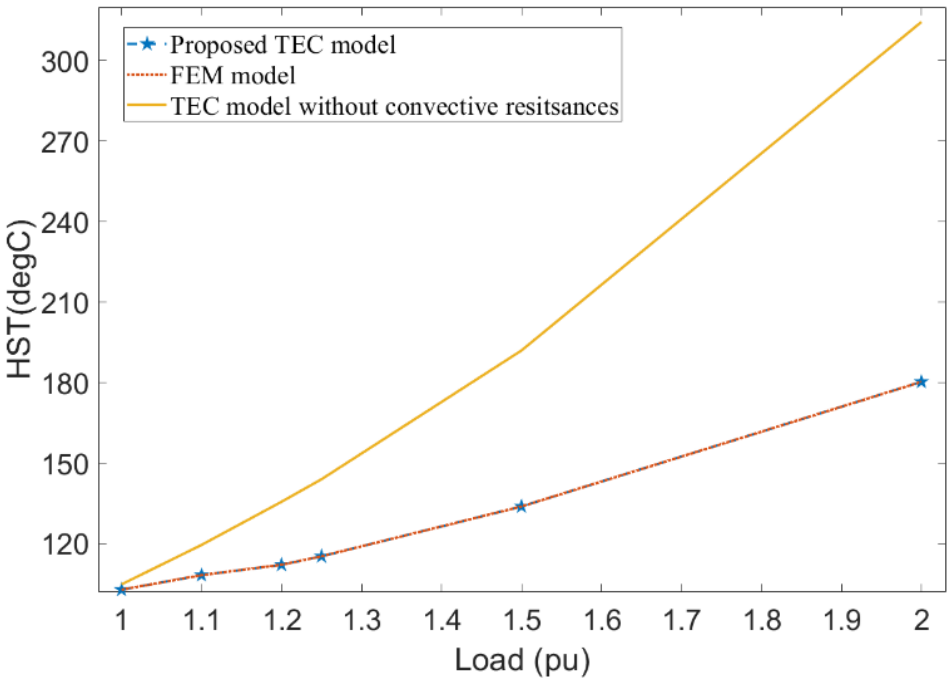

Figure 5-15. Comparison of HST calculated by proposed TEC model, FEM result, and TEC model without convection resistances.

convective resistances, a significant difference can be observed between TEC and FEM results. For 1pu loading, this difference is 2 ^{0}C, but increasing the load results in rising this difference drastically. For instance, the HST calculated by the TEC model at 2pu current is 134.2 ^{0}C greater than the associated HST calculated by both FEM and the TEC model. This further highlights the significance of representing convection heat transfer for the accurate estimation of the bushing HST.

5.6 HST of the Bushing Under GIC

Several studies have been undertaken about the effects of GIC on electric equipment, including transformers [131], wind farms [8], synchronous generators [132], transmission lines [133], and static VAR compensators [134]. However, the impact of GIC on transformer bushings has not yet been investigated. Since the bushing conductor handles the transformer current, it should be

sufficiently robust to withstand the high non-sinusoidal magnetizing current during GIC, which is superimposed on the transformer's normal load current. Such operating circumstances will alter the temperature distribution and hot-spot temperature (HST) of the bushing in terms of thermal stress. Based on the IEEE standard [115], the maximum allowable HST temperature for running a bushing at a rated current is 105 °C. Any extra losses may cause the HST to exceed the limitations, resulting in bushing failure or, at the very least, a shorter bushing lifespan. As the bushing is one of the primary components of a power transformer, it is essential to estimate the bushing hot-spot temperature under GIC to maintain the reliability and longevity of the in-service transformers.

This section investigates the effect of GIC on the thermal behavior of transformer bushings for the first time in the technical literature. First, using the EMTP-RV, the transient analysis is performed to find the current harmonics for the thermal calculations. Then, Bessel functions and Dwight's equations calculate the bushing solid conductor resistance at different frequencies to find the equivalent current. In the next step, a modified TEC model is developed to estimate the HST of an 800A, 245kV OIP bushing under different GIC levels. Also, in-depth investigations on the temperature profile and oil flow inside the bushing are conducted by FEM, with and without GIC. The results reveal that even with 20 A GIC, the HST of a fully-loaded bushing may exceed the permissible limit of the IEEE standard.

5.6.1 Equivalent Bushing Current under GIC Conditions

Since today's electricity grids must accommodate a wide range of nonlinear loads and generating sources, harmonic currents are a prevalent and unavoidable phenomenon. Designers and producers of electrical equipment should be aware of the potential problems that these harmonics might bring. Due to the skin effect phenomena, larger conductor ratings are needed to accommodate the flow of harmonics in the power system. When an alternating current flows

through a conductor, the current density at the conductor's surface is higher than at its core [135]. Hence, losses are higher with respect to those generated by a DC current with the same r.m.s. value [136]. To assess the thermal state of the bushing of a transformer, the skin effect must be taken into account since it raises conductor resistance and reduces its internal inductance [137]. Bessel function techniques proposed by Dwight in 1918 [138] are the most accurate method for calculating resistance. Since then, and using this technique, several publications have been published about the conductor resistance calculation considering the skin effect. Resistances can now be calculated with a high degree of precision, thanks to the increased processing power of computers and the development of more sophisticated numerical calculation techniques.

According to IEC/IEEE standard, the equivalent current is calculated by [136] as an equivalent generating the same total power losses and heat as those of all harmonics:

$$I_{eq-AC} = \sqrt{\frac{R_{dc} I_{dc}^2 + \sum_{h=1}^{\infty} \left(R_h \left(\frac{I_h}{\sqrt{2}} \right)^2 \right)}{R_1}} \tag{5-18}$$

where I_h is the peak current value of the given h[th] harmonic current, R_{dc} is the conductor dc resistance, and R_1 is the AC resistance at the fundamental frequency current.

To calculate the conductor AC resistance at various harmonics (R_h), two methods can be used. The first is using Bessel functions as [139]:

$$R_h = Re\left(i \times R_{dc} \times \frac{mr}{2} \times \frac{(r^2 - q^2)}{r^2} \times \frac{\left[\left(ber\,(mr) + i\, bei\,(mr) \right) + \lambda \left(ker\,(mr) + i\, kei\,(mr) \right) \right]}{\left[\left(ber'\,(mr) + i\, bei'\,(mr) \right) + \lambda \left(ker'\,(mr) + i\, kei'\,(mr) \right) \right]} \right) \tag{5-19}$$

where $\lambda = -\frac{\left(ber'(mq) + i\, bei'(mq) \right)}{\left(ker'(mq) + i\, kei'(mq) \right)}$ and $m = \sqrt{\frac{\omega \mu}{\rho}}$. Moreover, r is outer, and q is the inner radius of

the tube, ber and bei are real and imaginary parts of the Bessel function of the first kind, respectively, and ker and kei are real and imaginary parts of Bessel function of the second kind in respect. Other parameters with prime are derivatives of the corresponding Bessel coefficients. Furthermore, ω is equal to $2\pi f$ where f is the frequency of the ac current in Hz and μ is the permeability of the conductor.

The second approach employs a polynomial equation, a more straightforward formula based on a simplified version of the traditional hyperbolic functions. It is described by Dwight in [140]:

$$R_h = R_{dc}\frac{m.t.(r+q)}{20.r.\sqrt{2}}\left(1+\frac{10}{m.r.\sqrt{2}}+\frac{300}{8.m^2.r^2}\right) \quad (5\text{-}20)$$

where t is the conductor tube wall thickness, and m is:

$$m = \sqrt{\frac{8.\pi^2.f}{10^{11}.\rho}} \quad (5\text{-}21)$$

((5-19) and ((5-20) show the general forms of resistance that are used for tubular conductors. Solid conductor impedance can be easily calculated by considering $q = 0$. The second method, i.e., ((5-20), is a simplified version that can be used only when $m \times t > 40$. Thus, the first method, i.e., ((5-19), with higher accuracy, is selected for this paper analysis.

In this paper, a solid aluminum conductor with a diameter of 30mm is assumed for the studied bushing. Table 5-5 presents the conductor resistances at various harmonic frequencies observed in the transformer current during GIC. Using these resistances and the magnitudes of the current harmonics, the bushing equivalent ac current is calculated based on ((5-18).

Table 5-6 demonstrates the effect of different GICs on the bushing equivalent current when supplying the transformer magnetizing current. As seen in the table, GIC can considerably increase

the conductor current. Adding these currents to the rated bushing current can cause noticeable thermal stress on the bushing, which will be investigated in more detail in the following section.

In order to model the transient thermal behavior, the TEC should involve the thermal capacitances, which can be calculated based on the bushing time constant and the total resistance $R_{tot,i}$ of its parallel branch,

$$C_i = \frac{\tau}{R_{tot,i}} \tag{5-22}$$

where the C_i is the thermal capacitance of branch i, τ is the bushing time constant, and $R_{tot,i}$ is the

Table 5-5. Resistances of the aluminum bushing conductor at various harmonic frequency

Harmonic No.	Resistance	Harmonic No.	Resistance
0	4.63E-05	**7**	9.09E-05
1	4.88E-05	**8**	9.63E-05
2	5.50E-05	**9**	0.000101388
3	6.30E-05	**10**	0.000106135
4	7.10E-05	**11**	0.000110638
5	7.83E-05	**12**	0.00011494
6	8.49E-05	**13**	0.00011907

Table 5-6. GIC effects on the bushing equivalent current when supplying transformer magnetizing current

GIC (A)	$I_{eq\text{-}AC}$ (A)	GIC (A)	$I_{eq\text{-}AC}$ (A)
5	17.576	**75**	178.516
10	33.707	**100**	225.306
20	61.244	**125**	269.119
30	85.214	**150**	311.495
50	126.94	**200**	392.508
66.7	162.567	**300**	544.417

total resistance of the branch between the capacitor nodes. Figure 5-16 presents the proposed TEC considering the capacitances to estimate the HST under GIC conditions.

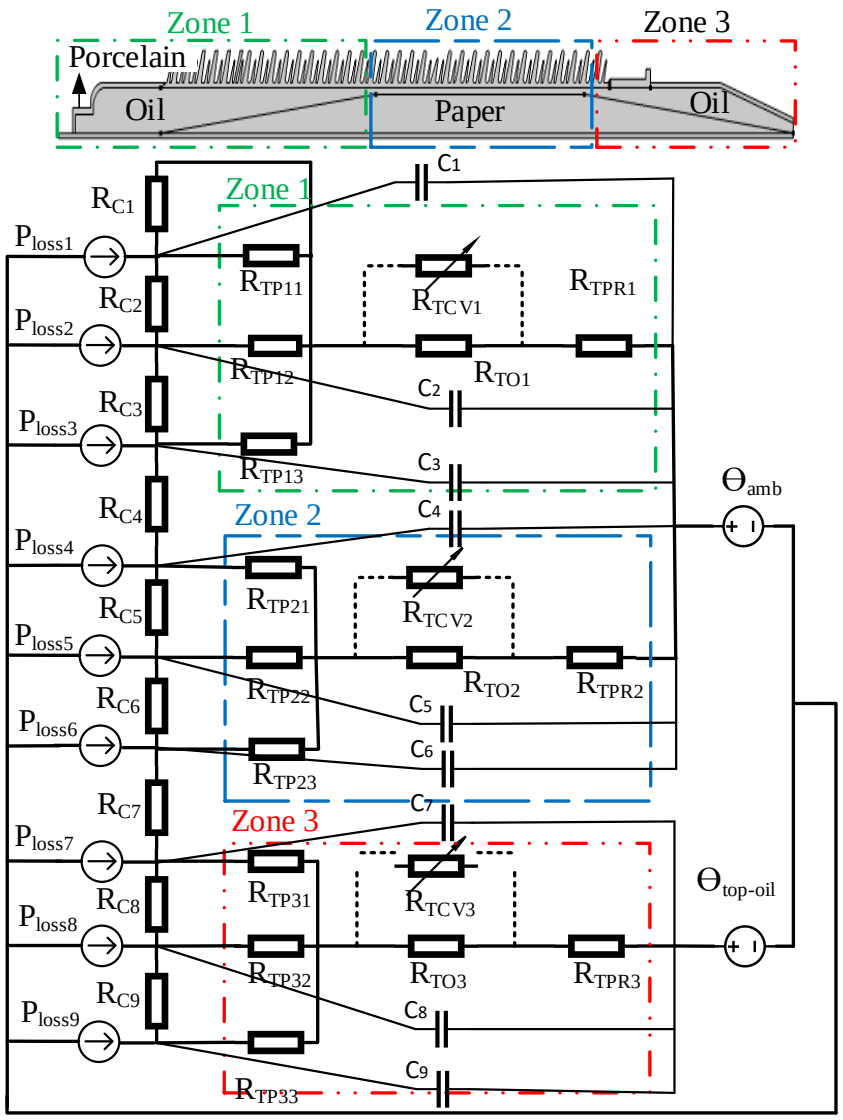

Figure 5-16. Proposed TEC for the HST of bushing under GIC conditions.

5.6.2 Simulation Results under GIC Conditions

This section predicts the HST of OIP bushing under GIC conditions by the CFD-modified thermal equivalent circuit (TEC) model shown in Figure 5-16. To this end, an 800A, 245 kV OIP transformer bushing is implemented in COMSOL Multi-physics [141] to perform the 3D

electromagnetic-fluid-thermal analysis using CFD-based FEM. Then, the results are used to modify a TEC model that can accurately calculate the HST.

During the GIC conditions, the magnitude of the fundamental frequency component of the magnetizing current, I_{mag1}, increases in addition to the other harmonics. This fundamental component current is an inductive current which is added to the normal load current, I_{load}. While the phase angle of I_{load} depends on the load power factor, the phase angle of I_{mag1} is 90°, lagging the transformer voltage. Therefore, the total equivalent current of the bushing varies with the load power factor. As an example, with a power factor of 0.85 lagging, the fundamental current I_1 in ((5-18) is obtained as:

$$I_1 = \sqrt{2}\left(I_{load}\angle - 31.79° + I_{mag1}\angle - 90°\right) \quad 5\text{-}23)$$

According to (5-23), Table 5-6 illustrates the equivalent bushing current under various GICs.

Figure 5-17 displays the 2D temperature distribution of the bushing under the 100 A GIC considering 30 ˚C and 95 ˚C for the ambient and the transformer top oil temperature, respectively. As depicted in Figure 5-17, the HST of the bushing on the conductor during the GIC is 111.04 ^{0}C, which exceeds the permissible limit of 105 ^{0}C in IEEE Std C57.19. During the GIC, not only the value of HST but also its location will change, as shown in Figure 5-17. Because harmonic losses cause more heat dissipation, the HST is moved upward. In addition, due to the temperature difference between the ambient and the transformer top oil, there is a significant difference in temperature between the top and bottom of the bushing conductor. To accurately determine the GIC impact on the bushing thermal behavior, Figure 5-18 compares the oil flow inside the bushing under the bushing rated load current, in the absence of GIC and with 100 A GIC. The temperature difference between the walls surrounding the oil space is the primary cause of fluid flow due to

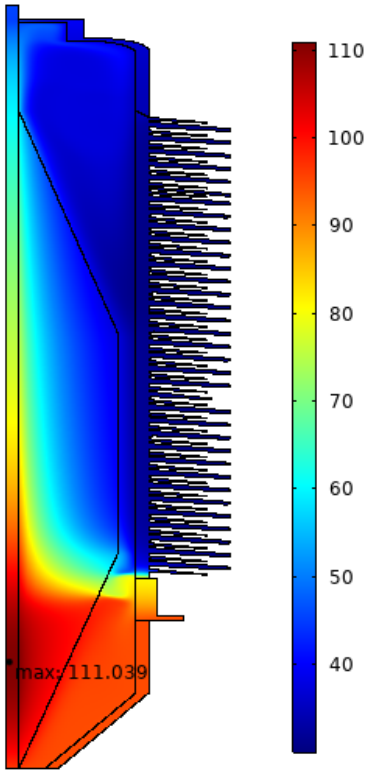

Figure 5-17. Temperature distribution (^{0}C) of the bushing under 100A GIC condition

the oil density change. Thus, during the GIC, as the temperature inside the bushing rises, the oil velocity becomes faster and reaches 6.61e-4 m/s from 3.9e-4 m/s in the normal loading condition.

Although FEM can pinpoint the exact location of HST, the power utilities are more concerned about controlling the operation of the units to keep the temperature rise within the tolerable range

Table 5-7. Steady state HST Estimation under Different GICs

GIC (A)	**HST** (degC)	**GIC (A)**	**HST** (degC)
5	104.15	75	108.51
10	104.57	100	111.04
20	105.35	125	113.194
30	106.07	150	115.38
50	106.68	200	119.55
66.7	107.92	300	132.04

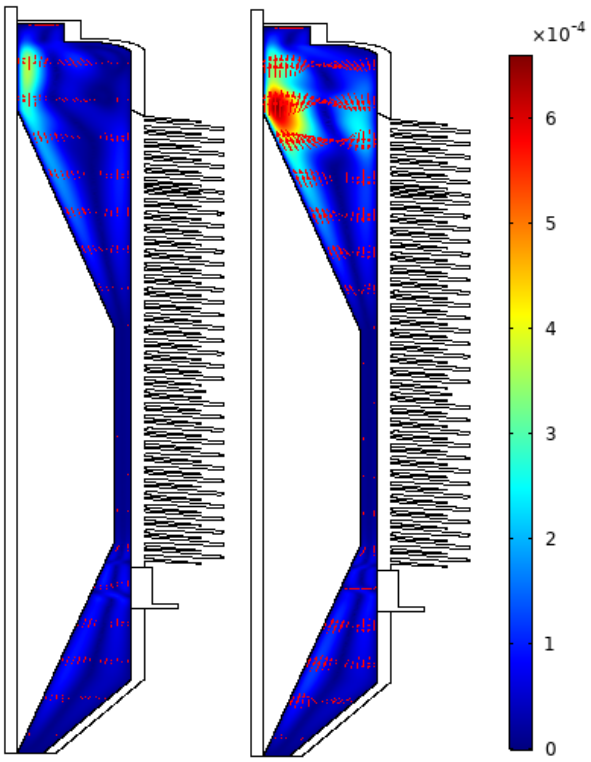

Figure 5-18. Oil velocity (m/s) inside the bushing due to natural convection during a) the normal loading and b) under the 100 A GIC condition.

[17]. As a result, employing a simple yet accurate thermal model for the HST estimation is preferable. The proposed CFD-modified TEC model of Figure 5-16 efficiently satisfies such a need. Table 5-7 shows the bushing HST estimation using this model under various GIC levels and

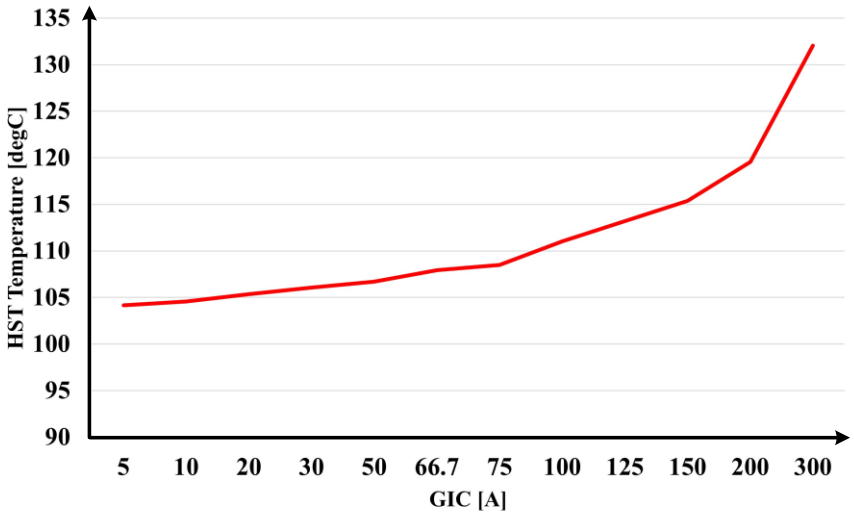

Figure 5-19. Steady state HST trend versus nominated GICs

full-load conditions. Figure 5-19 illustrates the bushing HST as a function of the applied GIC. With the higher GICs, more heat is generated in the transformer bushing, and the rate of rise of the HST increases with the GIC. At the severe GIC of 300A, the bushing HST reaches 132 ˚C, which is well above the standard permissible temperature.

As GIC is a transient phenomenon, both magnitude and time duration are crucial for the bushing thermal studies. Hence, the realistic GIC benchmark signature of the North American Electric Reliability Corporation (NERC) standard [142] is considered with a duration of 24 hours, as shown in Figure 5-20.

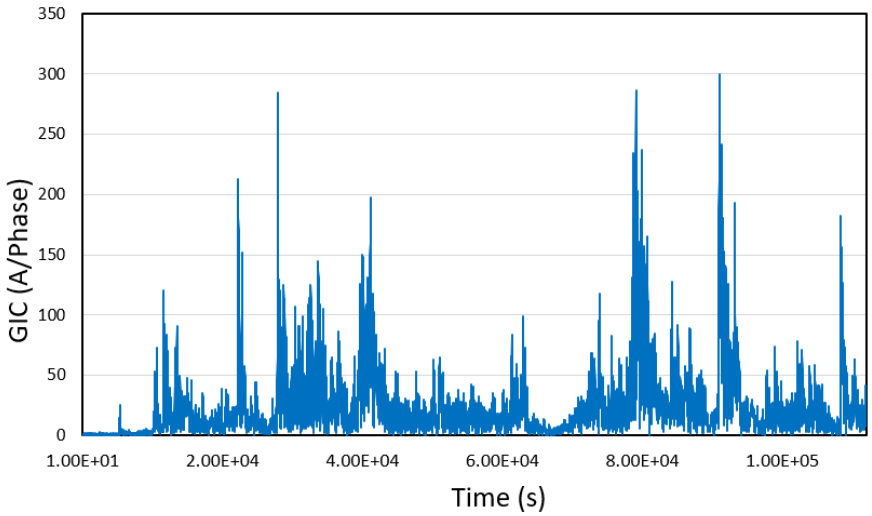

Figure 5-20. Benchmark GIC signature of the NERC standard with the magnitude of 300 A.

Figure 5-21 shows the HST of the bushing for the transient case study based on the CFD-FEM model. In our study, it is assumed that the GIC event occurs while the bushing operates at the rated load current of 800 A. After 24 hours and before the GIC event initiates, the temperature rises to reach the steady-state of 102.8 ^{0}C with a time constant of 2 hours. In the early part of the GIC event with the initial low magnitude, the HST remains around 103 ^{0}C till the GIC peaks at 120A around 27h. From that point, the HST increases to reach 110 ^{0}C; about 7.2 ^{0}C rises from the normal steady-state condition. Under this condition, the HST exceeds the IEEE standard recommended

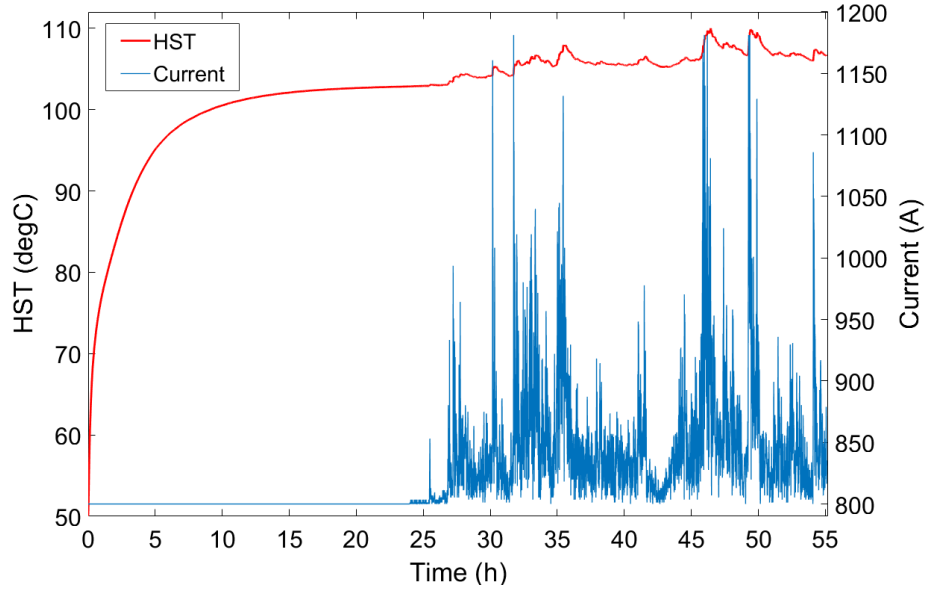

Figure 5-21. HST of bushing during the NERC GIC benchmark event of Fig. 5-20.

permissible limit by 5 ^{0}C. In addition, Figure 5-22 demonstrates the comparison of FEM and the proposed TEC model during a high GIC magnitude period. As discussed in the previous section, in order to model the transient behavior of GIC, nine capacitors are added to the circuit. Based on Figure 5-21 results, the time constant of the bushing is around 2 hours. So, the capacitor values are *C1=545.3, C2=419.3, C3=359, C4=641.7, C5=641.7, C6=641.7, C7=626.6, C8=764.3, and*

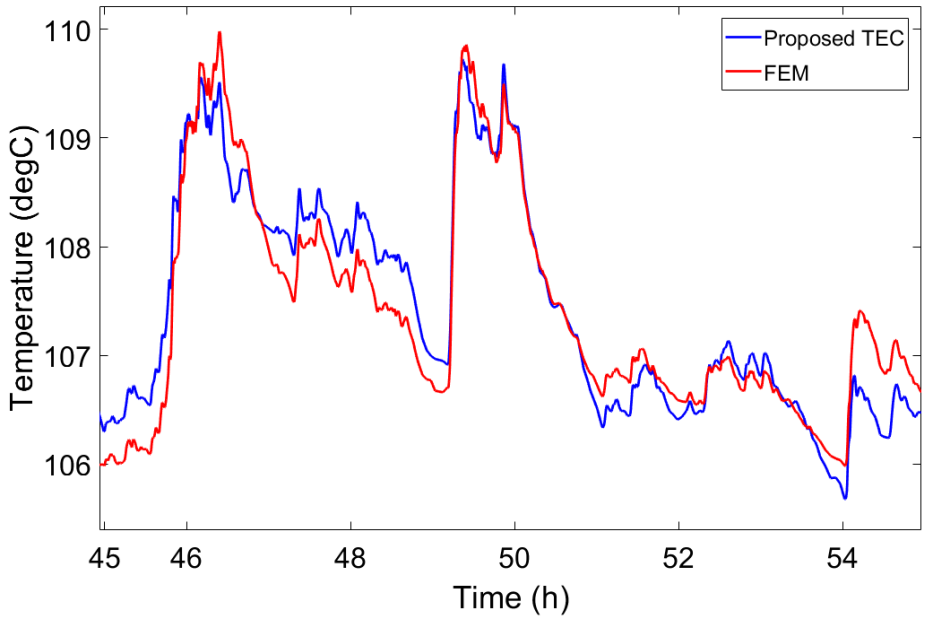

Figure 5-22. HST of bushing during GIC event based on NERC standard

C9=1116 F. Figure 5-22 showsa close agreement between the results of the FEM and TEC models, and the Mean Percentage Error (MPE) is less than 0.5%. This comparison shows the accuracy of the proposed TEC in estimating the HST in the presence of a GIC event.

This study highlights that the GIC effects on thermal stress of the transformer bushing must be taken into account in the design and testing stages by manufacturers. Since generating different GIC-caused harmonics is quite challenging for the testing process, the application of the equivalent current with the proposed calculation approach can significantly facilitate the bushing thermal test. Furthermore, designers must check the GIC impacts on the temperature rise of the bushing in the presence of other factors that may result in a higher tolerance level. Severe thermal stress on insulation can reduce its lifetime, accelerate the aging process, and make bushing more vulnerable to faults or abnormal conditions in the power system.

5.7 Conclusion

Investigation of the temperature distribution and oil flow in the bushings is essential to ensure the safe and reliable operation of the bushing and the associated transformer under various loading conditions. This chapter proposes a new approach to determining the HST of OIP bushing based on the FEM-modified thermal equivalent circuit (TEC) model. To deal with the accuracy issue of TEC models, the nonlinear characteristics of the resultant convection thermal resistances have been obtained. In order to find such characteristics, the temperature pattern and fluid velocity in the bushing have been modeled by FEM. The results reveal that in the absence of convective resistances, a significant difference can be observed between TEC and FEM results, for instance 134.2 ^{0}C at 2pu load. In addition, the effects of different parameters, such as load current, TTOT, and oil flow on HST are investigated. The simulation results show that TTOT has a noticeable

influence on the HST and the temperature distribution in the bottom part of the bushing due to the proximity to the transformer top oil. The HST nonlinearly varies with TTOT; for example, a decrease of 30 ^{0}C in transformer oil temperature results in an HST decrease of 24 ^{0}C. However, the temperature distribution in the top part of the bushing is not affected by the TTOT because of ambient temperature and the high convection rate in that area.

In addition, the results reveal that the oil flow in the top of the bushing has a high velocity compared with the bottom of the bushing, and this leads to better heat dissipation and a temperature drop of more than 10 ^{0}C in some parts of the bushing top portion. Furthermore, at higher load currents or with lower TTOT, the temperature difference between the walls of oil becomes high, the oil flow velocity increases, and more heat is transferred by convection to the ambient.

At the rated current, the HST is located on the conductor near the flange, and the temperature rise is less than the recommended temperature rise by the IEEE standard C57.19.00. However, the study results reveal that the HST exceeds the permissible limits when the bushing is overloaded during the transformer overloading conditions. For the studied bushing, only 4% overloading is high enough to push the HST beyond the permissible limit. This implies that the bushing is a vulnerable part of the transformer from the transformer overloading point of view, and the resultant HST can adversely affect the bushing's lifetime. Consequently, it is necessary that the overload capability of bushings is taken into account when power utilities plan to overload their transformers.

Finally, the impact of GIC on the thermal performance of the transformer bushing has been investigated. Since GIC creates a wide range of current harmonics in the power system, especially transformers, the bushing conductor resistance has been calculated for odd and even harmonics based on Dwight's method. Using a topological transformer model, the GIC harmonics have been

obtained by time-domain simulation in the EMTP-RV. Then, an equivalent current is calculated for the HST estimation and bushing testing after the manufacturing process. This equivalent current has been used with a modified TEC model to find the bushing HST under various GICs. Furthermore, detailed heat and fluid dynamic analyses are performed inside the bushing to investigate the thermal behavior of the bushing under GIC. The simulation results of the realistic NERC benchmark GIC signature show that the GIC can cause the bushing temperature rise to exceed the recommended permissible limit of the IEEE standard and put the bushing at risk of hotspot heating and insulation deterioration. Even short-term hot-spot heating due to GIC can accelerate the aging of the bushing insulation and make the bushing more vulnerable to subsequent power system disturbances. Therefore, manufacturers and utilities must be aware of the effects of this phenomenon on transformer bushings.

Chapter 6

Conclusion

6.1 Conclusion

The power transformers are critical equipment in power systems. The reliability of the system is within the reliability of this expensive device. Thus, it is vital to reduce transformers' failure rate and aging. Among several factors that affect transformer reliability, thermal issues are of paramount importance. Because of that, the research in this thesis focuses on the thermal assessment of the power transformer techniques and models.

Chapter 2 explains one of the abnormal conditions that transformers may be prone to. Since transformer loading is the key element in thermal modeling, it is shown how the current injected into the transformer can be calculated during the GIC by the transformer topological model. It is shown that the inductance between the airgap and core has significant effect on the GIC calculation. However, the existing methods to calculate this inductance were not completely accurate. In this regard, a new inductance enhancement factor (IEF) for calculating the air gap

inductance for the transformer topological model is proposed.

In chapter 3, a comprehensive literature review is performed on the thermal modeling of transformers. Thermal modeling is divided into two general categories: physical and semi-physical models, such as Correlation and Lumped models, and numerical models, such as FEM and FVM. The advantages and disadvantages of both groups are thoroughly discussed. Numerical models are highly accurate yet costly with high computational time. On the other hand, the physical and semi-physical models are simple to use but not accurate enough. In addition, it is found that the thermal modeling of transformer bushings has been scarcely investigated, although it plays a vital role in transformers' reliability. The existing thermal models are also insufficient during abnormal loading conditions, such as GIC.

In chapter 4, the numerical modeling of the transformers is fully explained for both electromagnetic and thermal analysis based on the FEM. Then, an electromagnetic-thermal analysis is performed for a 3-phase 3-legs transformer under normal and GIC conditions. It is shown that the structural parts, including the tank, clamps, and tank shunts, are saturated with a small amount of GIC. However, the transformer core is saturated at higher currents, leading to more stray losses in the structural parts. This causes the HST of structural components drastically increase compared with the normal condition. The results show that the most vulnerable parts might be the tank in a way that with 66.6A GIC the HST of the tank reaches 372.14 ^{0}C, twice the allowable limit. The HST of the other structural parts.

In chapter 5, a new approach is proposed to determine the HST of OIP bushing based on the FEM-modified thermal equivalent circuit (TEC) model. The proposed model is based on a CFD modeling of the bushing considering the internal natural convection. As explained in chapter 3, both TEC and CFD models have disadvantages. Therefore, the proposed TEC model uses the

accuracy of CFD to have both simplicity and accuracy. Also, the impact of different parameters, such as load current, TTOT, and oil flow on HST are investigated. Only 4% overloading is high enough for the examined bushing to cause the HST to exceed the allowable limit. This suggests that, from the perspective of transformer overloading, the bushing is a weak point in the transformer and that the ensuing HST may negatively impact the bushing's longevity. Finally, the impact of GIC on the thermal performance of the transformer bushing has been investigated. Thus, the proposed approach is developed by adding the thermal capacitances to estimate the HST of the bushing under abnormal transient conditions, such as GIC. The results show that based on GIC magnitude and duration, the HST may increase up to a dangerous domain.

6.2 Future Work

The multiphysics simulations of electrical equipment have become an exciting topic in industries. However, there are some limitations to performing such analysis for electrical equipment, especially transformers. On the other hand, there are still some challenges with the thermal modeling of transformers that need to be solved. Thus, the research work in this thesis can be extended in future studies as listed below:

1. Improve the dynamic thermal modeling of transformer bushings for long-term and short-term overloading. The bushings' dynamic thermal modeling is neglected in the dynamic thermal modeling of transformers. The reliability of transformers can be improved by adding the bushings dynamic thermal model to the transformer dynamic thermal model.
2. Obtain an accurate model to calculate the stray losses in the structural parts. Although some analytical formulas exist to find the stray losses, this task is yet challenging and

needs high effort with long runtime. The analytical formulas are validated in normal conditions and must be validated for abnormal conditions such as GIC.

3. Analyze the single-phase transformer under GIC because this type of transformer is more vulnerable. Since the geometry of the transformer is important for GIC studies, it is vital to find the HST of different transformers with various geometry.
4. Find an equivalent circuit for the transformer structural parts for an abnormal condition such as GICs. It is vital to estimate the HST of structural parts in abnormal conditions; however, the existing models are practical for the HST of the winding.

Chapter 7

References

[1] and A. G. C. M. Ngwira, A. Pulkkinen, M. M. Kuznetsova, “Modeling extreme ‘carrington-type’ space weather events using three-dimensional global MHD simulations,” *J. Geophys. Res. Sp. Phys.*, vol. 119, no. 6, pp. 4456–4474, 2014, doi: 10.1002/2013JA019661.

[2] D. M. O. and C. M. Ngwira, “Geomagnetically induced currents: Principles,” *Brazilian J. Phys*, vol. 47, no. 5, pp. 552–560, 2017.

[3] Z. M. Khurshid, N. F. Ab Aziz, Z. A. Rhazali, and M. Z. A. Ab Kadir, “Impact of Geomagnetically Induced Currents on High Voltage Transformers in Malaysian Power Network and Its Mitigation,” *IEEE Access*, vol. 9, pp. 167204–167217, 2021, doi: 10.1109/ACCESS.2021.3135883.

[4] CIGRE C4, “Understanding of geomagnetic storm environment for high voltage power grids,” 2019.

[5] T. Wildi, “Electrical Machines & Drives,” *Electrical Machines & Drives*. Prentice Hall, Columbus, 1985, doi: 10.1016/c2009-0-15969-x.

[6] R. M. Del Vecchio and P. T. Feghali, *TRANSFORMER DESIGN PRINCIPLES*. Boca Raton, 2002.

[7] P. C. Sen, *Electric.Machines.P.C.Sen (2).pdf*. John Wiley $ Sons, 1996.

[8] S. V. Kulkarni and S. A. Khaparde, *Transformer Engineering Design, Technology, and Diagnostics*. 2004.

[9] F. Marketos, D. Marnay, and T. Ngnegueu, "Experimental and numerical investigation of flux density distribution in the individual packets of a 100 kVA transformer core," *IEEE Trans. Magn.*, vol. 48, no. 4, pp. 1677–1680, 2012, doi: 10.1109/TMAG.2011.2173667.

[10] ABB, *Transformer Handbook 1*. 2013.

[11] R. M. Del Vecchio and P. T. Feghali, *TRANSFORMER Design Principles: With Applications to Core-Form Power Transformers*. 2002.

[12] U.S. Bureau of Reclamation, *Transformers : Basics, Maintenance and Diagnostics*, vol. 1, no. April. 2005.

[13] M. Lahtinen and J. Elovaara, "GIC occurrences and GIC test for 400 kV system transformer," *IEEE Trans. Power Deliv.*, vol. 17, no. 2, pp. 555–561, 2002, doi: 10.1109/61.997938.

[14] N. Takasu, T. Oshi, F. Miyawaki, S. Saito, and Y. Fujiwara, "An experimental analysis of dc excitation of transformers by geomagnetically induced currents," *IEEE Trans. Power Deliv.*, vol. 9, no. 2, pp. 1173–1182, 1994, doi: 10.1109/61.296304.

[15] A. H. Etemadi and A. Rezaei-Zare, "Optimal placement of GIC blocking devices for geomagnetic disturbance mitigation," *IEEE Trans. Power Syst.*, vol. 29, no. 6, pp. 2753–2762, 2014, doi: 10.1109/TPWRS.2014.2309004.

[16] A. Rezaei-Zare, "Reactive power loss versus GIC characteristic of single-phase transformers," *IEEE Trans. Power Deliv.*, vol. 30, no. 3, pp. 1639–1640, 2015, doi: 10.1109/TPWRD.2015.2394311.

[17] L. Marti, A. Rezaei-Zare, and A. Narang, "Simulation of transformer hotspot heating due to geomagnetically induced currents," *IEEE Trans. Power Deliv.*, vol. 28, no. 1, pp. 320–327, 2013, doi: 10.1109/TPWRD.2012.2224674.

[18] J. W. Aquilino and J. W. Aquilino, "Report of Transformer Reliability Survey—Industrial

Plants and Commercial Buildings," *IEEE Trans. Ind. Appl.*, vol. IA-19, no. 5, pp. 858–866, 1983, doi: 10.1109/TIA.1983.4504299.

[19] T. K. Saha and P. Purkait, "Investigation of an expert system for the condition assessment of transformer insulation based on dielectric response measurements," *IEEE Trans. Power Deliv.*, vol. 19, no. 3, pp. 1127–1134, 2004, doi: 10.1109/TPWRD.2004.829100.

[20] C. AJ, M. A. Salam, Q. M. Rahman, F. Wen, S. P. Ang, and W. Voon, "Causes of transformer failures and diagnostic methods – A review," *Renew. Sustain. Energy Rev.*, vol. 82, no. July 2017, pp. 1442–1456, 2018, doi: 10.1016/j.rser.2017.05.165.

[21] M. Wang, A. J. Vandermaar, and K. D. Srivastava, "Review of condition assessment of power transformers in service," *IEEE Electr. Insul. Mag.*, vol. 18, no. 6, pp. 12–25, 2002, doi: 10.1109/MEI.2002.1161455.

[22] S. Tenbohlen and T. Stirl, "Assessment of Overload Capacity of Power Transformers by On-line Monitoring Systems," in *IEEE Power Engineering Society Winter Meeting*, 2001, pp. 1–6.

[23] M. Djamali and S. Tenbohlen, "Hundred years of experience in the dynamic thermal modelling of power transformers," *IET Gener. Transm. Distrib.*, vol. 11, pp. 2731–2739, 2017, doi: 10.1049/iet-gtd.2016.1321.

[24] S. A. Mousavi, "Electromagnetic Modelling of Power Transformers for Study and Mitigation of Effects of GICs," 2015.

[25] J. A. Martinez and B. A. Mork, "Closure on 'Transformer modeling for low- and mid-frequency transients - A review,'" *IEEE Trans. Power Deliv.*, vol. 23, no. 3, p. 1697, 2008, doi: 10.1109/TPWRD.2008.924192.

[26] O. Hydro, H. W. Donnel, B. C. Vancouver, and I. I. Dommel, "MATRIX REPRESENTATION OF THREE-PHASE N-WINDING TRANSFORMERS FOR STEADY-STATE AND TRANSIENT STUDIES," *IEEE Trans. Power Appar. Syst.*, vol. 75, no. 6, pp. 1369–1378, 1982.

[27] X. Chen, "Negative inductance and numerical instability of the saturable transformer component in EMTP," *IEEE Trans. Power Deliv.*, vol. 15, no. 4, pp. 1199–1204, 2000, doi:

10.1109/61.891503.

[28] T. Henriksen, “How to avoid unstable time domain responses caused by transformer models,” *IEEE Trans. Power Deliv.*, vol. 17, no. 2, pp. 516–522, 2002, doi: 10.1109/61.997928.

[29] M. Amp, D. H. Former, S. I. R. See, and R. External, “TRANSFORMER MO)DELS FOR TRANSIENT STUDIES BASED ON FIELD MEASUREMENTS,” *IEEE Trans. Power Appar. Syst.*, vol. PAS-100, no. 1, pp. 9–12, 1965.

[30] F. de Leon and A. Semlyen, “Complete transformer model for electromagnetic transients,” *IEEE Trans. Power Deliv.*, vol. 9, no. 1, pp. 231–239, 1994, doi: 10.1109/61.277694.

[31] X. Chen, “A THREE-PHASE MULTI-LEGGED TRANSFORMER MODEL IN ATP USING THE DIRECTLY-FORMED INVERSE INDUCTANCE MATRIX,” *IEEE Trans. Power Deliv.*, vol. 11, pp. 1554–1565, 1996.

[32] A. Rezaei-zare, “Enhanced Transformer Model for Low- and Mid-Frequency Transients—Part I: Model Development,” *IEEE Trans. POWER Deliv.*, vol. 30, no. 1, pp. 307–316, 2015.

[33] F. de Leon and A. Semlyen, “Time domain modeling of eddy current effects for transformer transients,” *IEEE Trans. Power Deliv.*, vol. 8, no. 1, pp. 271–280, 1993, doi: 10.1109/61.180346.

[34] S. Jazebi, F. De Leon, and B. Vahidi, “Duality-synthesized circuit for eddy current effects in transformer windings,” *IEEE Trans. Power Deliv.*, vol. 28, no. 2, pp. 1063–1072, 2013, doi: 10.1109/TPWRD.2013.2238257.

[35] A. Rezaei-Zare, “Enhanced transformer model for low- And mid-frequency transients - part II: Validation and simulation results,” *IEEE Trans. Power Deliv.*, vol. 30, no. 1, pp. 316–325, 2015, doi: 10.1109/TPWRD.2014.2347934.

[36] A. Ramos, J. C. Burgos, A. Moreno, and E. Sorrentino, “Determination of parameters of zero-sequence equivalent circuits for three-phase three-legged YNynd transformers based on onsite low-voltage tests,” *IEEE Trans. Power Deliv.*, vol. 28, no. 3, pp. 1618–1625, 2013, doi: 10.1109/TPWRD.2013.2259184.

[37] A. Narang and R. H. Brierley, “Topology based Magnetic Model for Steady-State and Transient Studies for Three-Phase Core Type Transformers,” *IEEE Trans. Power Syst.*, vol. 9, no. 3, pp. 1337–1349, 1994, doi: 10.1109/59.336132.

[38] T. G. Balakrishnan, A., Joines, W. T. Wilson, “Air-gap reluctance and inductance calculations for magnetic circuits using a Schwarz-Christoffel transformation,” *IEEE Trans. Power Electron.*, vol. 12, no. 4, pp. 654–663, 1997.

[39] S. E. Zirka, Y. I. Moroz, and C. M. Arturi, “Accounting for the In fl uence of the Tank Walls in the Zero-Sequence Topological Model of a Three-Phase , Three-Limb Transformer,” pp. 1–8, 2014.

[40] C. W. Mclyman, *Transformer and Inductor Design Handbook*. 2004.

[41] J. Schneider *et al.*, “Asset management techniques,” *Int. J. Electr. Power Energy Syst.*, vol. 28, no. 9 SPEC. ISS., pp. 643–654, 2006, doi: 10.1016/j.ijepes.2006.03.007.

[42] M. Sefidgaran, M. Mirzaie, and A. Ebrahimzadeh, “Reliability model of the power transformer with ONAF cooling,” *Int. J. Electr. Power Energy Syst.*, vol. 35, no. 1, pp. 97–104, 2012, doi: 10.1016/j.ijepes.2011.10.002.

[43] L. Raeisian, H. Niazmand, E. Ebrahimnia-Bajestan, and P. Werle, “Thermal management of a distribution transformer: An optimization study of the cooling system using CFD and response surface methodology,” *Int. J. Electr. Power Energy Syst.*, vol. 104, no. May 2018, pp. 443–455, 2019, doi: 10.1016/j.ijepes.2018.07.043.

[44] M. El-Harbawi and F. Al-Mubaddel, “Risk of Fire and Explosion in Electrical Substations Due to the Formation of Flammable Mixtures,” *Sci. Rep.*, vol. 10, no. 1, pp. 1–9, 2020, doi: 10.1038/s41598-020-63354-4.

[45] Cigre WG A2.38, “Transformer Thermal Modelling,” 2016. [Online]. Available: https://e-cigre.org/publication/659-transformer-thermal-modelling.

[46] IEEE C57, “IEEE Guide for Loading Mineral-Oil-Immersed Transformers and Step-Voltage Regulators - Redline,” 2012.

[47] IEC 60076-7, “Power transformers - Part 7: Loading guide for oil-immersed power

transformers," 2005.

[48] L. James and H. Wayne, "Model-Based Monitoring of Transformers," Massachusetts Inst. Technol., Laboratory for Electromagnetic and Electronic Systems, 1995.

[49] J. H. Provanzana and P. R. Gattens, "Transformer condition monitoring realizing an integrated adaptive analysis system," *Proc. CIGRE 34th Sess.*, pp. 1–105, 1992.

[50] W. H. Tang, Q. H. Wu, and Z. J. Richardson, "A simplified transformer thermal model based on thermal-electric analogy," *IEEE Trans. Power Deliv.*, vol. 19, no. 3, pp. 1112–1119, Jul. 2004, doi: 10.1109/TPWRD.2003.822968.

[51] G. L. Alegi and W. Z. Black, "Real-Time Thermal Model for an Oil-Immersed Forced-Air Cooled Transformer," *IEEE Trans. Power Deliv.*, vol. 5, no. 2, pp. 991–1000, 1990.

[52] J. Voldman, *Lumped-element Modeling with Equivalent Circuits*. 2007.

[53] K & K Associates, *Thermal Network Modeling Handbook*. Westminster: K & K Associates, 2000.

[54] L. Jauregui-Rivera and D. J. Tylavsky, "Acceptability of four transformer top-oil thermal models - Part II: Comparing metrics," *IEEE Trans. Power Deliv.*, vol. 23, no. 2, pp. 866–872, 2008, doi: 10.1109/TPWRD.2007.905576.

[55] G. Swift, T. S. Molinski, and W. Lehn, "A fundamental approach to transformer thermal modeling - Part I: Theory and equivalent circuit," *IEEE Trans. Power Deliv.*, vol. 16, no. 2, pp. 171–175, 2001, doi: 10.1109/61.915478.

[56] G. Swift, T. S. Molinski, and W. Lehn, "A Fundamental Approach to Transformer Thermal Modeling-Part II: Field Verification," *IEEE Trans. Power Deliv.*, vol. 16, no. 2, pp. 176–180, 2001, doi: 10.1109/61.915478.

[57] W. H. Tang, Q. H. Wu, and Z. J. Richardson, "Equivalent heat circuit based power transformer thermal model," *IEE Proc. Electr. Power Appl.*, vol. 149, no. 2, pp. 87–92, 2002, doi: 10.1049/ip-epa:20020290.

[58] Z. Radakovic and K. Feser, "A new method for the calculation of the hot-spot temperature in power transformers with onan cooling," *IEEE Trans. Power Deliv.*, vol. 18, no. 4, pp.

1284–1292, Oct. 2003, doi: 10.1109/TPWRD.2003.817740.

[59] V. Galdi, L. Ippolito, A. Piccolo, and A. Vaccaro, “Neural diagnostic system for transformer thermal overload protection,” *IEE Proc. - Electr. Power Appl.*, vol. 147, no. 5, p. 415, 2000, doi: 10.1049/ip-epa:20000519.

[60] D. Villacci, G. Bontempi, A. Vaccaro, and M. Birattari, “The Role of Learning Methods in the Dynamic Assessment of Power Components Loading Capability,” *IEEE Trans. Ind. Electron.*, vol. 52, no. 1, pp. 280–290, Feb. 2005, doi: 10.1109/TIE.2004.841072.

[61] M. Hell, P. Costa, and F. Gomide, “Recurrent Neurofuzzy Network in Thermal Modeling of Power Transformers,” *IEEE Trans. Power Deliv.*, vol. 22, no. 2, pp. 904–910, Apr. 2007, doi: 10.1109/TPWRD.2006.874613.

[62] M. Hell, P. Costa, and F. Gomide, “Participatory Learning in Power Transformers Thermal Modeling,” *IEEE Trans. Power Deliv.*, vol. 23, no. 4, pp. 2058–2067, Oct. 2008, doi: 10.1109/TPWRD.2008.923994.

[63] L. Jauregui-Rivera and D. J. Tylavsky, “Acceptability of Four Transformer Top-Oil Thermal Models—Part I: Defining Metrics,” *IEEE Trans. Power Deliv.*, vol. 23, no. 2, pp. 860–865, Apr. 2008, doi: 10.1109/TPWRD.2007.905555.

[64] L. Jauregui-Rivera and D. J. Tylavsky, “Acceptability of Four Transformer Top-Oil Thermal Models—Part II: Comparing Metrics,” *IEEE Trans. Power Deliv.*, vol. 23, no. 2, pp. 866–872, Apr. 2008, doi: 10.1109/TPWRD.2007.905576.

[65] D. J. Tylavsky, X. Mao, and G. A. McCulla, “Transformer Thermal Modeling: Improving Reliability Using Data Quality Control,” *IEEE Trans. Power Deliv.*, vol. 21, no. 3, pp. 1357–1366, Jul. 2006, doi: 10.1109/TPWRD.2005.864039.

[66] D. Susa, M. Lehtonen, and H. Nordman, “Dynamic thermal modelling of power transformers,” in *IEEE Power Engineering Society General Meeting, 2004.*, vol. 2, p. 1421, doi: 10.1109/PES.2004.1373100.

[67] D. Susa and M. Lehtonen, “Dynamic Thermal Modeling of Power Transformers : Further Development — Part I,” *IEEE Trans. Power Deliv.*, vol. 21, no. 4, pp. 1961–1970, 2006.

[68] D. Susa and M. Lehtonen, “Dynamic Thermal Modeling of Power Transformers : Further Development — Part II,” *IEEE Trans. Power Deliv.*, vol. 21, no. 4, pp. 1971–1980, 2006.

[69] A. Weinläder, W. Wu, S. Tenbohlen, and Z. Wang, “Prediction of the oil flow distribution in oil-immersed transformer windings by network modelling and computational fluid dynamics,” *IET Electr. Power Appl.*, vol. 6, no. 2, pp. 82–90, 2012, doi: 10.1049/iet-epa.2011.0122.

[70] J. Zhang and X. Li, “Coolant Flow Distribution and Pressure Loss in ONAN Transformer Windings - Part I: Theory and Model Development,” *IEEE Trans. Power Deliv.*, vol. 19, no. 1, pp. 186–193, 2004, doi: 10.1109/TPWRD.2003.820225.

[71] A. J. Oliver, “Estimation of Transformer Winding Temperatures and Coolant Flows Using a General Network Method.,” *IEE Proc. C Gener. Transm. Distrib.*, vol. 127, no. 6, pp. 395–405, 1980, doi: 10.1049/ip-c.1980.0061.

[72] E. Rahimpour, M. Barati, and M. Schäfer, “An investigation of parameters affecting the temperature rise in windings with zigzag cooling flow path,” *Appl. Therm. Eng.*, vol. 27, no. 11–12, pp. 1923–1930, Aug. 2007, doi: 10.1016/j.applthermaleng.2006.12.019.

[73] F. Torriano, H. Campelo, M. Quintela, P. Labbé, and P. Picher, “Numerical and experimental thermofluid investigation of different disc-type power transformer winding arrangements,” *Int. J. Heat Fluid Flow*, vol. 69, pp. 62–72, Feb. 2018, doi: 10.1016/j.ijheatfluidflow.2017.11.007.

[74] W. Wu, Z. D. Wang, A. Revell, H. Iacovides, and P. Jarman, “Computational fluid dynamics calibration for network modelling of transformer cooling oil flows - Part I heat transfer in oil ducts,” *IET Electr. Power Appl.*, vol. 6, no. 1, pp. 19–27, 2012, doi: 10.1049/iet-epa.2011.0004.

[75] W. Wu, Z. D. Wang, A. Revell, and P. Jarman, “Computational fluid dynamics calibration for network modelling of transformer cooling flows - Part II: Pressure loss at junction nodes,” *IET Electr. Power Appl.*, vol. 6, no. 1, pp. 28–34, 2012, doi: 10.1049/iet-epa.2011.0005.

[76] A. Sayma, *Computational Fluid Dynamics*. London: Bookboon, 2009.

[77] A. Sharma, *Introduction to Computational Fluid Dynamics*. chichester: John Wiley $ Sons, 2017.

[78] C. Hirsch, *Numerical Computation of internal and External Flows*, Second. Oxford: Elsevier Ltd, 2007.

[79] O. C. Zienkiewicz, R. L. Taylor, and P. Nithiarasu, *The Finite Element Method For Fluid Dynamics*, Seventh. Oxford: Elsevier Ltd, 2014.

[80] J.-M. Mufuta and E. van den Bulck, "Modelling of the mixed convection in the windings of a disc-type power transformer," *Appl. Therm. Eng.*, vol. 20, no. 5, pp. 417–437, Apr. 2000, doi: 10.1016/S1359-4311(99)00034-4.

[81] I. Fernández *et al.*, "Thermal degradation assessment of Kraft paper in power transformers insulated with natural esters," *Appl. Therm. Eng.*, vol. 104, pp. 129–138, 2016, doi: 10.1016/j.applthermaleng.2016.05.020.

[82] M. Eslamian, B. Vahidi, and A. Eslamian, "Thermal analysis of cast-resin dry-type transformers," *Energy Convers. Manag.*, vol. 52, no. 7, pp. 2479–2488, 2011, doi: 10.1016/j.enconman.2011.02.006.

[83] M. Lee, H. A. Abdullah, J. C. Jofriet, and D. Patel, "Thermal modeling of disc-type winding for ventilated dry-type transformers," *Electr. Power Syst. Res.*, vol. 80, no. 1, pp. 121–129, 2010, doi: 10.1016/j.epsr.2009.08.007.

[84] M. Lee, H. A. Abdullah, J. C. Jofriet, D. Patel, and M. Fahrioglu, "Air temperature effect on thermal models for ventilated dry-type transformers," *Electr. Power Syst. Res.*, vol. 81, no. 3, pp. 783–789, 2011, doi: 10.1016/j.epsr.2010.11.008.

[85] L. Wang, L. Zhou, H. Tang, D. Wang, and Y. Cui, "Numerical and experimental validation of variation of power transformers' thermal time constants with load factor," *Appl. Therm. Eng.*, vol. 126, pp. 939–948, 2017, doi: 10.1016/j.applthermaleng.2017.07.167.

[86] A. Skillen, A. Revell, H. Iacovides, and W. Wu, "Numerical prediction of local hot-spot phenomena in transformer windings," *Appl. Therm. Eng.*, vol. 36, pp. 96–105, Apr. 2012, doi: 10.1016/j.applthermaleng.2011.11.054.

[87] F. Torriano, P. Picher, and M. Chaaban, “Numerical investigation of 3D flow and thermal effects in a disc-type transformer winding,” *Appl. Therm. Eng.*, vol. 40, pp. 121–131, Jul. 2012, doi: 10.1016/j.applthermaleng.2012.02.011.

[88] F. Torriano, M. Chaaban, and P. Picher, “Numerical study of parameters affecting the temperature distribution in a disc-type transformer winding,” *Appl. Therm. Eng.*, vol. 30, no. 14–15, pp. 2034–2044, Oct. 2010, doi: 10.1016/j.applthermaleng.2010.05.004.

[89] R. Hosseini, M. Nourolahi, and G. B. Gharehpetian, “Determination of OD cooling system parameters based on thermal modeling of power transformer winding,” *Simul. Model. Pract. Theory*, vol. 16, no. 6, pp. 585–596, 2008, doi: 10.1016/j.simpat.2008.02.013.

[90] J. Smolka, “CFD-based 3-D optimization of the mutual coil configuration for the effective cooling of an electrical transformer,” *Appl. Therm. Eng.*, vol. 50, no. 1, pp. 124–133, 2013, doi: 10.1016/j.applthermaleng.2012.06.012.

[91] J.-M. Mufuta, “Comparison of experimental values and numerical simulation on a set-up simulating the cross-section of a disc-type transformer,” *Int. J. Therm. Sci.*, vol. 38, no. 5, pp. 424–435, May 1999, doi: 10.1016/S1290-0729(99)80013-1.

[92] J. Y. LEE, S. W. IEE, J. H. Woo, and I. S. HWANG, “CIGRE 2010 CFD analyses and experiments of a winding with zig-zag cooling duct for a power transformer Hyundai Heavy Industries Co ., Ltd . KOREA,” 2010.

[93] N. Schmidt, S. Tenbohlen, S. Chen, and C. Breuer, “Numerical and Experimental Investigation of the Temperature Distribution Inside Oil-Cooled Transformer Windings,” *18th Int. Symp. High Volt. Eng.*, no. August 2013, 2013.

[94] V. A. Yatsevsky, “Hydrodynamics and heat transfer in cooling channels of oil-filled power transformers with multicoil windings,” *Appl. Therm. Eng.*, vol. 63, no. 1, pp. 347–353, Feb. 2014, doi: 10.1016/j.applthermaleng.2013.10.055.

[95] J. Smolka and A. J. Nowak, “Experimental validation of the coupled fluid flow, heat transfer and electromagnetic numerical model of the medium-power dry-type electrical transformer,” *Int. J. Therm. Sci.*, vol. 47, no. 10, pp. 1393–1410, 2008, doi: 10.1016/j.ijthermalsci.2007.11.004.

[96] M. Kim, S. M. Cho, and J.-K. Kim, “Prediction and evaluation of the cooling performance of radiators used in oil-filled power transformer applications with non-direct and direct-oil-forced flow,” *Exp. Therm. Fluid Sci.*, vol. 44, pp. 392–397, Jan. 2013, doi: 10.1016/j.expthermflusci.2012.07.011.

[97] S. B. Paramane, W. Van der Veken, and A. Sharma, “A coupled internal–external flow and conjugate heat transfer simulations and experiments on radiators of a transformer,” *Appl. Therm. Eng.*, vol. 103, pp. 961–970, Jun. 2016, doi: 10.1016/j.applthermaleng.2016.04.164.

[98] S. B. Paramane, K. Joshi, W. Van der Veken, and A. Sharma, “CFD Study on Thermal Performance of Radiators in a Power Transformer: Effect of Blowing Direction and Offset of Fans,” *IEEE Trans. Power Deliv.*, vol. 29, no. 6, pp. 2596–2604, Dec. 2014, doi: 10.1109/TPWRD.2014.2347292.

[99] E. J. Kranenborg, C. O. Olsson, B. R. Samuelsson, and R. M. Missing, “Numerical Study On Mixed Convection And Thermal Streaking In Power Transformer,” *5th Eur. Therm. Conf. Netherlands, 2008*, pp. 1–8, 2008.

[100] C. AJ, M. A. Salam, Q. M. Rahman, F. Wen, S. P. Ang, and W. Voon, “Causes of transformer failures and diagnostic methods – A review,” *Renew. Sustain. Energy Rev.*, vol. 82, pp. 1442–1456, Feb. 2018, doi: 10.1016/j.rser.2017.05.165.

[101] I. Metwally, “Failures, Monitoring and New Trends of Power Transformers,” *IEEE Potentials*, vol. 30, no. 3, pp. 36–43, May 2011, doi: 10.1109/MPOT.2011.940233.

[102] “North American electric reliability corporation GMD task force effects of geomagnetic disturbances on bulk power system,” *Spec. Reliab. Assess. Interim Rep.*, 2012.

[103] A. Rezaei-Zare, “Behavior of Single-Phase Transformers Under Geomagnetically Induced Current Conditions,” *IEEE Trans. Power Deliv.*, vol. 29, no. 2, pp. 916–925, Apr. 2014, doi: 10.1109/TPWRD.2013.2281516.

[104] S. Girgis and R. J. Nevins, “Analysis of observed geomagnetically induced current effects on transformers,” in *in Proc. EPRI Geomagnetic. Induced Current Conference*, 1992, pp. 1–7.

[105] Cigre, “Effects of geomagnetically induced currents on power transformers,” *Electra*, no.

141, 1992.

[106] C. Gauntand and G. Coetzee, “Transformer failures in regions incorrectly considered to have low GIC-risk,” in *in Proc. IEEE Power Tech*, 2007, pp. 807–812.

[107] R. S. Girgis and C.-D. Ko, “Calculation techniques and results of effects of GIC currents as applied to large power transformers,” *IEEE Trans. Power Deliv.*, vol. 7, no. 2, pp. 699–705, Apr. 1992, doi: 10.1109/61.127070.

[108] M. Mikha-Beyranvand, J. Faiz, B. Rezaeealam, A. Rezaei-Zare, and M. Jafarboland, “Thermal analysis of power transformers under unbalanced supply voltage,” *IET Electr. Power Appl.*, vol. 13, no. 4, pp. 503–512, Apr. 2019, doi: 10.1049/iet-epa.2018.5799.

[109] W. Wu and G. Liu, *Modeling and Application of Electromagnetic and Thermal Field in Electrical Engineering*. Springer, 2019.

[110] R. M. Del Vecchio, B. Poulin, P. T. Feghali, D. M. Shah, and R. Ahuja, *Transformer design principles: Third edition*. 2017.

[111] R. A. Walling and A. H. Khan, “Characteristics of transformer exciting-current during geomagnetic disturbances,” *IEEE Trans. Power Deliv.*, vol. 6, no. 4, pp. 1707–1714, 1991, doi: 10.1109/61.97710.

[112] S. Zhang, “Evaluation of Thermal Transient and Overload Capability of High-Voltage Bushings With ATP,” *IEEE Trans. Power Deliv.*, vol. 24, no. 3, pp. 1295–1301, Jul. 2009, doi: 10.1109/TPWRD.2009.2014484.

[113] A. Pasricha and M. L. Crow, “A method of improving transformer overloading beyond nameplate rating,” in *2015 North American Power Symposium (NAPS)*, Oct. 2015, pp. 1–6, doi: 10.1109/NAPS.2015.7335148.

[114] W. J. McNutt and J. K. Easley, “Mathematical Modelling -- A Basis for Bushing Loading Guides,” *IEEE Trans. Power Appar. Syst.*, vol. PAS-97, no. 6, pp. 2393–2404, Nov. 1978, doi: 10.1109/TPAS.1978.354746.

[115] “IEEE Guide for Application of Power Apparatus Bushings,” *IEEE Stand. C57.19.100*, 2012.

[116] H. K. Youssef, M. M. Abdel Aziz, and R. Hackam, “Steady state temperature distribution of high voltage bushings-analysis and measurements,” *IEEE Trans. Power Syst.*, vol. 3, no. 1, pp. 278–285, 1988, doi: 10.1109/59.43212.

[117] H. K. Youssef and R. Hackam, “Computerized Thermal Analysis of High Voltage Bushings,” *IEEE Power Eng. Rev.*, vol. PER-7, no. 10, pp. 53–54, Oct. 1987, doi: 10.1109/MPER.1987.5526751.

[118] P. P. Hebert and R. C. Steed, “A High Voltage Bushing Thermal Performance Computer Model,” *IEEE Trans. Power Appar. Syst.*, vol. PAS-97, no. 6, pp. 2219–2224, Nov. 1978, doi: 10.1109/TPAS.1978.354725.

[119] Daxiong Zeng, “An improved method for estimating temperature rise of a bushing loaded above nameplate rating,” *IEEE Trans. Power Deliv.*, vol. 14, no. 3, pp. 986–995, Jul. 1999, doi: 10.1109/61.772344.

[120] N. Jyothi, T. Ramu, and M. Mandlik, “Temperature distribution in resin impregnated paper insulation for transformer bushings,” *IEEE Trans. Dielectr. Electr. Insul.*, vol. 17, no. 3, pp. 931–938, Jun. 2010, doi: 10.1109/TDEI.2010.5492269.

[121] S. Zhang, Z. Peng, and P. Liu, “Inner insulation structure optimization of UHV RIP oil-SF 6 bushing using electro-thermal simulation and advanced equal margin design method,” *IEEE Trans. Dielectr. Electr. Insul.*, vol. 21, no. 4, pp. 1768–1777, Aug. 2014, doi: 10.1109/TDEI.2014.004211.

[122] M. Allahbakhshi and M. Akbari, “Heat analysis of the power transformer bushings using the finite element method,” *Appl. Therm. Eng.*, vol. 100, pp. 714–720, May 2016, doi: 10.1016/j.applthermaleng.2016.02.065.

[123] M. Akbari, M. Allahbakhshi, and R. Mahmoodian, “Heat analysis of the power transformer bushings in the transient and steady states considering the load variations,” *Appl. Therm. Eng.*, vol. 121, pp. 999–1010, Jul. 2017, doi: 10.1016/j.applthermaleng.2017.05.004.

[124] Z. Yang, J. Ruan, D. Huang, Z. Du, L. Tang, and T. Zhou, “Calculation of Hot Spot Temperature of Transformer Bushing Considering Current Fluctuation,” *IEEE Access*, vol. 7, pp. 120441–120448, 2019, doi: 10.1109/ACCESS.2019.2937510.

[125] Z. Radakovic, E. Cardillo, M. Schaefer, and K. Feser, “Design of the winding–bushing interconnections in large power transformers,” *Electr. Eng.*, vol. 88, no. 3, pp. 183–190, Mar. 2006, doi: 10.1007/s00202-004-0275-x.

[126] Q. Wang, J. Liao, H. Tian, P. Liu, and Z. Peng, “Regularity analysis of the temperature distribution of epoxy impregnated paper converter transformer bushings,” *IEEE Trans. Dielectr. Electr. Insul.*, vol. 24, no. 5, pp. 3254–3264, Oct. 2017, doi: 10.1109/TDEI.2017.006685.

[127] Q. Wang, X. Yang, H. Tian, P. Liu, and Z. Peng, “A novel dissipating heat structure of converter transformer RIP bushings based on 3-D electromagnetic-fluid-thermal analysis,” *IEEE Trans. Dielectr. Electr. Insul.*, vol. 24, no. 3, pp. 1938–1946, Jun. 2017, doi: 10.1109/TDEI.2017.006027.

[128] H. Tian *et al.*, “Research on the deterioration process of electrical contact structure inside the ±500 kV converter transformer RIP bushings and its prediction strategy,” *IET Gener. Transm. Distrib.*, vol. 13, no. 12, pp. 2391–2400, Jun. 2019, doi: 10.1049/iet-gtd.2019.0110.

[129] Anderson, *Computational fluid dynamics*. New York: McGraw-Hill, 1995.

[130] X. Zhang, Z. Wang, Q. Liu, P. Jarman, and M. Negro, “Numerical investigation of oil flow and temperature distributions for ON transformer windings,” *Appl. Therm. Eng.*, vol. 130, pp. 1–9, Feb. 2018, doi: 10.1016/j.applthermaleng.2017.10.092.

[131] P. R. Price, “Geomagneticaily Induced Current Effects on Transformers,” *IEEE Power Eng. Rev.*, vol. 22, no. 6, p. 62, 2002, doi: 10.1109/MPER.2002.4312311.

[132] P. Jankee, D. T. O. Oyedokun, and H. Chisepo, “Synchronous generator modelling and excitation voltage control for GIC studies,” *Asia-Pacific Power Energy Eng. Conf. APPEEC*, vol. 2021-Novem, pp. 0–5, 2021, doi: 10.1109/APPEEC50844.2021.9687728.

[133] K. Zheng *et al.*, “Effects of system characteristics on geomagnetically induced currents,” *IEEE Trans. Power Deliv.*, vol. 29, no. 2, pp. 890–898, 2014, doi: 10.1109/TPWRD.2013.2281191.

[134] V. D. Alberston, “Geomagnetic disturbance effects on power systems,” *IEEE Trans. Power Deliv.*, vol. 8, no. 3, pp. 1206–1216, 1993.

[135] H. W. Beaty and D. G. Fink, *Standard handbook for electrical engineers*. McGraw-Hill Education, 2013.

[136] "IEC/IEEE International Standard -- Bushings for DC application," *IEC/IEEE 65700-19-03 Edition 1.0 2014-07*. pp. 1–56, 2014, doi: 10.1109/IEEESTD.2014.6853297.

[137] W. Mingli and F. Yu, "Numerical calculations of internal impedance of solid and tubular cylindrical conductors under large parameters," *IEE Proceedings-Generation Transm. Distrib.*, vol. 151, no. 1, pp. 812–820, 2004.

[138] B. Dwight, H., "Skin effect in tubular and flat conductors," *Proc. Am. Inst. Electr. Eng.*, vol. 37, no. 2, pp. 1379–1403, 1918.

[139] H. B. Dwight, "Bessel functions for AC. problems," *Trans. Am. Inst. Electr. Eng.*, vol. 48, no. 3, pp. 812–820, 1929.

[140] H. B. Dwight, "Skin effect in tubular and flat conductors," *Trans. Am. Inst. Electr. Eng.*, vol. 37, no. 2, pp. 1379–1403, 1918.

[141] COMSOL Multiphysics v. 5.3.a, "www.comsol.com," *COMSOL AB, Stockholm, Sweden*. .

[142] NERC, "Transmission System Planned Performance for Geomagnetic Disturbance Events," Atlanta, 2016.

[143] G. Meunier, *The Finite Element Method for Electromagnetic Modeling*, no. December. 2006.

[144] H. M. Ahn, Y. H. Oh, J. K. Kim, J. S. Song, and S. C. Hahn, "Experimental verification and finite element analysis of short-circuit electromagnetic force for dry-type transformer," *IEEE Trans. Magn.*, vol. 48, no. 2, pp. 819–822, 2012, doi: 10.1109/TMAG.2011.2174212.

[145] J. R. Sibué, J. P. Ferrieux, G. Meunier, and R. Périot, "Modeling of losses and current density distribution in conductors of a large air-gap transformer using homogenization and 3-D FEM," *IEEE Trans. Magn.*, vol. 48, no. 2, pp. 763–766, 2012, doi: 10.1109/TMAG.2011.2174143.

[146] H. Zhang *et al.*, "Dynamic deformation analysis of power transformer windings in short-circuit fault by FEM," *IEEE Trans. Appl. Supercond.*, vol. 24, no. 3, pp. 5–8, 2014, doi:

10.1109/TASC.2013.2285335.

[147] X. Yan, X. Yu, M. Shen, D. Xie, and B. Bai, “Research on Calculating Eddy-Current Losses in Power Transformer Tank Walls Using Finite-Element Method Combined with Analytical Method,” *IEEE Trans. Magn.*, vol. 52, no. 3, pp. 4–7, 2016, doi: 10.1109/TMAG.2015.2494375.

[148] Z. W. Zhang, W. H. Tang, T. Y. Ji, and Q. H. Wu, “Finite-element modeling for analysis of radial deformations within transformer windings,” *IEEE Trans. Power Deliv.*, vol. 29, no. 5, pp. 2297–2305, 2014, doi: 10.1109/TPWRD.2014.2322197.

[149] X. Zhang, Z. Wang, and Q. Liu, “Interpretation of Hot Spot Factor for Transformers in OD Cooling Modes,” *IEEE Trans. Power Deliv.*, vol. 33, no. 3, pp. 1071–1080, 2018, doi: 10.1109/TPWRD.2017.2710087.

Appendix I

Finite Element Method

Most systems are described mathematically by gradients or differential equations. In engineering issues, in addition to differential equations, there are additional constraints known as boundary conditions (BCs). Together, they constitute a boundary value issue, which is specified for a certain domain. Now, if the domains are simple, such as a circle or cylinder, analytical techniques such as Direct integration and Laplace transformers may be used to solve the boundary value issue. However, the geometries of the vast majority of engineering issues are complicated. To overcome these obstacles, numerical techniques such as the Finite Element Method should be used.

The finite element method (FEM), derived from matrix methods of computation of discrete or semi-discrete mechanical structures (assembly of beams), is a method for solving physics problems involving partial differential equations [143]. This is a powerful tool for describing the performance of electromagnetic devices and is used in many studies to find the magnetic flux, power losses, eddy currents, and other electromagnetic studies of transformers [144]–[148]. Although FEM is a wide topic with complicated mathematics formulas, this section briefly explains how this method can solve partial differential equations.

As discussed, FEM is applied to obtain an approximate solution for a given boundary value problem. The process of FEM is as follows:

1- The domain is divided into elements, which are smaller building blocks. This technique is known as mesh generation.
2- After meshing, calculations are performed for each individual element.
3- Assembling all elements, followed by obtaining the solution for all nodes in the domain
4- The further calculation to find the field solution for the entire domain

In order to explain better the FEM process, Poisson's equation with a set of boundary conditions is assumed for a simple rectangle shown in Figure 8-2. Poisson's equation is:

$$\frac{\partial^2 u}{\partial x^2} + \frac{\partial^2 u}{\partial y^2} = \varphi \tag{8-1}$$

If $u^e(x, y)$ is an exact solution, then

$$\frac{\partial^2 u^e}{\partial x^2} + \frac{\partial^2 u^e}{\partial y^2} - \varphi = 0 \tag{8-2}$$

Now, consider the $u'(x, y)$as an approximate solution, thus we will have

$$\frac{\partial^2 u'}{\partial x^2} + \frac{\partial^2 u'}{\partial y^2} - \varphi \neq 0 \tag{8-3}$$

So, we have a residual R as

$$R = \frac{\partial^2 u'}{\partial x^2} + \frac{\partial^2 u'}{\partial y^2} - \varphi \tag{8-4}$$

The objective is to find an approximate solution u' such that R is close to zero at each node within the domain. The FEM tries to find this approximate solution by Weighted-Residual techniques in which both sides of ((8-4) multiply by a test function $W(x, y)$ and then integrate over the domain. Thus,

$$\int W(x,y)(\nabla^2 u' - \varphi)d\Omega = 0 \tag{8-5}$$

Using the integration by parts, the weak form of ((8-5) can be obtained as

$$\int W\,\nabla u'.n'd\lambda - \int \nabla W.\nabla u' d\Omega - \int W\,\varphi d\Omega = 0 \tag{8-6}$$

Now, we can define the obtained weak form equation for each element separately. If we define $u'_i(x,y)$ the approximate solution for element i of the domain, and also u'_1, u'_2, u'_3, and u'_4 as the approximate solution values at the nodes of the element, then based on Piecewise Interpolation we will have

$$u'_i(x,y) = N_1(x,y)u'_1 + N_2(x,y)u'_2 + N_3(x,y)u'_3 + N_4(x,y)u'_4 \tag{8-7}$$

Where N_i are the known functions and u'_i are the unknown numbers. This can be written for all domain elements as

$$u'(x,y) = [N]\{u\} \tag{8-8}$$

If we substitute ((8-8) into the weak form equation ((8-6), we will get a set of linear equations for element i as

$$[k]_i\{u\}_i = \{f_i\} \tag{8-9}$$

and with applying the same procedure for all elements, a set of linear equations can be obtained

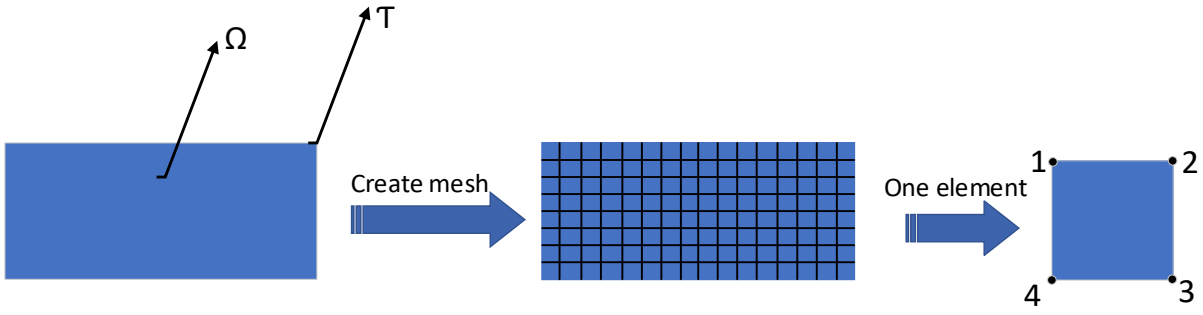

Figure 8-1. Mesh generation of a simple rectangular for FEM

for the domain as

$$[K]\{U\} = \{F\} \tag{8-10}$$

where K is the global stiffness matrix, F is the global force vector. By solving ((8-10), we can find the unknown values for all nodes of elements, and then, by Piecewise Interpolation and ((8-7), the filed representation of $u'(x, y)$ will be calculated for the entire domain.

Appendix II

Validation of the Models

In order to validate the CFD model, our CFD based-Model is implemented on the CIGRE's benchmark for the HST calculation in the transformer winding. All necessary data for CFD modeling of this benchmark can be found in [45]. As can be seen in Figure 9-1, the implemented 2D model in this thesis could estimate the HST and temperature distribution in the transformer winding as well as 3D results of the CIGRE.

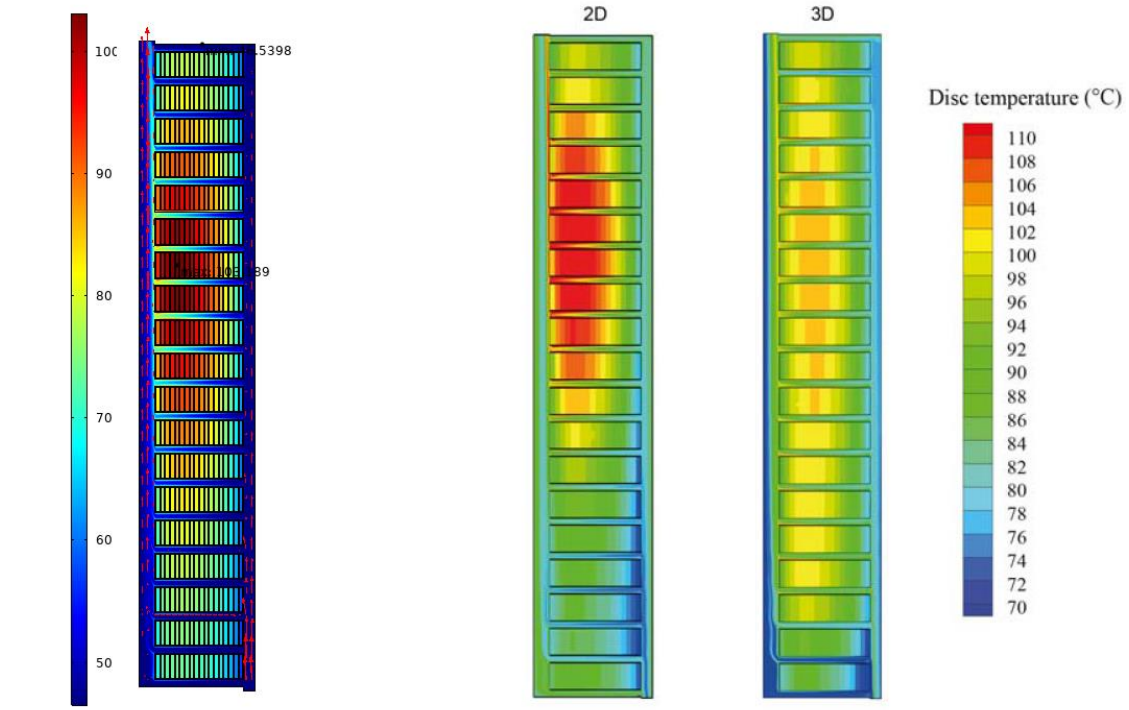

(a). HST of the benchmark based on implemented CFD model (b). HST of the benchmark based on CIGRE result [45]

Figure 9-1. Comparision results between the implemented CFD model and CIGRE result for the benchmark [45].

Regarding the bushing model, we can verify the results with comparison to other papers and methods. In [149] a CFD model of transformer is presented to calculate the hot spot factor (H) while the verification of the model is done by a new CFD simulation with different boundary conditions and a comparison between the simulations. In Chapter 5, Figure 5-10, Figure 5-11,Figure 5-12, and Figure 5-13 are all based the comparison of different CFD simulations. All the results show the accuracy of model based on the previous hints from previous works such as the location of hot spot temperature (HST) which should be on the conductor near to flange [119], [122]. In addition, the comparison of Different CFD simulations in Figure 5-10 shows that increasing the load leads to moving the location of hot spot temperature slowly to the middle of the conductor. This is due to the increase of temperature difference between the conductor and top oil tank which we expect that. Also, the same fact can be seen in Figure 5-12 when decreasing the top oil tank temperature (meaning increasing the temperature difference between the conductor and top oil tank) results in moving the location of hot spot temperature slowly to the middle of the conductor again. All these clues can verify the accuracy of the presented model.